# Masters Program in Geospatial Technologies



Spatial Suitability Analysis of Mars for Robotic Colonization and Future Human Settlement

Sebastian Suarez Andrade

Dissertation submitted in partial fulfilment of the requirements for the Degree of *Master of Science in Geospatial Technologies* 







#### NOVA Information Management School Instituto Superior de Estatística e Gestão de Informação

Universidade Nova de Lisboa

#### Spatial Suitability Analysis of Mars for Robotic Colonization and Future Human Settlement

by

Sebastian Suarez Andrade

Master Dissertation presented as partial requirement for obtaining the master's degree in Geospatial Technologies

#### Supervised by

Marco Otávio Trindade Painho, PhD, NOVA Information Management School

#### **Co-Supervised by**

Sara Ribeiro, PhD, NOVA Information Management School

Filiberto Pla Bañón, PhD, Universitat Jaume I

#### STATEMENT OF INTEGRITY

I declare that the work described in this document is my own and not from someone else. All the assistance I have received from other people is duly acknowledged and all the sources (published or not published) are referenced.

This work has not been previously evaluated or submitted to NOVA Information Management School or elsewhere. I further declare that I have fully acknowledged the Rules of Conduct and Code of Honor from the NOVA Information Management School.

Lisbon, 1<sup>st</sup> of February 2025 Sebastian Suarez Andrade

#### USE OF GENERATIVE ARTIFICIAL INTELLIGENCE

Tasks	NO	YES	Generative Artificial Intelligence tools
Better understand issues related to the research		X	Perplexity, Chat GPT
Summarizing text from bibliography / resources		X	Chat GPT
Summarizing the method(s) used	X		
Translating text	X		
Grammar check		X	Chat GPT
Paraphrase or rewriting text from other people / resources		X	Chat GPT, Deep Seek
Coding in R, Python, etc.		X	Chat GPT
Get help on a software		X	Chat GPT
Creating and editing images, maps, videos, etc.	X		
Data analysis	X		
Specify below other tasks not mentioned above:			

#### **ACKNOWLEDGEMENTS**

First and foremost, I would like to express my deepest gratitude to my beloved wife, Nicolle Herrera Gonzalez, for her unwavering support, encouragement, and belief in me throughout this journey. Her presence and dedication have been my greatest strength.

I am also profoundly thankful to my parents and my grandmothers for their lifelong guidance and support, which have shaped who I am today.

A special acknowledgment goes to my thesis supervisor, Professor Marco Painho, for his invaluable mentorship and expertise. His expertise and mentorship were instrumental in shaping this work. Additionally, I would like to thank all my professors from the Master in Science in Geospatial Technologies program for providing an exceptional learning experience and inspiring me to pursue excellence in geospatial science.

I am grateful to the institutions that hosted and supported my education, Nova Information Management School (Nova IMS) and the University of Münster, for providing exceptional academic environments and resources.

I would like to dedicate a special mention to my late mother-in-law, Mary Gonzalez, for her support and love. Although she is no longer with us, she will remain in our hearts, and she be remembered with affection and gratitude.

Finally, I sincerely thank my friends, colleagues, and everyone who contributed to making this academic journey a memorable and enriching experience.

## Spatial Suitability Analysis of Mars for Robotic Colonization and Future Human Settlement

#### **ABSTRACT**

The exploration and potential colonization of Mars have long fascinated scientists and the public, driven by the goal of extending human presence beyond Earth. However, Mars' harsh environment—thin atmosphere, extreme temperatures, high radiation, and lack of breathable oxygen—poses significant challenges. To establish a sustainable human presence, robotic colonies must serve as precursors, conducting scientific research, resource extraction, infrastructure development, and environmental monitoring to prepare viable locations for future missions. This study integrates geospatial technologies and Multi-Criteria Decision Analysis (MCDA) to identify optimal regions for robotic colonies and future human settlement, using the Analytic Hierarchy Process (AHP) combined with engineering constraints from the Perseverance (Mars 2020) mission. Engineering constraints—slope, elevation, latitude, surface reflectivity, and load-bearing properties—delineated non-viable areas, while factors including surface temperature, water-equivalent hydrogen, elevation, and terrain stability, determined suitable locations for human habitability. The integrated suitability map highlights certain regions at the four-region intersection between Oxia Palus-Margaritifer-Arabia-Sinus Sabaeus (area  $\approx 600'000 \text{ km}^2$ ), Memnonia (area 30'000 km²) and Aeolis (area  $\approx 160'000 \text{ km}^2$ ) as the most promising sites, with the first one emerging as the preferred option due to its larger contiguous terrain, reducing landing uncertainties and enhancing mission flexibility. This study provides a systematic and scalable framework for selecting robotic colony sites while ensuring safe and sustainable operations, ultimately supporting long-term human exploration. Beyond planetary exploration, these findings contribute to humanity's pursuit of interplanetary expansion—securing survival, advancing scientific frontiers, and positioning Mars as a gateway for deep-space exploration.

#### **KEYWORDS**

Analytic Hierarchy Process; Geospatial Technologies; Mars Colonization; Multi-Criteria Decision Analysis; Geospatial Suitability Analysis

#### **Sustainable Development Goals (SGD):**









## **INDEX**

STATEMENT OF INTEGRITY	0
USE OF GENERATIVE ARTIFICIAL INTELLIGENCE	0
ACKNOWLEDGEMENTS	1
ABSTRACT	2
INDEX OF TABLES	5
INDEX OF FIGURES	6
ACRONYMS	10
1. Introduction	11
2. RELATED WORK - LITERATURE REVIEW	13
2.1 MARS OVERVIEW	13
2.2 MARS EXPLORATION	14
2.2.1 ROBOTIC MISSIONS FOR MARS EXPLORATION	15
2.3 ADVANCEMENTS OF ROBOTIC OPERABILITY IN MARTIAN SURFACE	16
2.4 SITE SELECTION FOR SAFE LANDING & ROBOTIC OPERABILITY	18
2.4.1 EDL - ENTRY, DESCENT AND LANDING	19
2.4.2 Landing Site Engineering Constraints	20
2.4.2.1 ELEVATION	21
2.4.2.2 LATITUDE AND THERMAL CONDITIONS	21
2.4.2.3 LANDING ELLIPSE	22
2.4.2.4 SLOPE AND TERRAIN	23
2.4.2.5 THERMOPHYSICAL PROPERTIES: DUST AND LOAD BEARING SURFACE	24
2.5 SCIENCE CRITERIA FOR ASSESSING CANDIDATE SITES	28
2.6 MARS COLONIZATION	29
2.6.1 THE ROLE OF ROBOTS IN MARS COLONIZATION	29
2.6.2 Human Habitability in Mars	30
2.6.2.1 SURVIVAL ON MARS.	31
2.6.2.2 WATER	32
2.6.2.3 ENERGY	35
2.6.2.4 HABITATS	36
2.7 Mars Climate Database	36
3. METHODOLOGY	38
3.1 METHODOLOGICAL FRAMEWORK	38
3.2 EXPLORATORY SPATIAL DATA ANALYSIS	39
3.2.1 Data Overview	39
3.2.2 Data Preparation	41

3.2.2.1 PREPARATION OF SEASONAL DATA	41
3.2.2.2 COORDINATE SYSTEM ALIGNMENT	49
3.2.3 Analysis of Seasonal Variability	49
3.2.4 DESCRIPTIVE STATISTICS & DATA VISUALIZATION	51
3.2.4.1 ELEVATION	51
3.2.4.2 WATER EQUIVALENT HYDROGEN (WEH)	52
3.2.4.3 Thermal Inertia	53
3.2.4.4 Albedo	55
3.2.4.5 Surface Temperature	56
3.2.4.6 Surface Pressure	57
3.2.4.7 Incoming Radiative Flux to Surface	58
3.2.5 SPATIAL CORRELATION ANALYSIS	59
3.3 DERIVED DATASETS: SLOPE & THERMOPHYSICAL UNITS	60
3.4 Engineering constraints for Safe Landing and Robotic Operability	61
3.4.1 ALTITUDE-BASED ENGINEERING CONSTRAINT	62
3.4.2 SLOPE-BASED ENGINEERING CONSTRAINT	63
3.4.3 LATITUDE-BASED ENGINEERING CONSTRAINT	63
3.4.4 LOAD BEARING SURFACE AND RADAR REFLECTIVITY-BASED ENGINEERING CO	ONSTRAINT 64
3.4.5 Unified Engineering Constraints Map	65
3.5 MULTI-CRITERIA HUMAN HABITABILITY ASSESSMENT USING ANALYTIC HIERAF	RCHY PROCESS
(AHP)	66
3.5.1 SENSITIVITY ANALYSIS	70
3.5.1.1 PEARSON'S CORRELATION ANALYSIS	70
3.5.1.2 SPEARMAN'S RANK CORRELATION ANALYSIS	71
3.5.1.3 SUITABILITY SCORE 10 OVERLAP ANALYSIS	72
4. RESULTS AND DISCUSSION	74
5. Conclusions	78
6. Future Work	79
BIBLIOGRAPHICAL REFERENCES	80

### INDEX OF TABLES

TABLE 1 — SUMMARY OF KEY MARS ROBOTIC MISSIONS, INCLUDING THEIR LAUNCH YEAR,  OPERATING AGENCY, SPACECRAFT TYPE, AND MAJOR SCIENTIFIC HIGHLIGHTS. TAKEN FROM  (MAITY & SAXENA, 2024)
TABLE 2 — SUMMARY OF LANDING SITE ENGINEERING CONSTRAINTS AND SAFETY CRITERIA FOR THE MARS 2020 PERSEVERANCE ROVER MISSION (GRANT ET AL., 2018)
Table 3 — From filled thermophysical unit map. Each unit is interpreted based on surface properties, such as unconsolidated fines, duricrust, or bedrock, as indicated in the interpretation column. Percent surface area represents the proportional coverage of each unit across Mars. (Putzig et al., 2005)
Table 4 — Load Bearing Surface landing site engineering constraint and safety criteria for the Mars 2020 rover. Taken and Edited from Grant et al., (2018) 27
Table 5 — Science criteria for assessing candidate Sites at third 2020 landing site workshop (Grant et al., 2018)
Table 6 — Key spatial criteria selected to identify the most suitable Martian regions for robotic colonies as precursors to human settlement, along with their data sources, factor type (Static/Dynamic), seasonal data details and data extent 39
TABLE 7 — CLASSIFICATION OF INITIAL KEY CRITERIA BASED ON THEIR APPLICATION IN THE METHODOLOGICAL FRAMEWORK: HUMAN HABITABILITY MULTI-CRITERIA ANALYSIS AND ENGINEERING CONSTRAINTS FOR SAFE LANDING AND ROBOTIC OPERABILITY
<b>TABLE 8 (LEFT)</b> — MARS' ORBITAL POSITION (SOLAR LONGITUDE, $L_s$ ) IN RELATION TO EACH OF THE 12 MARTIAN MONTHS FOR THE SEASONAL DATASETS OF THE MCD: SURFACE TEMPERATURE, SURFACE PRESSURE AND INCOMING RADIATIVE FLUX
Table 9— Correlation Matrix of selected variables for human habitability suitability analysis
TABLE 10 — LANDING SITE ENGINEERING CONSTRAINTS AND SAFETY CRITERIA USED. TAKEN FROM THE MARS 2020 PERSEVERANCE ROVER MISSION (GRANT ET AL., 2018)
TABLE 11 — CRITERIA INCLUDED IN AHP METHOD FOR SUITABILITY ANALYSIS OF HUMAN HABITABILITY
TABLE 12 — AHP PAIRWISE COMPARISON MATRIX
TABLE 13 — NORMALIZED AHP MATRIX WITH CRITERION WEIGHTS
TABLE 14 — WEIGHTED SUM MATRIX FOR CONSISTENCY CALCULATION IN AHP
TABLE 15 — CONSISTENCY ANALYSIS RESULTS FOR AHP MATRIX
<b>TABLE <math>16</math></b> — Criteria Weights of Suitability Models created for sensitivity analysis $76$
TABLE 17 — PEARSON'S CORRELATION SENSITIVITY ANALYSIS OF SUITABILITY MODELS
TABLE 18 — SPEARMAN'S RANK CORRELATION BETWEEN BASELINE AND SENSITIVITY MODELS 72
TABLE 19 — SUITABILITY SCORE 10 OVERLAP BETWEEN BASELINE AND SENSITIVITY MODELS 73

## **INDEX OF FIGURES**

FIGURE 1 — IMAGE OF MARS CAPTURED BY NASA'S HUBBLE SPACE TELESCOPE FROM APPROXIMATELY 55.76 MILLION KM (NASA, 2008)	3
FIGURE 2 — AN ARTISTIC IMPRESSION OF KEY CONSTRAINTS IN CULTIVATING CROPS ON MARS, HIGHLIGHTING KEY ENVIRONMENTAL FACTORS (MAITY & SAXENA, 2024)	4
FIGURE 3 — SCHEMATIC DIAGRAM OF THE HEXAPOD ROBOT INSPIRED BY THE MOVEMENT OF ANTS (CHEN ET AL., 2024)	6
FIGURE 4 — THE RESULTS OF SEMANTIC SEGMENTATION OF SANDY AND ROCKY ENVIRONMENTS (CHEN ET AL., 2024).	7
FIGURE 5 — MARS 2020 MISSION EXPLORATION ROBOTS: A) INGENUITY MARS HELICOPTER; B) PERSEVERANCE MARS ROVER. MADE FROM (JET PROPULSION LABORATORY, 2020) INTERACTIVE 3D MODELS	8
FIGURE 6 — ENTRY, DESCENT AND LANDING SEQUENCE FOR THE MARS SCIENCE LABORATORY FROM CRUISE STAGE SEPARATION THROUGH LANDING (M. GOLOMBEK ET AL., 2012)	9
FIGURE 7 — LATITUDE BANDS DESIGNATED FOR THE EXOMARS (GREEN) AND MARS 2020 (BLUE) ROVERS OVERLAID ON A MOLA BASEMAP OF MARS. THE MARS 2020 ROVER, POWERED BY AN RTG, ALLOWS FOR A BROADER LATITUDE RANGE, WHICH ENCOMPASSES THE EXOMARSDESIGNATED REGION SINCE EXOMARS LACKS AN RTG (PAJOLA ET AL., 2019B)	:2
FIGURE 8 — EXAMPLES OF LANDING ELLIPSE SIZES USED IN MARS ROBOTIC EXPLORATION, RANGING FROM THE VIKING LANDERS TO THE MARS 2020 ROVER (PAJOLA ET AL., 2016A; PAJOLA ET AL., 2019B)	,
FIGURE 9 — NIGHTTIME BOLOMETRIC THERMAL INERTIA MAP OF MARS. INTERPOLATION WAS APPLIED TO FILL GAPS BETWEEN TES GROUND TRACKS FOR LATITUDES SPANNING 80°S TO 80°N (PUTZIG ET AL., 2005)	
FIGURE 10 — TES ALBEDO FOR MARS YEAR 26. ALBEDO VALUES RANGE FROM 0 TO 1, WHERE 1 INDICATES A PERFECTLY REFLECTIVE SURFACE THAT REFLECTS ALL INCIDENT RADIATION, AND REPRESENTS COMPLETE ABSORPTION WITH NO REFLECTION. (PUTZIG ET AL., 2005)	
FIGURE 11—TWO-DIMENSIONAL HISTOGRAM SHOWING THE GLOBAL RELATIONSHIP BETWEEN TES NIGHTTIME BOLOMETRIC THERMAL INERTIA AND VISIBLE BOLOMETRIC ALBEDO. WHITE AREAS INDICATE NO OCCURRENCES. UNITS A, B, AND C REPRESENT THE PRIMARY MODES OF FREQUENT CORRELATION, WHILE OUTLIERS ARE UNITS D, E, F, AND G. (PUTZIG ET AL., 2005)	
FIGURE 12 — THERMAL INERTIA—ALBEDO UNIT MAP OF MARS. UNITS REPRESENT THERMAL INERTIA—ALBEDO MODES IN FIG. 13. WHITE AREAS CORRESPOND TO REGIONS BETWEEN UNIT BOUNDS IN FIG. 13 (PUTZIG ET AL., 2005)	:6
FIGURE 13 — SUITABILITY MAPS FROM ZHU ET AL. (2025) FOR ABOVEGROUND BUILDING SITES ON MARS, GENERATED USING AN AHP MODEL. THREE SUITABILITY ZONES—PRIMARY, SECONDARY, AND TERTIARY—ARE SHOWN	0
FIGURE 14 — SUITABILITY MAPS FROM ZHU ET AL. (2025) FOR UNDERGROUND BUILDING SITES ON MARS, GENERATED USING AN AHP MODEL. THREE SUITABILITY ZONES—PRIMARY, SECONDARY, AND TERTIARY—ARE SHOWN	1
FIGURE 15 — THE MINIMUM (TOP) AND MAXIMUM (BOTTOM) WATER EQUIVALENT HYDROGEN (WEH) MAPS FROM 50°N TO 50°S, DISPLAY THE RANGE OF POTENTIAL VALUES, ACCOUNTING FOR MEASUREMENT UNCERTAINTIES WITH $+\Sigma$ AND $-\Sigma$ (MALAKHOV ET AL., 2022)	3
FIGURE 16 — MAP SHOWING THE THICKNESS OF THE ICE-RICH PORTIONS OF THE MEDUSAE FOSSAE FORMATION (MFF) DEPOSITS, WITH ESTIMATED ICE VOLUMES RANGING FROM $\sim 2.2 \times 10^5$ km³ to	0

$\sim$ 4.0 $\times$ 105 km³. The boundaries of the MFF deposits have been modified from Tanaka et al. (014) as referenced in Watters et al. (2024)	4
FIGURE 17 — METHODOLOGICAL FRAMEWORK FOR THE IDENTIFICATION OF MOST SUITABLE REGIONS FOR ROBOTIC COLONIZATION AND FUTURE HUMAN SETTLEMENT	8
FIGURE 18 (RIGHT)— MARS' ORBITAL POSITION IN RELATION TO EACH OF THE 12 MARTIAN MONTHS FOR THE SEASONAL DATASETS OF THE MCD (MILLOUR ET AL., 2022; MILLOUR ET AL., 2014; FORGET ET AL., 1999)	
Figure 19 — Surface temperature layer at 02:00:00, first Martian month (solar longitude $0^{\circ}$ to $30^{\circ}$ )	2
FIGURE 20 — SURFACE TEMPERATURE LAYER AT 04:00:00, FIRST MARTIAN MONTH (SOLAR LONGITUDE 0° TO 30°)	2
FIGURE 21 — SURFACE TEMPERATURE LAYER AT 06:00:00, FIRST MARTIAN MONTH (SOLAR LONGITUDE 0° TO 30°)	2
Figure 22 — Surface temperature layer at $08:00:00$ , first Martian month (solar longitude $0^{\circ}$ to $30^{\circ}$ )	3
Figure 23 — Surface temperature layer at $10:00:00$ , first Martian month (solar longitude $0^{\circ}$ to $30^{\circ}$ )	3
Figure 24 — Surface temperature layer at 12:00:00, first Martian month (solar longitude $0^{\circ}$ to $30^{\circ}$ )	3
Figure 25 — Surface temperature layer at 14:00:00, first Martian month (solar longitude $0^{\circ}$ to $30^{\circ}$ )	3
Figure 26 — Surface temperature layer at 16:00:00, first Martian month (solar longitude $0^{\circ}$ to $30^{\circ}$ )	4
Figure 27 — Surface temperature layer at 18:00:00, first Martian month (solar longitude $0^{\circ}$ to $30^{\circ}$ )	4
Figure 28 — Surface temperature layer at 20:00:00, first Martian month (solar longitude $0^{\circ}$ to $30^{\circ}$ )	4
Figure 29 — Surface temperature layer at 22:00:00, first Martian month (solar longitude $0^{\circ}$ to $30^{\circ}$ )	4
Figure 30 — Surface temperature layer at 00:00:00, first Martian month (solar longitude $0^{\circ}$ to $30^{\circ}$ )	.5
FIGURE 31 — MEAN SURFACE TEMPERATURE LAYER OF THE 1ST MARTIAN MONTH (SOLAR LONGITUDE OF $0^{\circ}$ TO $30^{\circ}$ )	.5
Figure 32 — Mean surface temperature layer of the 2nd Martian month (solar longitude of $30^{\circ}$ to $60^{\circ}$ )	.5
FIGURE 33 — MEAN SURFACE TEMPERATURE LAYER OF THE $3^{\rm RD}$ MARTIAN MONTH (SOLAR LONGITUDE OF $60^{\circ}$ TO $90^{\circ}$ )	6
FIGURE 34 — MEAN SURFACE TEMPERATURE LAYER OF THE $4^{\text{TH}}$ MARTIAN MONTH (SOLAR LONGITUDE OF $90^{\circ}$ TO $120^{\circ}$ )	
FIGURE 35 — MEAN SURFACE TEMPERATURE LAYER OF THE $5^{\text{TH}}$ MARTIAN MONTH (SOLAR LONGITUDE OF $120^{\circ}$ to $150^{\circ}$ )	6
FIGURE $36$ — Mean surface temperature layer of the 6th Martian month (solar longitude of $150^{\circ}$ to $180^{\circ}$ )	6
FIGURE 37 — MEAN SURFACE TEMPERATURE LAYER OF THE $7^{\text{th}}$ MARTIAN MONTH (SOLAR LONGITUDE OF $180^{\circ}$ to $210^{\circ}$ )	7

FIGURE 38 — MEAN SURFACE TEMPERATURE LAYER OF THE $8^{\text{th}}$ MARTIAN MONTH (SOLAR LONGITUDE OF $210^{\circ}$ to $240^{\circ}$ )
FIGURE 39 — MEAN SURFACE TEMPERATURE LAYER OF THE $9^{\text{th}}$ MARTIAN MONTH (SOLAR LONGITUDE OF $240^{\circ}$ to $270^{\circ}$ )
FIGURE 40 — MEAN SURFACE TEMPERATURE LAYER OF THE $10^{\text{th}}$ Martian month (solar longitude of $270^{\circ}$ to $300^{\circ}$ )
FIGURE 41 — MEAN SURFACE TEMPERATURE LAYER OF THE 11 <sup>th</sup> Martian month (solar longitude of 300° to 330°)
FIGURE 42 — MEAN SURFACE TEMPERATURE LAYER OF THE 12 <sup>th</sup> MARTIAN MONTH (SOLAR LONGITUDE OF 330° TO 360°)
<b>FIGURE 43</b> —Surface temperature layer representative of a standard Martian year $48$
FIGURE 44 —SURFACE PRESSURE LAYER REPRESENTATIVE OF A STANDARD MARTIAN YEAR 49
FIGURE 45 — INCOMING RADIATIVE FLUX TO SURFACE LAYER REPRESENTATIVE OF A STANDARD MARTIAN YEAR
FIGURE 46 — STANDARD DEVIATION MAP OF THE SURFACE TEMPERATURE DATASET REPRESENTATIVE OF A STANDARD MARTIAN YEAR (SOLAR LONGITUDE OF $0^{\circ}$ to $360^{\circ}$ ) 50
Figure 47 — Standard Deviation map of the Incoming radiative flux to surface dataset representative of a standard Martian year (solar longitude of $0^{\circ}$ to $360^{\circ}$ ) 50
FIGURE 48 — STANDARD DEVIATION MAP OF THE SURFACE PRESSURE DATASET REPRESENTATIVE OF A STANDARD MARTIAN YEAR (SOLAR LONGITUDE OF $0^{\circ}$ TO $360^{\circ}$ )
FIGURE 49 — ELEVATION MAP OF MARS (50°N TO 50°S). ELEVATION IN METERS; QUADRANGLES REPRESENT STANDARD GEOGRAPHIC DIVISIONS OF MARS
FIGURE 50 — ELEVATION HISTOGRAM OF MARS (50°N TO 50°S).
FIGURE 51 —WATER EQUIVALENT HYDROGEN MAP OF MARS (50°N TO 50°S). MEASURED IN PERCENTAGE BY WEIGHT, QUADRANGLES REPRESENT STANDARD GEOGRAPHIC DIVISIONS OF MARS. DATA EXTRACTED FROM (MALAKHOV ET AL., 2022)
FIGURE 52 —WATER EQUIVALENT HYDROGEN HISTOGRAM OF MARS (50°N TO 50°S)
FIGURE 53 —THERMAL INERTIA MAP OF MARS (50°N TO 50°S). MEASURED IN J·M <sup>-2</sup> ·K <sup>-1</sup> ·S <sup>-1/2</sup> ; QUADRANGLES REPRESENT STANDARD GEOGRAPHIC DIVISIONS OF MARS. DATA EXTRACTED FROM (PUTZIG ET AL., 2005)
FIGURE 54 —THERMAL INERTIA HISTOGRAM OF MARS (50°N TO 50°S)
FIGURE 55 —ALBEDO MAP OF MARS (50°N TO 50°S). RANGES FROM 0 (FULL ABSORPTION) TO 1 (FULL REFLECTIVITY); QUADRANGLES REPRESENT STANDARD GEOGRAPHIC DIVISIONS OF MARS. DATA EXTRACTED FROM (PUTZIG & MELLON, 2007)
FIGURE 56 —ALBEDO HISTOGRAM OF MARS (50°N TO 50°S).
FIGURE 57 —SURFACE TEMPERATURE MAP OF MARS (50°N TO 50°S). MEASURED IN KELVIN, QUADRANGLES REPRESENT STANDARD GEOGRAPHIC DIVISIONS OF MARS
FIGURE 58—SURFACE TEMPERATURE HISTOGRAM OF MARS (50°N TO 50°S)
FIGURE 59 —SURFACE PRESSURE MAP OF MARS (50°N TO 50°S). MEASURED IN PASCAL, QUADRANGLES REPRESENT STANDARD GEOGRAPHIC DIVISIONS OF MARS
FIGURE 60 —SURFACE PRESSURE HISTOGRAM OF MARS (50°N TO 50°S)
FIGURE 61 — INCOMING RADIATIVE FLUX TO SURFACE MAP OF MARS (50°N TO 50°S). MEASURED IN $W/m^2$ (WATTS PER SQUARE METER), QUADRANGLES REPRESENT STANDARD GEOGRAPHIC
DIVISIONS OF MARS

FIGURE 62 — INCOMING RADIATIVE FLUX TO SURFACE HISTOGRAM OF MARS (50°N TO 50°S) 5
FIGURE 63—SLOPE MAP OF MARS (50°N TO 50°S). MEASURED IN DEGREES (°) REPRESENTS THE ANGLE OF TERRAIN INCLINATION DERIVED FROM THE ELEVATION DATASET; QUADRANGLES REPRESENT STANDARD GEOGRAPHIC DIVISIONS OF MARS
FIGURE 64 —THERMOPHYSICAL UNIT MAP OF MARS (50°N TO 50°S). EACH UNIT IS INTERPRETED BASED ON SURFACE PROPERTIES (TABLE 3); QUADRANGLES REPRESENT STANDARD GEOGRAPHIC DIVISIONS OF MARS.
FIGURE 65 — ALTITUDE CONSTRAINT MAP OF MARS (50°N TO 50°S). AREAS ABOVE -500 METERS ARE RESTRICTED (RED), WHILE NON-RESTRICTED AREAS ARE SHOWN IN GRAY; QUADRANGLES REPRESENT STANDARD GEOGRAPHIC DIVISIONS OF MARS
<b>FIGURE 66</b> — SLOPE CONSTRAINT MAP OF MARS ( $50^{\circ}$ N to $50^{\circ}$ S). Areas with slopes greater than $5^{\circ}$ are restricted (red), while non-restricted areas are shown in gray; Quadrangles represent standard geographic divisions of Mars
FIGURE 67— LATITUDE CONSTRAINT MAP OF MARS (50°N TO 50°S). AREAS BEYOND 30°N AND 30°S ARE RESTRICTED (RED), WHILE NON-RESTRICTED AREAS ARE SHOWN IN GRAY; QUADRANGLES REPRESENT STANDARD GEOGRAPHIC DIVISIONS OF MARS
FIGURE 68 — LOAD-BEARING SURFACE AND RADAR REFLECTIVITY CONSTRAINT MAP OF MARS (50°) TO 50°S). AREAS DOMINATED BY UNCONSOLIDATED FINES OR UNSTABLE SURFACES (UNITS OTHER THAN B AND C) ARE RESTRICTED (RED), WHILE STABLE SURFACES REMAIN NON-RESTRICTED (GRAY); QUADRANGLES REPRESENT STANDARD GEOGRAPHIC DIVISIONS OF MARS.
FIGURE 69 — UNIFIED ENGINEERING CONSTRAINTS MAP OF MARS (50°N TO 50°S). AREAS THAT FAIL TO MEET ONE OR MORE ENGINEERING CONSTRAINTS (ALTITUDE, SLOPE, LATITUDE, OR LOAD-BEARING SURFACE/RADAR REFLECTIVITY) ARE RESTRICTED (RED), WHILE REGIONS THAT SATISFY ALL CONSTRAINTS REMAIN NON-RESTRICTED (GRAY); QUADRANGLES REPRESENT STANDARD GEOGRAPHIC DIVISIONS OF MARS
FIGURE 70— ALTERNATIVE SYMBOLOGY FOR THE UNIFIED ENGINEERING CONSTRAINTS MAP OF MARS (50°N TO 50°S). SAFE LANDING AND ROBOTIC OPERABILITY ZONES ARE HIGHLIGHTED IN GREEN, WHILE RESTRICTED AREAS REMAIN IN GRAY; QUADRANGLES REPRESENT STANDARD GEOGRAPHIC DIVISIONS OF MARS.
FIGURE 71— HUMAN HABITABILITY SUITABILITY MAP OF MARS (50°N TO 50°S). SUITABILITY VALUES CLASSIFIED BY NATURAL BREAKS, FROM 1 (LEAST SUITABLE) TO 10 (MOST SUITABLE). ADDITIONAL MAP VIEWS HIGHLIGHT KEY GEOLOGICAL FEATURES—OLYMPUS MONS & ASCRAEUS MONS (BOTTOM-LEFT); AND THE VALLES MARINERIS ZONE (BOTTOM-RIGHT) 6
FIGURE 72 — INTEGRATED SUITABILITY MAP FOR MARS FOR ROBOTIC COLONIES AND FUTURE HUMAN SETTLEMENT. RESTRICTED AREAS RECEIVE THE LOWEST SCORE (1), WHILE NON-RESTRICTED REGIONS RETAIN THEIR ORIGINAL AHP-DERIVED SCORES (2 TO 10)
FIGURE 73 —FILTERED SUITABILITY MAP OF MARS (50°N TO 50°S) DISPLAYING THE MOST PROMISING REGIONS FOR FUTURE ROBOTIC COLONIES AND POTENTIAL HUMAN SETTLEMENTS (HIGHEST-SCORING AREAS 8, 9, AND 10), BASED ON INTEGRATED HABITABILITY CRITERIA AND ENGINEERING CONSTRAINTS. MARS ROVERS DISPLAYED IN MAIN MAP FOR REFERENCE
FIGURE 74 — FOCUSED SUITABILITY MAP FOR MARS (50°N TO 50°S) HIGHLIGHTING ONLY REGIONS WITH A SUITABILITY SCORE OF 10. FOUR SUPPLEMENTARY LOCAL-SCALE MAP VIEWS (A-D) FURTHER DETAIL THESE KEY AREAS, OFFERING AN IN-DEPTH PERSPECTIVE ON THE MOST FAVORABLE ZONES FOR ROBOTIC COLONIES AND POTENTIAL HUMAN SETTLEMENTS

#### **ACRONYMS**

AHP - Analytic Hierarchy Process

**CNN** – Convolutional Neural Network

**DEM** – Digital Elevation Model

**EDL** – Entry, Descent, and Landing

**ESDA** - Exploratory Spatial Data Analysis

**EUV** – Extreme Ultraviolet

**FREND** – Fine Resolution Epithermal Neutron Detector

**GCM** – General Circulation Model

**HEND** – High Energy Neutron Detector

**IRTM** – Viking Infrared Thermal Mapper

**JPL** – Jet Propulsion Laboratory

**LMD** – Laboratoire de Météorologie Dynamique

**LSS** – Life Support Systems

MARSIS – Mars Advanced Radar for Subsurface and Ionosphere Sounding

MCD - Mars Climate Database

MER – Mars Exploration Rover

**MFF** – Medusae Fossae Formation

MGS - Mars Global Surveyor

**MOLA** – Mars Orbiter Laser Altimeter

**MSL** – Mars Science Laboratory

**NASA** – National Aeronautics and Space Administration

NOVA IMS – Instituto Superior de Estatística e Gestão de Informação

**PCM** - Planetary Climate Model

**RL** – Reinforcement Learning

**RTG** – Radioisotope Thermoelectric Generator

**TES** – Thermal Emission Spectrometer

**TGO** – Trace Gas Orbiter

**USGS** – United States Geological Survey

**WEH** – Water Equivalent Hydrogen

#### 1. Introduction

The exploration and potential colonization of Mars have long been central objectives in planetary science and space exploration. However, Mars presents extreme environmental challenges, including low atmospheric pressure, harsh temperature fluctuations, high radiation exposure, and a lack of breathable oxygen. Overcoming these obstacles necessitates a strategic, phased approach in which robotic colonies serve as a crucial preliminary step before human settlement. These robotic systems could play a vital role in conducting scientific research, monitoring environmental conditions, extracting resources, constructing infrastructure, and establishing life support systems, laying the groundwork for long-term human habitation (Schulze-Makuch & Irwin, 2008).

Therefore, identifying suitable locations for robotic colonies is essential to ensuring their longterm operability and efficiency as precursors to human settlement. This research integrates geospatial technologies and Multi-Criteria Decision Analysis (MCDA) to evaluate potential sites by combining engineering constraints for safe landing and robotic operability with a human habitability suitability assessment. The engineering constraints analysis is based on Mars 2020 Perseverance mission parameters (Grant et al., 2018), applying restrictions on slope, elevation, latitude, and surface properties to delineate non-viable areas for robotic operations. In parallel, a suitability analysis for human habitability is conducted using the Analytic Hierarchy Process (AHP), assessing factors such as surface temperature, water-equivalent hydrogen, slope, and altitude. The AHP pairwise comparison model used in this study is adapted from Zhu et al. (2025), originally developed for an aboveground building scenario for habitat site selection on Mars, with modifications on criteria and datasets used. By combining the engineering constraints layer with the AHP-based habitability assessment, this research produces a final suitability map, highlighting regions that are both safe for robotic operations and favorable for long-term habitability. This approach ensures a systematic evaluation of the Martian surface, identifying the most promising locations for robotic colonies that will pave the way for future human exploration and settlement.

To achieve these objectives, the study is guided by the following research questions:

1) Which are the primary criteria that influence the suitability of Martian regions for establishing robotic colonies and future human settlements?

- 2) How can geospatial technologies and multi-criteria decision analysis be effectively integrated to evaluate the suitability of potential sites on Mars for robotic colonies as precursors to human settlements?
- 3) Which are the most suitable regions on Mars for the establishment of robotic colonies as precursors to human settlement?

This research contributes to the advancement of planetary exploration strategies by providing a scientifically driven framework for selecting optimal locations for robotic colonies, ensuring their long-term viability and laying the foundation for sustainable human presence on Mars.

#### 2. RELATED WORK - LITERATURE REVIEW

#### 2.1 MARS OVERVIEW

Mars (Figure 1) is our second closest planetary neighbor after Venus and shares several characteristics with Earth, particularly in its dynamic and water-rich nature. However, the Martian environment presents significant challenges, such as extremely low temperatures averaging around -63°C, fluctuating between -115°C and 20°C, the absence of an ozone layer and magnetospheric protection, and the lack of surface liquid water. Despite having a thin but considerable atmosphere composed primarily of carbon dioxide (95%), Mars remains a difficult environment for sustaining life (Schulze-Makuch & Irwin, 2008).

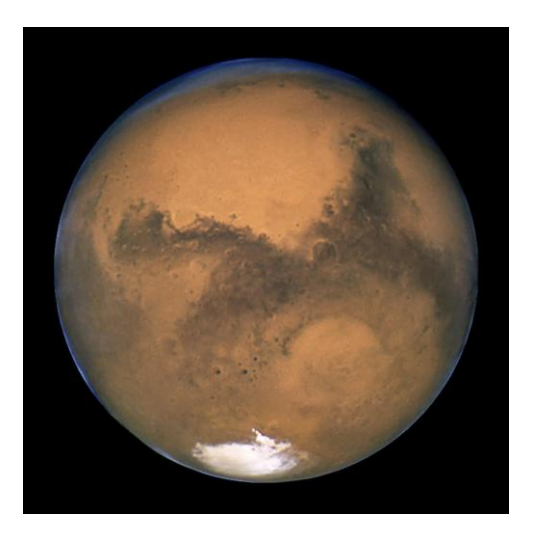


**Figure 1** — Image of Mars captured by NASA's Hubble Space Telescope from approximately 55.76 million km (NASA, 2008).

Despite its extreme environment, Mars is the most Earth-like planet in the Solar System, offering essential resources such as shelter, minerals, water and a tenuous atmosphere, which together make its potential colonization conceivable. Additionally, while liquid water is unstable on the surface today and quickly vaporizes, various findings suggest its presence beneath the surface and potentially in underground caves (Boynton et al., 2002; Schulze-Makuch & Irwin, 2008). As such, Mars remains the only planet with conditions that, while harsh, could offer limited habitability to terrestrial organisms, including humans (Schulze-Makuch & Irwin, 2008).

The following Figure 2, from Maity & Saxena (2024), focuses on the key constraints in cultivating crops on Mars but also provides valuable insights into the broader environmental differences between Earth and Mars. By highlighting critical factors such as distance from the Sun, gravity, atmosphere, soil composition, and temperature, the image offers a comparative analysis that is highly relevant for understanding the challenges Mars presents for long-term human settlement.

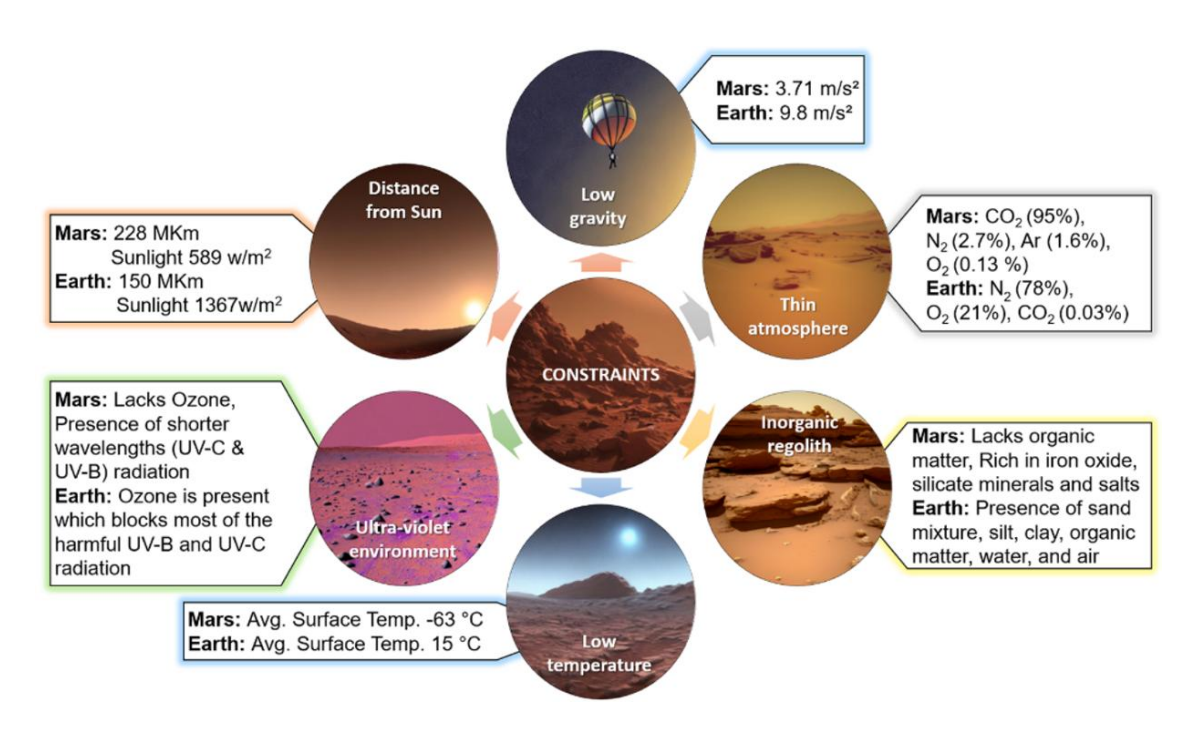


**Figure 2** — An artistic impression of key constraints in cultivating crops on Mars, highlighting key environmental factors (Maity & Saxena, 2024).

#### 2.2 MARS EXPLORATION

According to NASA (2024), Mars exploration is guided by the following key scientific objectives aimed at understanding the planet's history, its potential for life, and its suitability for future human missions:

- **a. Search for Signs of Life**: Scientists target areas where water existed or remains hidden—like ancient lakes, underground ice deposits, and hydrothermal regions—because water is essential for life.
- **b.** Understanding Mars' Climate: Researchers analyze Mars' dynamic weather, including dust storms and seasonal changes, to reconstruct its past climate and determine if it once supported conditions favorable for life.
- c. Geological Studies: Mars' diverse landscape, featuring volcanoes, ancient riverbeds, and impact craters, is examined to understand the planet's evolution and the processes that have shaped rocky worlds.
- **d. Preparing for Human Exploration:** Efforts are underway to address Mars' environmental challenges such as high radiation and extreme temperatures, focusing on resource utilization and safety strategies to pave the way for future human missions.

#### 2.2.1 ROBOTIC MISSIONS FOR MARS EXPLORATION

Previous robotic missions to Mars have primarily pursued either in-depth exploration of a single site -by using a lander, a rover or a helicopter-, or broad planetary mapping -via an orbiter. While landers and rovers offer detailed analyses of specific, accessible locations, they lack the capability to provide a regional perspective. In contrast, orbiters generate extensive global datasets but with limited local resolution (Schulze-Makuch & Irwin, 2008). The following Table 1 shows a summary of some of these key Mars robotic missions.

**Table 1** — Summary of key Mars robotic missions, including their launch year, operating agency, spacecraft type, and major scientific highlights. Taken from (Maity & Saxena, 2024).

Viking 1 & Viking 2 (Daniels et al., 2003; Hess et al., 1980)	1975	NASA	Orbiter & Lander	The meteorological data obtained in the mission measured the composition and structure of Mars' upper atmosphere such as atmospheric temperature, wind speed, wind direction, and pressure. First time conducted biology experiments designed to look for existence of life on Mars
Mars Odyssey (operational) (Saunders et al., 2004)	2001	NASA	Orbiter	This spacecraft holds the record for being the longest-operating spacecraft in orbit around a planet other than Earth. Its findings revealed significant amounts of hydrogen in the soil, indicating the potential presence of subsurface ice. It made a ground-breaking discovery of substantial subsurface water ice in the northern arctic plain and created detailed maps of the distribution and quantity of minerals and elements on the planet's surface.
Mars Express (operational) (Formisano et al., 2004; Pätzold et al., 2016)	2003	ESA	Orbiter	The Mars Express Radio Science Experiment has successfully accomplished multiple objectives in the fields of ionospheric physics, geology, geophysics, and solar science. It provided valuable insights into the heterogeneity of the Martian surface, ranging from low-density soil to dry solid rock. Additionally, the orbiter achieved a significant milestone by detecting methane on Mars for the first time, marking a significant finding in the exploration of the planet.
Mars Exploration Rover Mission ( Afshinnekoo et al., 2020; Arvidson et al., 2011)	2003	NASA	Twin Rovers; Spirit and opportunity	Both rovers have discovered compelling evidence of previous wet conditions on Mars, suggesting the potential for supporting microbial life in the past.
Phoenix (Boynton et al., 2009; Hecht et al., 2009; Kounaves et al., 2010)	2007	NASA	Lander	The lander acquired numerous samples of Martian dry and icy soil through excavation for sophisticated scientific analysis. Major findings include study of history of water, presence of carbonate and perchlorate in soil.
Mars Science Laboratory (operational) ( Hassler et al., 2014)	2011	NASA	Rover (Curiosity)	The rover mission accomplished that Martian site 'Gale Crater' had been hospitable, made of rocks that had formed on a lakebed under water suggesting that Mars atmosphere was suitable for microbial life. The data obtained also indicated that Mars had a massive ocean in the past, which was partly covered in ice and surrounded by glaciers on the lower plains of the northern hemisphere.
ExoMars 2016 (operational) (Giuranna et al., 2019)	2016	ESA/ Rosmoscos	Orbiter (Lander lost on descent)	The orbiter is observing Martian atmosphere in search of evidence of gases of possible biological importance, such as methane and its degradation products.
Tianwen-1 (operational) (Wan et al., 2020)	2020	CNSA	2 Orbiters, 2 landers and a rover	The goal is to explore the shape, composition, space environment, and distribution of water-ice on Mars.
Mars 2020 (operational) (Williford et al., 2018)	2020	8NASA	Rover & helicopter	The mission is aimed to investigate regional geology, seek signs of past extra- terrestrial life in an ancient habitable environment and assemble a returnable cache of samples.

On the other hand, about the next logical steps in Mars exploration, Schulze-Makuch & Irwin (2008) discusses that after a sample return mission, the establishment of a permanent robotic station would be the next step. This robotic base would serve as an essential precursor to a human mission, offering significant scientific benefits. Such a robotic station is considered essential for the success of future human exploration, while numerous robotic missions would also be needed to pave the way for a sustainable human presence on Mars Schulze-Makuch & Irwin (2008).

# 2.3 ADVANCEMENTS OF ROBOTIC OPERABILITY IN MARTIAN SURFACE

Mars features a diverse landscape, characterized by vast plains and a variety of distinct geomorphic features, including rocky and sandy terrains, which make robotic mobility on Mars very challenging (Chen et al., 2024). Given the high cost and risk associated with planetary missions, as well as the challenges of operating in uncertain environments like the Martian surface, a highly capable mobile robot is essential to support long-term exploration (Chen et al., 2024; Huang et al., 2020; Lele et al., 2020; Zhang J. et al., 2021).

Over the past few decades, several semi-autonomous or autonomous robots leveraging the latest technological and engineering advancements have been proposed to tackle the significant challenges of performing complex tasks and navigating the unpredictable Martian terrain. These advancements have led to the development of innovative systems for terrain adaptability, mobility, functional tasks, and autonomous decision-making, all of which are crucial for Mars exploration (Chen et al., 2024; Huang et al., 2020). Key examples of these technological developments are presented below, demonstrating how they contribute to the feasibility of long-term robotic operations on Mars.

Chen et al. (2024) developed a hexapod robot inspired by the movement of ants (Figure 3). This design features adaptable gaits, mechanical redundancy, and strong fault tolerance, providing stability across rough terrains.

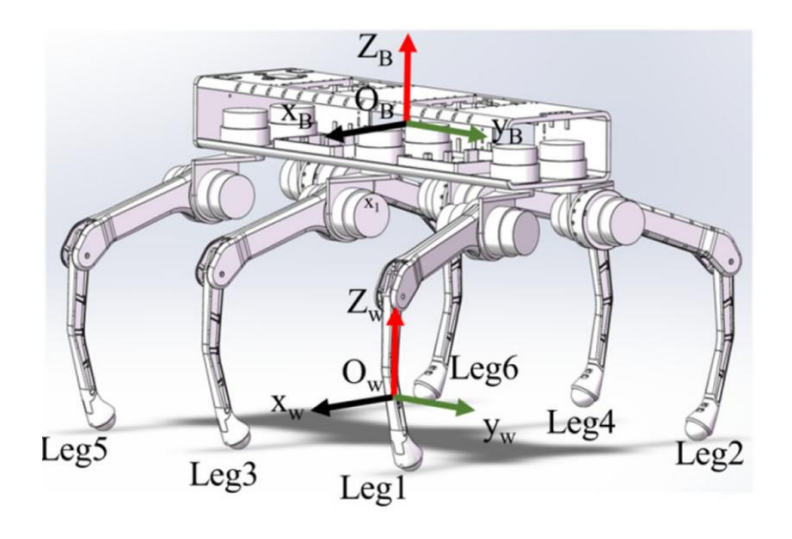


Figure 3 — Schematic diagram of the hexapod robot inspired by the movement of ants (Chen et al., 2024).

The robot is equipped with a convolutional neural network (CNN) for efficient terrain recognition allowing it to identify and classify the Martian surface through semantic segmentation of visual images (Figure 4) (Chen et al., 2024). Moreover, it incorporates a performance evaluation system that measures key motion characteristics, such as speed and stability. Additionally, the robot's ability to switch between gaits seamlessly improves its capacity to maneuver through difficult landscapes, positioning it as a promising solution for future planetary exploration (Chen et al., 2024).

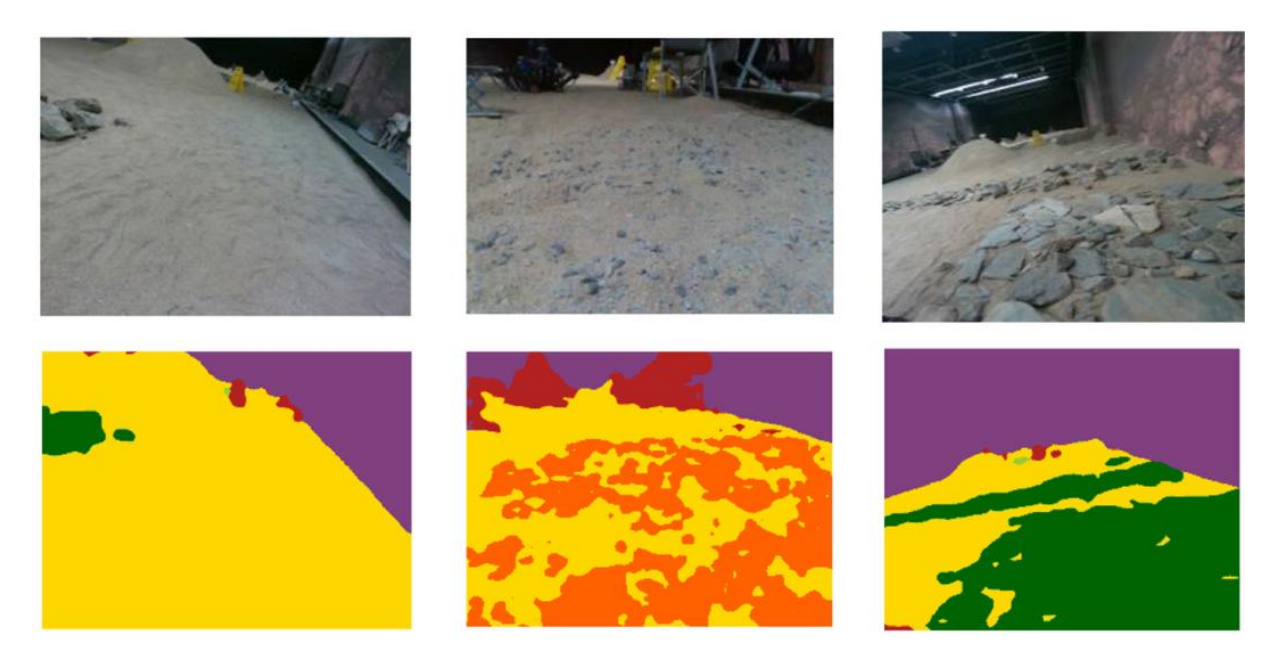


Figure 4 — The results of semantic segmentation of sandy and rocky environments (Chen et al., 2024).

Furthermore, to enhance the reliability and effectiveness of exploration missions, particularly in challenging environments like Mars, one promising solution is the use of swarm robotics (Huang et al., 2020; Martinez Rocamora et al., 2023; Petrovsky et al., 2022). By utilizing a swarm of robots instead of a single, highly sophisticated one, exploration missions and tasks can be carried out more efficiently through collaboration, offering a more reliable and resilient alternative to traditional approaches. Each robot within the swarm can autonomously handle specific tasks with the possibility to collaborate with each other, optimizing the overall performance of the mission. Reinforcement learning (RL), particularly multi-agent systems using deep deterministic policy gradients, has shown promise in enabling these robots to learn cooperative behaviors (Huang et al., 2020).

Lastly, in the context of ongoing robotic missions for Mars exploration, the Mars 2020 mission, which landed the Perseverance Rover in Mars in 2021 (Figure 5a), highlights the growing focus on enhancing robot mobility and the integration of cooperative robotics described in the above

examples. A key advancement is the deployment of the first flying robot on Mars (Ingenuity Mars Helicopter; Figure 5b), which opens up new possibilities for exploring regions that were previously unreachable (Petrovsky et al., 2022).





**Figure 5** — Mars 2020 mission exploration robots: a) Ingenuity Mars Helicopter; b) Perseverance Mars Rover.

Made from (Jet Propulsion Laboratory, 2020) interactive 3D models.

All these collaborative approaches significantly broaden the scope of Mars exploration, demonstrating the evolving role of robotics in overcoming challenges and expanding exploration capabilities (Petrovsky et al., 2022).

#### 2.4 SITE SELECTION FOR SAFE LANDING & ROBOTIC OPERABILITY

Over the last decades, multiple robotic missions have successfully been carried out on the Martian surface (Table 1). These achievements have been possible due to meticulous landing site selection processes, which ensure both the operational and lading safety of the mission and the feasibility of scientific exploration (Grant et al., 2018).

Selecting a landing site on Mars surface is a long (>4 years) and challenging endeavor, characterized by several engineering and scientific challenges (Golombek et al. 2012; Pajola et al., 2019). As highlighted by Golombek et al. (2003), selecting an appropriate site involves evaluating engineering constraints-requirements for the current technology available, defining acceptable locations, and gathering data to certify potential landing zones Golombek et al. (2003). These factors collectively contribute to mission success and the long-term sustainability of robotic exploration on Mars.

The engineering criteria for safe landing and robotic operability encompass various factors, including the site's latitude and elevation, the dimensions of the landing ellipse, surface slopes, rock distribution, thermal inertia, albedo, radar reflectivity, and atmospheric conditions (Pajola et al., 2019; Golombek et al., 2012; Golombek et al., 2003)

#### 2.4.1 EDL - ENTRY, DESCENT AND LANDING

Due to Mars having a thin atmosphere, which is not dense enough to allow for purely aerodynamic landings, all landing systems must incorporate a combination of parachutes and aeroshells, supplemented by additional descent technologies to ensure a controlled touchdown Golombek et al. (2013). Figure 6 is one of the examples and illustrates the entry, descent and landing sequence (EDL) used for the successful landing of the Curiosity rover in 2012 (M. Golombek et al., 2012; Grant et al., 2018).

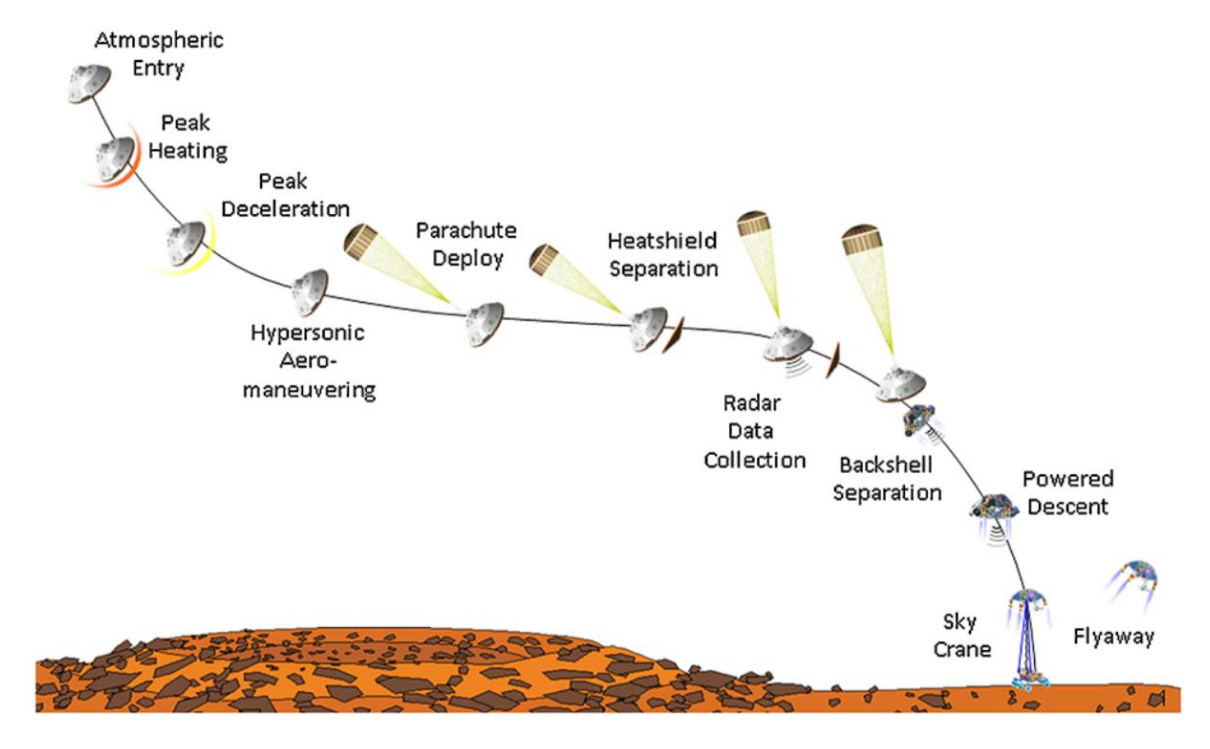


**Figure 6** — Entry, descent and landing sequence for the Mars Science Laboratory from cruise stage separation through landing (M. Golombek et al., 2012).

This sophisticated system (Figure 6) incorporated several advancements, such as the aero-maneuvering -enabling the spacecraft to actively adjust its trajectory during hypersonic flight-which significantly enhanced the process of selecting a landing site due to the considerable reduction in the uncertainty of the landing ellipse (Golombek et al., 2012).

Earlier Mars missions that relied on uncontrolled ballistic descent had landing ellipses approximately 100 km in length. In contrast, this refined aero-maneuvering capabilities reduced its landing ellipse to about 25 km. Since landing sites must avoid hazardous features such as craters and steep or rugged terrain, this smaller ellipse significantly expanded the number of potential landing locations considered for a lander compared to previous Mars missions (Golombek et al., 2012).

Furthermore, this EDL sequence system introduced the groundbreaking 'Sky Crane landing technique,' which significantly improved the system's ability to handle high surface slopes during touchdown. This increased tolerance to uneven terrain allowed for the consideration of landing sites that were far rougher than those deemed suitable for earlier missions (Golombek et al., 2012). The enhanced EDL system and sequence (Figure 6) was later refined and utilized for the Perseverance Rover's landing in 2021, further demonstrating its reliability and precision in ensuring safe touchdowns on the Martian surface (Golombek et al., 2012; Grant et al., 2018).

#### 2.4.2 LANDING SITE ENGINEERING CONSTRAINTS

All lander missions shown in Table 1 adhered to a set of engineering constraints designed to ensure safe landing and operational functionality on the surface. These constraints are governed by the limitations of the EDL technology employed in each mission, as well as the inherent constraints of the robotic systems available at the time. The following table (Table 2) presents the landing site engineering constraints and safety criteria for the Mars 2020 mission (Perseverance Rover), which serve as the current baseline, reflecting the technological limitations of the most recent successful mission. These constraints closely resemble those of the MSL mission (Curiosity Rover) in 2013, as both missions employed comparable EDL technology (Golombek et al., 2012; Grant et al., 2018).

**Table 2** — Summary of landing site engineering constraints and safety criteria for the Mars 2020 Perseverance rover mission (Grant et al., 2018)

Engineering Parameter	Requirement for Landing Sites	Notes/Rationale
Latitude	30°N to 30°S	Sites poleward of 30°N and 30°S have surface thermal limitations
Elevation	$< -0.5 \mathrm{km^b}$	Relative to the Mars Orbiter Laser Altimeter (MOLA) datum
Radius and Azimuth of Landing Ellipse	≤16.0 km (down-track direction, approx. W-E) 14 km (cross- track direction, approx. N-S) <sup>c</sup>	Using range trigger reduces the ellipse size, includes wind-induced uncertainty during parachute descent
Terrain Relief/Slopes	2–10 km length scale: ≤ 20°	Radar spoofing in preparation for powered descent <sup>a</sup>
-	$1{-}2$ km length scale: $\leq 43$ m relief at 1 km, linearly increasing to 720 m and 2 km $^{\rm a}$	Radar spoofing in preparation for powered descent <sup>a</sup>
	1 m-1000 m baseline length scale: ≤ 100 m relief	For control authority and fuel consumption, increased from MSL
	2 m–5 m length scale: $\leq$ 25°–30°	Rover landing stability/trafficability after landing; Increased from original MSL specification
Rock Height	$\leq$ 0.6 m (assumes a max rock height of 0.55 m and a rover sinkage of 0.05 m)	<0.50% probability rock > 0.6 m high occurs in random area of 4 m <sup>2</sup> (belly pan) (~12% rock abundance) <sup>n</sup>
Radar Reflectivity	Ka band reflective	Adequate Ka band radar backscatter cross-section (>-20 dB and <15 dB) <sup>a</sup>
Load Bearing Surface	Not dominated by dust	Thermal inertia $>$ 100 J m-2 s $-$ 0.5 K-1 and albedo $<$ 0.25; radar reflectivity $>$ 0.01 for load bearing bulk density <sup>a</sup>
Atmosphere	Up to 25 m/s horizontal and 20 m/s vertical winds	During EDL <sup>a</sup>
Surface winds for Thermal	During Operation:	For 1 m above the surface. These constraints provide an environment in which the
Environment	<15 m/s (steady)	rover can perform science operations <sup>a</sup>
	<30 m/s (gusts)	·
	Non-Operation (sleeping):	
	<40 m/s (steady)	

Building on the constraints outlined in Table 2, several factors are particularly critical for ensuring a successful landing and operability. These landing site engineering constraints and safety criteria establish the conditions under which a mission can safely land and function,

guiding the selection of suitable sites based on atmospheric conditions, energy availability, surface stability, terrain characteristics, and environmental hazards (Golombek et al., 2013).

The evolution of robotic systems and EDL technologies has aimed to increase access to a broader range of Martian regions by expanding landing capabilities, allowing for greater flexibility in site selection. This ensures that missions are less restricted by factors such as latitude, elevation, and terrain, enabling them to respond to new scientific discoveries and objectives (Golombek et al., 2012).

The following sections examine each of these factors in detail, highlighting their role in mission success and their influence on the current engineering decisions behind landing site selection.

#### **2.4.2.1 ELEVATION**

Elevation plays a crucial role in landing site selection, as it directly affects the spacecraft's entry dynamics and braking efficiency, which are integral to the EDL sequence (Golombek et al., 2012). One of the ways the elevation influences EDL performance is through its effect on atmospheric density. Mars has a thin atmosphere, which, although not dense enough to provide significant aerodynamic drag on its own, is still essential for slowing down a spacecraft during descent. At lower elevations, the denser atmosphere allows for greater aerodynamic braking, facilitating more effective velocity reduction before the final descent phase. This results in a better-controlled terminal velocity, making the landing process more manageable. As a consequence, past rover and lander missions have consistently targeted low-altitude regions, making elevation one of the most critical engineering constraints in determining landing site suitability (Golombek et al., 2003; Golombek et al., 2012; Golombek et al., 2013). As shown in Table 2, the preferred elevation for landing sites in the Mars 2020 mission is below 0.5 km relative to the Mars Orbiter Laser Altimeter (MOLA) datum (Grant et al., 2018).

#### 2.4.2.2 LATITUDE AND THERMAL CONDITIONS

Energy availability is a key factor in landing site selection for robotic missions, as most rely on solar power for operation. Sites near the equator are preferred to maximize energy intake, with landing locations typically targeted between 30°N and 30°S (Table 2; Figure 7) for optimal operational conditions (Grant et al., 2018). These regions benefit from stable thermal conditions and more consistent solar energy, with only minor cosine losses at angles away from the subsolar latitude, slightly mitigated by atmospheric diffusion. In contrast, sites at higher latitudes experience significant thermal fluctuations, affecting both power generation and

thermal regulation, and even missions using Radioisotope Thermoelectric Generators (RTGs) face challenges in maintaining consistent temperatures (Golombek et al., 2012).

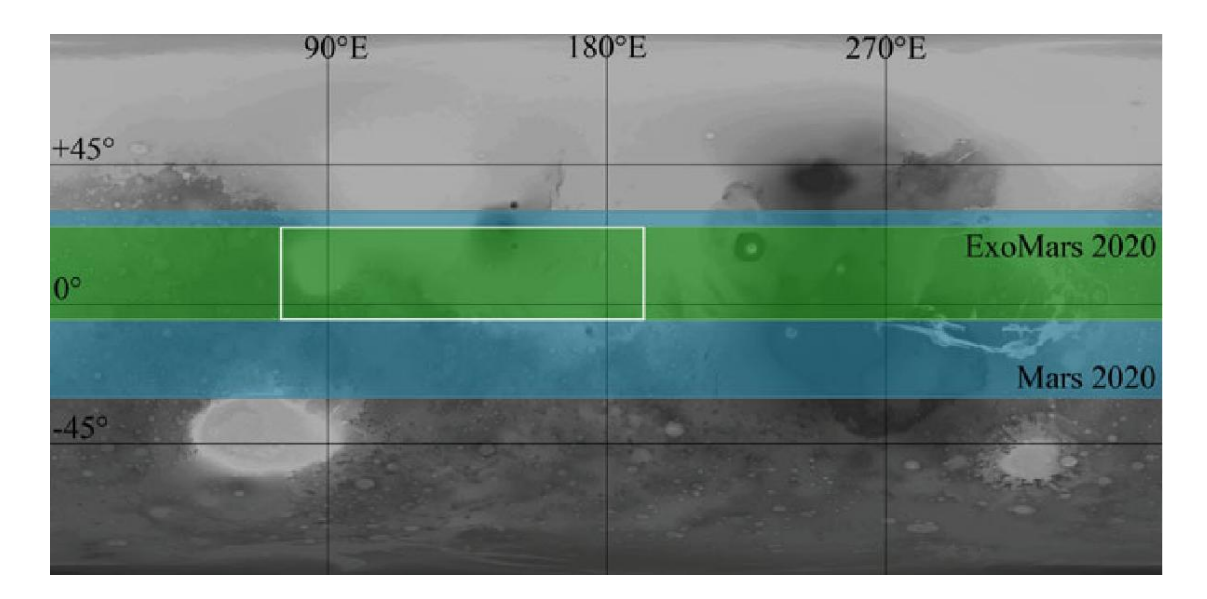


**Figure 7** — Latitude bands designated for the ExoMars (green) and Mars 2020 (blue) rovers overlaid on a MOLA basemap of Mars. The Mars 2020 rover, powered by an RTG, allows for a broader latitude range, which encompasses the ExoMars-designated region since ExoMars lacks an RTG (Pajola et al., 2019b).

The rover's performance hinges on its ability to collect and store solar energy during the day for nighttime thermal regulation. If the energy collected is insufficient, especially in colder, high-latitude conditions where more energy is needed for heating, the rover risks becoming inoperable or non-productive. Consequently, milder, near-equatorial temperatures are preferred for optimal operations (Golombek et al., 2012; Golombek et al., 2003).

#### 2.4.2.3 LANDING ELLIPSE

The landing ellipse defines the 99% probability region where the rover is expected to land (Figure 8). Its size and orientation are determined by uncertainties in entry trajectory, descent dynamics, and atmospheric conditions (Golombek et al., 2003a; Grant et al., 2018). For instance, a major improvement in EDL system from Figure 6, the Range Trigger method, reduced the uncertainty ellipse size by controlling parachute deployment based on a prespecified latitude and longitude rather than velocity.

Nevertheless, despite any EDL improvements, the landing ellipses must still be evaluated for hazards such as steep slopes, high rock abundance, and unstable terrain, as the rover could land anywhere within the defined region (Golombek et al., 2003; Grant et al., 2018). These additional criteria and engineering constraints are described in the following sections.

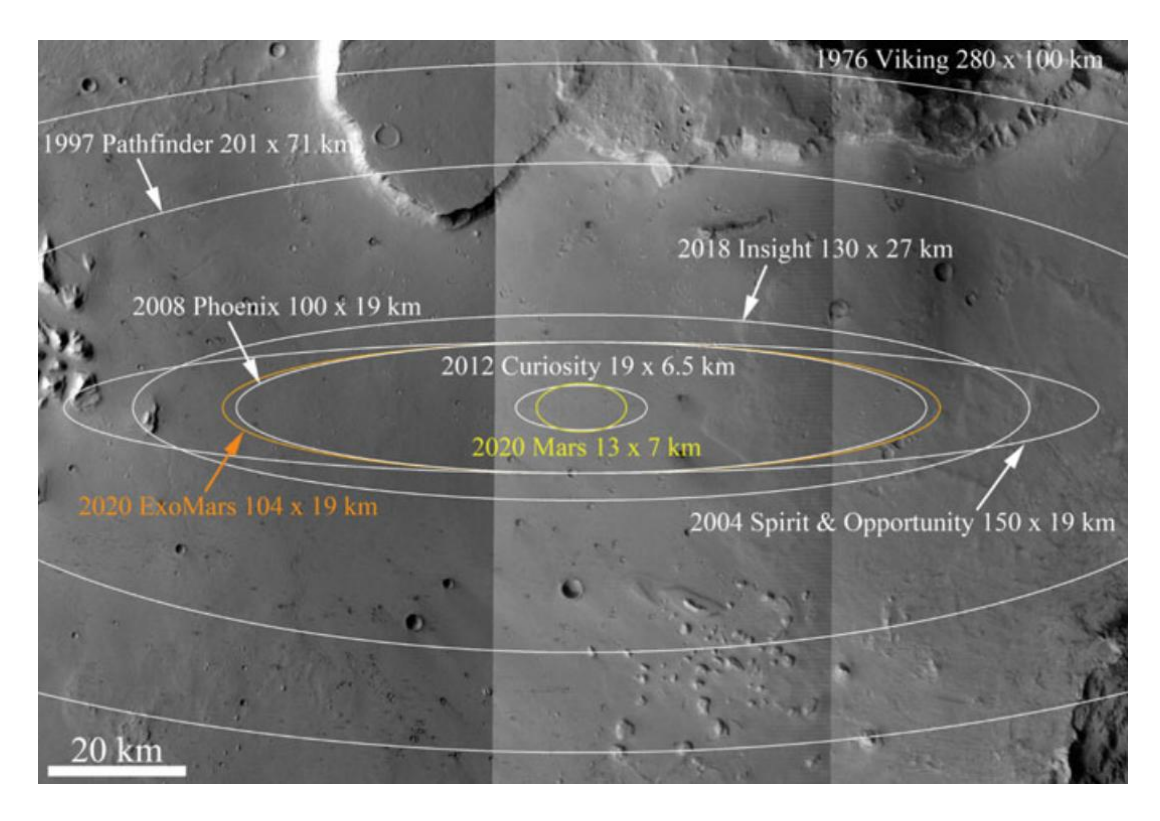


**Figure 8** — Examples of landing ellipse sizes used in Mars robotic exploration, ranging from the Viking Landers to the Mars 2020 rover (Pajola et al., 2016a; Pajola et al., 2019b).

#### 2.4.2.4 SLOPE AND TERRAIN

Slope and terrain variability impose critical constraints on landing site selection, influencing descent control, touchdown stability, and rover mobility. To prevent radar spoofing during descent, terrain relief should not exceed 20 m at the 2–10 km scale and must increase linearly from 43 m at 1 km to 720 m at 2 km (Table 2). For powered descent, the rover requires terrain relief below  $100 \text{ m} (5^{\circ})$  at the 1–1000 m scale to ensure effective fuel use and altitude estimation as well as for control authority and energy consumption purposes (Grant et al., 2018).

At smaller scales, surface slopes directly impact rover stability. While the rover is designed to handle slopes up to 30°, an initial constraint of 15° was used to ensure safe touchdown and post-landing operations. Tests later confirmed safe operation on slopes up to 30°, though risk increases beyond this threshold. At the 2–5 m scale, slopes should not exceed 25–30° to maintain rover stability and ensure successful traversability (Golombek et al., 2003; Golombek et al., 2012; Grant et al., 2018).

# 2.4.2.5 THERMOPHYSICAL PROPERTIES: DUST AND LOAD BEARING SURFACE

As referenced by Putzig et al. (2005), previous investigations carried out by Mellon et al. (2000) suggest that quantitative comparison between thermal inertia and albedo is key to inferring the characteristics of the martian surface, which allows the distinguishment of different thermophysical units.

Thermal inertia is a fundamental property governing diurnal temperature variations on the Martian surface. Measured in Jm<sup>-2</sup> K<sup>-1</sup> s<sup>-1/2</sup>, it describes the ability of the subsurface (upper 2–30 cm) to absorb heat during the day and re-radiate it at night. It depends on factors such as: particle size, the degree of induration, rock abundance, and bedrock exposure within the top few centimeters (M. Golombek et al., 2012; Putzig et al., 2005).

By using the nighttime Thermal Emission Spectrometer (TES) bolometer observations of the brightness temperature of Mars, Putzig et al. (2005) produced a global thermal inertia map with a resolution of  $\frac{1}{20}$ ° per pixel and a coverage from 80°N to 80°S latitudes (Figure 9).

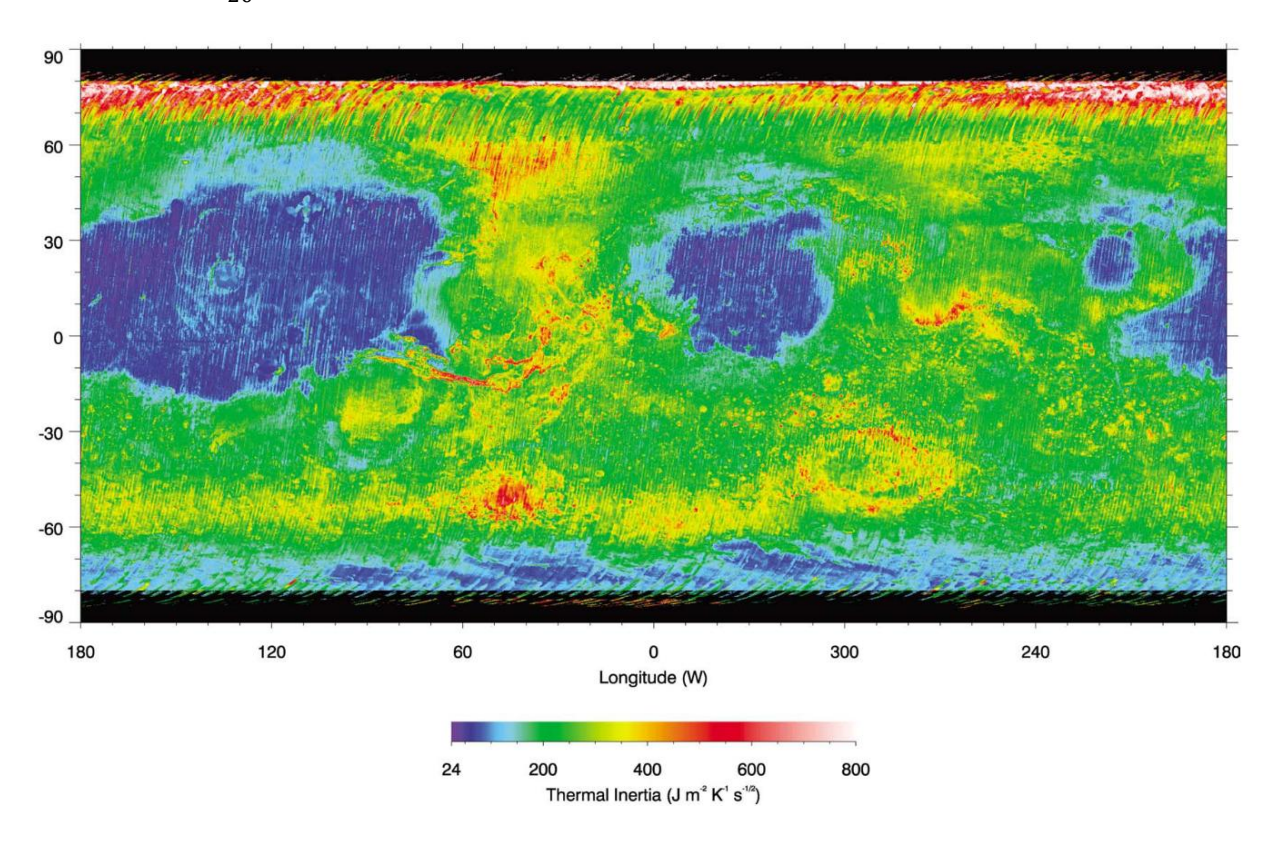


**Figure 9** — Nighttime bolometric thermal inertia map of Mars. Interpolation was applied to fill gaps between TES ground tracks for latitudes spanning 80°S to 80°N (Putzig et al., 2005).

On the other hand, Putzig et al. (2005) used the visible bolometric albedo Figure 10, which is the proportion of incident solar radiation that a surface reflects across the entire visible spectrum; to understand the compositional and structural differences of martian surface materials.

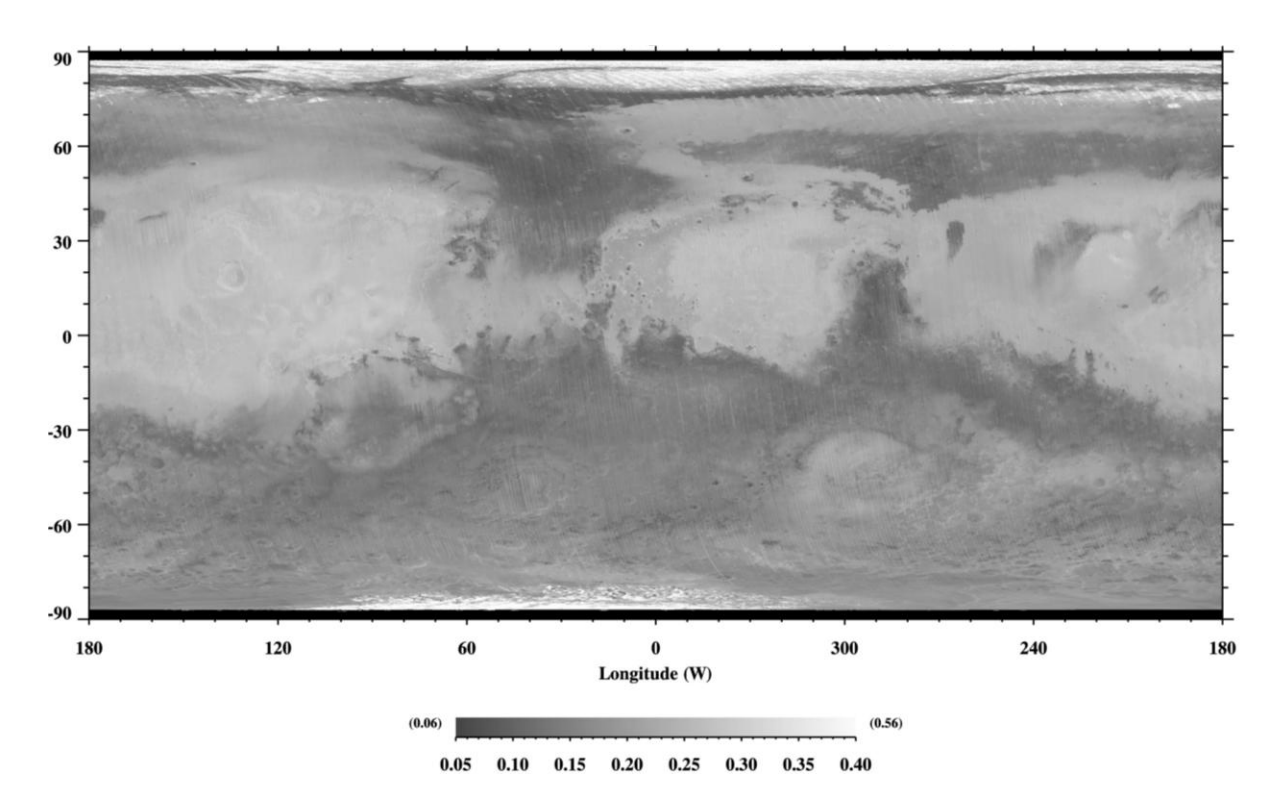


**Figure 10** — TES Albedo for Mars Year 26. Albedo values range from 0 to 1, where 1 indicates a perfectly reflective surface that reflects all incident radiation, and 0 represents complete absorption with no reflection. (Putzig et al., 2005).

To understand the compositional and structural differences of martian surface Putzig et al. (2005) refined the approach of Mellon et al. (2000) -in which three major units were identified and defined by distinct combinations of thermal inertia and albedo- and used a two-dimensional histogram of thermal inertia and albedo data to delineate regions with similar surface properties and define thermophysical mapping units (Figure 11).

This global histogram was constructed from unfilled maps (non-interpolated data), with each pixel weighted—representing 1/20° of surface area—to prevent the disproportionate influence of high-latitude regions. Additionally, the boundaries of the major units were then adjusted to match the three primary peaks in the histogram (units A, B, and C), while bins with fewer than 1,669 occurrences were excluded to maintain clear distinctions between the major units and their outliers (Putzig et al., 2005).

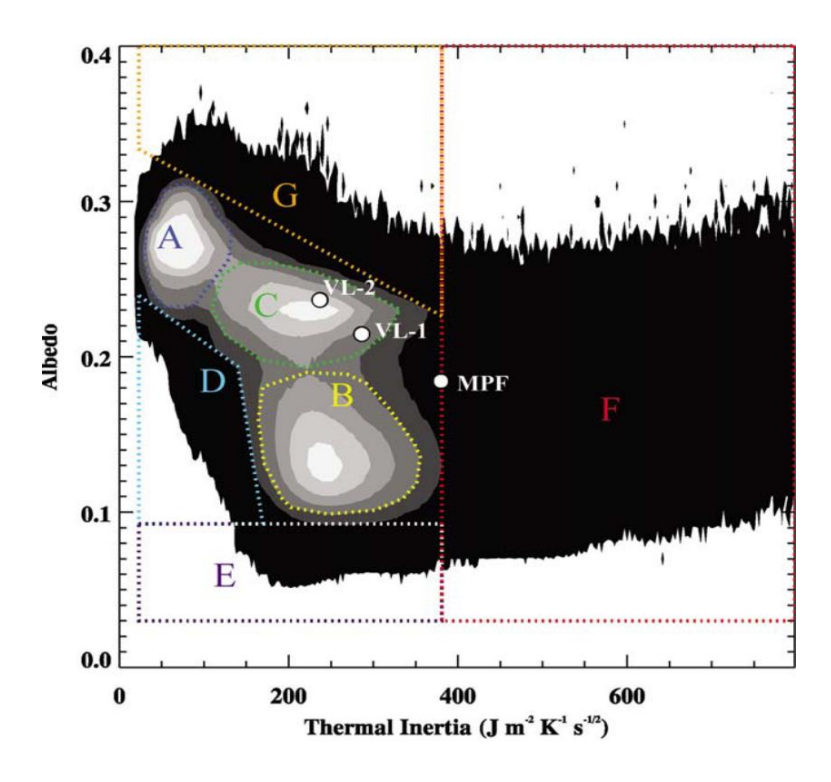


**Figure 11**—Two-dimensional histogram showing the global relationship between TES nighttime bolometric thermal inertia and visible bolometric albedo. White areas indicate no occurrences. Units A, B, and C represent the primary modes of frequent correlation, while outliers are Units D, E, F, and G. (Putzig et al., 2005)

Finally, Putzig et al. (2005) mapped the thermophysical units to their corresponding surface locations, producing a comprehensive global map (Figure 12) that illustrates their spatial distribution across Mars.

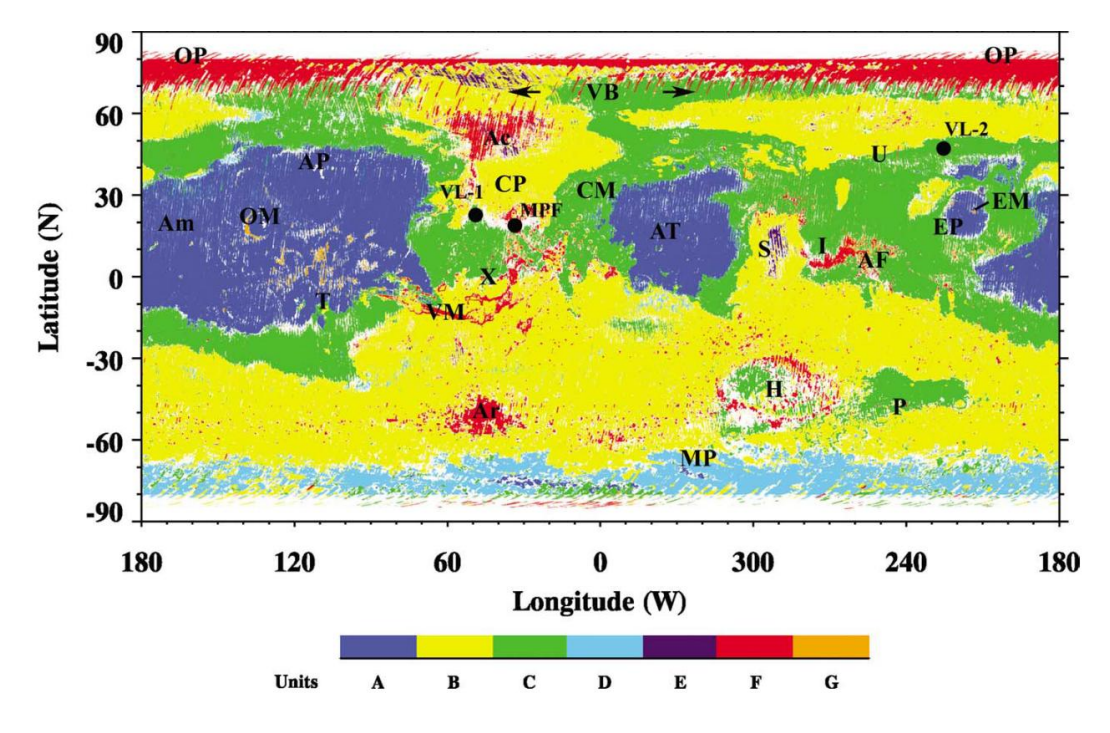


**Figure 12** — Thermal inertia—albedo unit map of Mars. Units represent thermal inertia—albedo modes in Fig. 13. White areas correspond to regions between unit bounds in Fig. 13 (Putzig et al., 2005).

The primary units (A, B, C) cover approximately 78% of the planet's surface, while outlier regions were classified into additional units: (D) low thermal inertia with low-to-intermediate albedo, (E) very low albedo, (F) very high thermal inertia, and (G) very high albedo.

**Table 3** — From filled thermophysical unit map. Each unit is interpreted based on surface properties, such as unconsolidated fines, duricrust, or bedrock, as indicated in the interpretation column. Percent surface area represents the proportional coverage of each unit across Mars. (Putzig et al., 2005).

Mars therm	Mars thermal inertia–albedo units				
Unit	Inertia	Albedo	% surface <sup>a</sup>	Interpretation	
A	Low (28-135)	High (0.23-0.31)	19	Bright unconsolidated fines	
В	High (160-355)	Low (0.10-0.19)	36	Sand, rocks, and bedrock; some duricrust	
C	High (110-330)	Med. (0.19-0.26)	23	Duricrust; some sand, rocks and bedrock	
D	Low (24-170)	Low-med. (0.09-0.24)	2	Low density mantle or dark dust?	
E	High (140-386)	Very Low (< 0.09)	0.3	As B, but little or no fines	
F	Very high (> 386)	All	4	Rocks, bedrock, duricrust, and polar ice	
G	Low-high (40-386)	Very high (> 0.23)	0.7	As A thermally thin at higher inertia	

As observed in Table 3, each thermophysical unit has a specific interpretation, highlighting their significance in selecting a landing site on Mars. According to Golombek et al. (1997), surfaces dominated by bright, unconsolidated fines (i.e., loose dust; Table 3), corresponding to thermophysical unit A, should be avoided. These surfaces are characterized by potentially thick dust deposits, ranging from 1 meter to tens of meters, making them unsuitable for load-bearing and trafficability. Furthermore, radar reflectivity is linked to the bulk density of dry materials, implying that regions with lower bulk density (unconsolidated fines; Thermophysical Unit A) may have surfaces with low radar reflectivity, further reducing their suitability for landing (Golombek et al., 1997). As a result of these considerations, this parameter has consistently been established as a key engineering constraint in various rover and lander missions.

For instance, Grant et al. (2018) established the following engineering constraints and safety values for the Mars 2020 Perseverance Rover mission, further emphasizing the critical importance of this engineering constraint in ensuring mission success (Table 4).

**Table 4** — Load Bearing Surface landing site engineering constraint and safety criteria for the Mars 2020 rover.

Taken and Edited from Grant et al., (2018).

Engineering Parameter	Requirement for Landing Sites	Notes/Rationale
Load Bearing Surface	Not dominated by dust	Thermal inertia $>$ 100 J m-2 s $-$ 0.5 K-1 and albedo $<$ 0.25; radar reflectivity $>$ 0.01 for load bearing bulk density <sup>a</sup>

Together, these findings establish a framework for understanding how thermal inertia and albedo variations reveal the composition, mechanical properties and radar reflectivity of Martian surfaces, with thermophysical units serving as the critical indicators. This knowledge

is vital for selecting landing sites that not only meet engineering constraints but also ensure the stability, functionality, and operability of robotic missions, particularly by avoiding surfaces dominated by loose dust or unconsolidated fines (M. Golombek et al., 2012; Putzig et al., 2005).

#### 2.5 SCIENCE CRITERIA FOR ASSESSING CANDIDATE SITES

The selection of rover landing sites requires balancing engineering constraints and safety criteria with scientific objectives to ensure both mission feasibility and scientific return. While engineering and safety considerations are fundamental for a successful landing and long-term operability, scientific goals play a crucial role in determining the final site (Grant et al., 2018). Rigorous site selection is essential, as it directly impacts the rover's ability to achieve its science objectives (Table 1).

Table 5 from Grant et al. (2018) presents an example of scientific criteria used to evaluate potential landing sites for the Mars 2020 Perseverance mission.

**Table 5** — Science criteria for assessing candidate Sites at third 2020 landing site workshop (Grant et al., 2018).

Criterion 1	The site is an astrobiologically-relevant ancient environment and has geologic diversity that has the potential to yield fundamental scientific discoveries when it is a) characterized for the processes that formed and modified the geologic record; and b) subjected to astrobiologically-
	relevant investigations (e.g., assessment of habitability and biosignature preservation potential). (scoring: $1 = \text{lowest potential}$ , $5 = \text{highest potential}$ )
Criterion	A rigorously documented and returnable cache of rock and regolith
2	samples assembled at this site has the potential to yield fundamental
	scientific discoveries if returned to Earth in the future. (scoring:
	1 = lowest potential, $5 =$ highest potential)
Criterion	There is high confidence in the assumptions, evidence, and any
3	interpretive models that support the assessments for Criteria 1 and 2 for this site. (scoring: $1 = lowest$ confidence, $5 = highest$ confidence)
Criterion	There is high confidence that the highest-science-value regions of
4	interest at the site can be adequately investigated in pursuit of Criteria 1
	and 2 within the prime mission. (scoring: $1 =$ lowest confidence,
	5 = highest confidence)
Criterion	The site has high potential for significant water resources that may be of
5	use for future exploration—whether in the form of water-rich hydrated
	minerals, ice/ice regolith or subsurface ice. (scoring: 1 = lowest
	potential, 5 = highest potential)

Consequently, during the site selection process, it is common for scientifically promising locations to be excluded after evaluating the risks that could occur during the landing or roving phases. In the end, the chosen site represents the most balanced compromise between scientific objectives and engineering constraints (Pajola et al., 2019).

#### 2.6 MARS COLONIZATION

Mars, in particular, stands out as a prime candidate for colonization due to its relative proximity and similarities to Earth's environment compared to other celestial bodies (Campa et al., 2019)

But what makes Mars settlements desirable? One of the main rationales is the need to safeguard humanity from existential-catastrophic threats such as global pandemics, nuclear war, severe climate change, ecological collapse, uncontrollable artificial intelligence, supervolcanic eruptions, or asteroid impacts all pose significant risks to human survival. Additionally, unforeseen dangers may emerge, further underscoring the necessity of establishing a self-sustaining presence beyond Earth (J. Leslie, 2020; Ord, 2020; Rees, 2003; Puumala et al., 2023). Another of the driving forces behind extraterrestrial expansion is resource utilization. Celestial bodies contain valuable materials and energy sources, making space mining a potentially lucrative endeavor (Campa et al., 2019). Moreover, other key rationales identified in favor of Mars colonies are scientific exploration, inspiration and discovery (Puumala et al., 2023).

Therefore, while significant challenges remain, the growing interest in Mars colonization—whether through robotic missions or eventual human settlement—represents a crucial step in humanity's efforts to expand beyond Earth (Campa et al., 2019).

#### 2.6.1 THE ROLE OF ROBOTS IN MARS COLONIZATION

The ability of robots to function in hazardous environments minimizes risks and challenges for human colonization in Mars and ensures long-term viability of settlements (Schulze-Makuch & Irwin, 2008; Campa et al., 2019).

In such challenging conditions, precursor robotic missions to Mars that involve teams of multiple cooperating robots (Huntsberger et al., 2000) will be essential for long-term operations, as they could autonomously or semi-autonomously prepare the Martian surface by performing tasks too dangerous or inefficient for humans, including scientific research, maintaining life support systems, resource extraction-transport and infrastructure development; with robots laying the groundwork and humans building upon it (Campa et al., 2019; Schulze-Makuch & Irwin, 2008; Huntsberger et al., 2000).

Additionally, as highlighted by Huntsberger (2001), robot assistance will continue even after human settlers arrive, playing a crucial role in maintaining support, managing resources, and expanding infrastructure to ensure the colony's long-term sustainability; and as their capabilities

advance, they will take on increasingly complex tasks, further contributing to Mars' self-sufficiency.

#### 2.6.2 HUMAN HABITABILITY IN MARS

Crews for Mars missions rely on current or developing technologies, yet many challenges must be resolved for selecting a habitable landing site, safe landing, and sustainable presence. Although technological advancements may overcome these obstacles, strict Martian conditions could still limit mission success (Puumala et al., 2023).

A recent study by Zhu et al. (2025) employed an Analytic Hierarchy Process (AHP) model to determine the most suitable locations for human habitats on Mars. The study developed two distinct AHP models—one for aboveground habitats and another for underground habitats—recognizing that the relative importance of each criterion varies between these settings. Figure 13 and Figure 14 present the resulting suitability maps for both models. The analysis considered several key criteria, including surface temperature, dust opacity, dust storm frequency, slope, and water ice consistency as measured by SWIM (Morgan et al., 2021; Putzig et al., 2023).

This work, as noted by Zhu et al. (2025), introduces an innovative, adaptable framework that provides a fresh interdisciplinary perspective on analyzing human habitation environments for future Martian exploration and can be modified to align with various emerging technological scenarios.

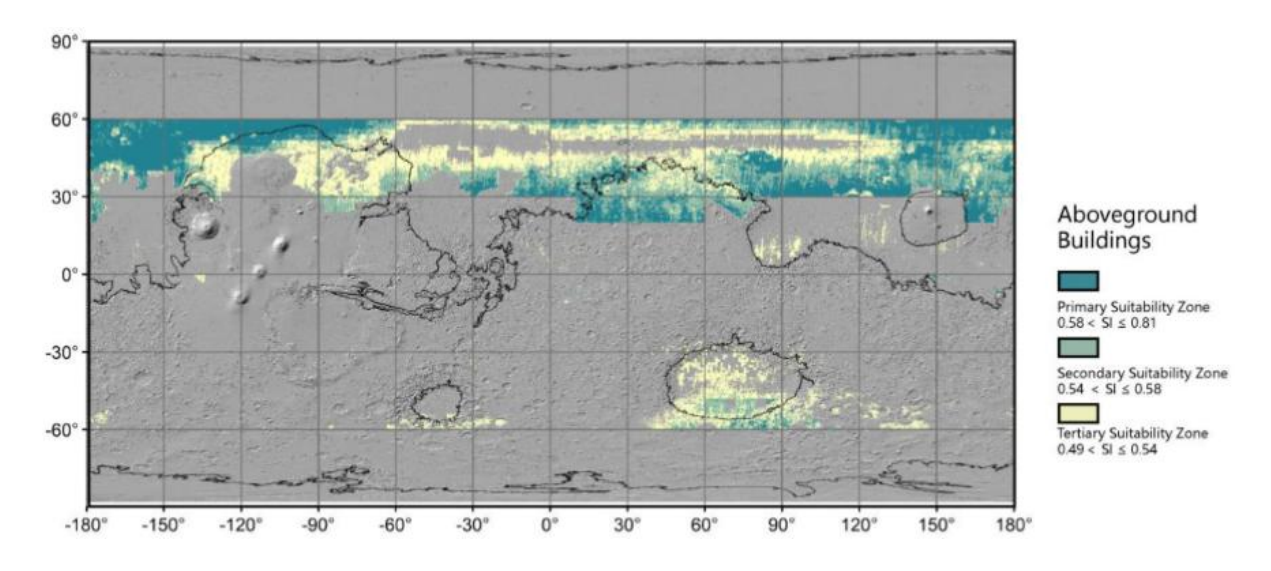


**Figure 13** — Suitability maps from Zhu et al. (2025) for aboveground building sites on Mars, generated using an AHP model. Three suitability zones—Primary, Secondary, and Tertiary—are shown.

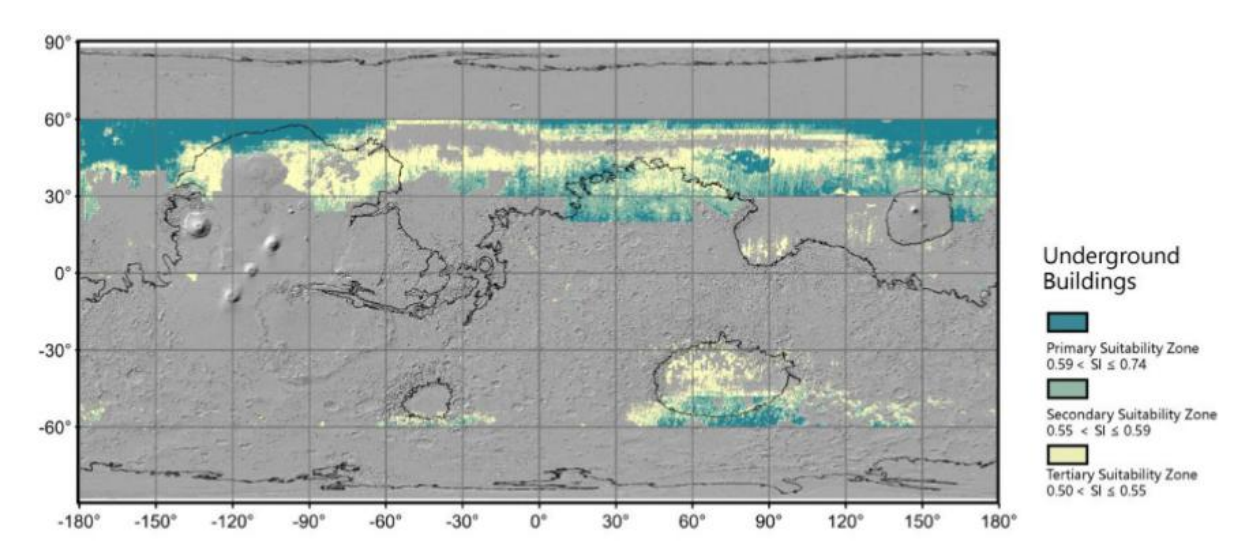


**Figure 14** — Suitability maps from Zhu et al. (2025) for underground building sites on Mars, generated using an AHP model. Three suitability zones—Primary, Secondary, and Tertiary—are shown.

Furthermore, other studies have centered in identifying key obstacles and criteria for crewed missions and permanent Mars settlements, grouping them into five main categories: Survival, Water, Energy, Habitat, and In-situ Resources (Puumala et al., 2023). In the following subsections, we delve deeper into these challenges and criteria, examining each in detail to highlight their relevance for future exploration efforts.

#### 2.6.2.1 SURVIVAL ON MARS

Despite certain geological similarities between Earth and Mars, including rocky landscapes shaped by erosion and sedimentation, the Martian environment is fundamentally different and poses significant challenges to sustaining terrestrial life (Puumala et al., 2023).

Mars' surface conditions are extremely hostile to unprotected humans. The planet's thin atmosphere, which has an oxygen concentration of only 0.13%, combined with its low atmospheric pressure, would quickly lead to asphyxiation due to hypoxia (Verseux et al., 2016; Puumala et al., 2023). Additionally, the low pressure would result in the rapid formation of gas bubbles in the blood within the lung vesicles, a condition comparable to severe decompression sickness experienced by divers (Puumala et al., 2023).

Radiation exposure on Mars is another major concern. The planet's surface is bombarded by high-intensity ultraviolet radiation, which is over 1,000 times more biologically harmful than the levels experienced on Earth, posing a severe risk to living organisms (Puumala et al., 2023).

In addition to radiation and atmospheric challenges, Mars' extreme temperatures create further obstacles for human survival. Similar to Earth, temperature variations depend on latitude,

season, and time of day. However, daily temperature fluctuations in the equatorial region can be drastic, reaching up to 100°C—ranging from daytime highs around 20°C to nighttime lows near -120°C. The planet's global average temperature remains around -60°C, which is far from suitable for most terrestrial organisms, including warm-blooded animals and plants (Verseux et al., 2016; Puumala et al., 2023).

Mars' frequent and prolonged dust storms introduce yet another hazard for both human physiology and technological systems. The planet's fine, sharp dust particles are easily lifted into the atmosphere, creating abrasive conditions that can damage equipment and pose respiratory risks. Given these extreme environmental factors, survival on Mars requires continuous protection, either through specialized spacesuits for short-term exposure or entirely sealed habitats for long-term habitation (Puumala et al., 2023).

Moreover, the planet's reduced gravity—approximately one-third of Earth's—poses physiological challenges, potentially leading to muscle atrophy and bone density loss over extended missions. These physical effects, coupled with the psychological strain of isolation and confinement, could significantly impact the well-being of astronauts (Amini et al., 2022; Puumala et al., 2023). Collectively, these stressors could threaten the endurance and survival of crew members, ultimately affecting the success and feasibility of human missions to Mars.

#### 2.6.2.2 WATER

Due to Mars' extremely low atmospheric pressure and cold temperatures, liquid water cannot persist on the surface. Instead, it either rapidly evaporates or freezes, while exposed ice deposits quickly sublimate. However, small ice deposits have been identified near the surface (Piqueux et al., 2019; Puumala et al., 2023), and significant reservoirs of subsurface water ice have been mapped through orbital remote sensing (Boynton et al., 2002; Vincedon et al., 2010; Carr, 2015; Dundas et al., 2018). According to Byrne et al. (2009) water ice should be stable decimeters to about 1 meter below the martian surface at latitudes poleward of about 40°.

For mission planning, accurately identifying and characterizing local water sources is a crucial step, especially when preparing for a potential base camp or long-term settlement. Extracting, storing, and transporting water require specialized infrastructure and logistical planning (Mellerowicz et al., 2022; Puumala et al., 2023). As a precaution, a portion of the water supply must also be transported from Earth to ensure crew safety (Heldmann et al., 2022; Puumala et al., 2023).

Beyond human consumption, water is indispensable for numerous other applications, including fuel production. Generating the necessary oxygen and methane for the return journey of a SpaceX vehicle, for example, would require approximately 600 tons of water, equivalent to an ice volume of around 730 m³—a cube roughly 9 meters per side (Heldmann et al., 2022; Puumala et al., 2023). Water is also essential for plant cultivation, habitat maintenance, laundry, dust suppression, and processing Martian regolith into a cement-like material for construction (Amini et al., 2022; Heldmann et al., 2022; Puumala et al., 2023; Starr, 2020).

Neutron spectroscopy is a vital technique for evaluating the water content in the Martian subsurface. The Fine Resolution Epithermal Neutron Detector (FREND) aboard the ExoMars TGO enables the creation of highly detailed localized maps of Water Equivalent Hydrogen (WEH) in the upper meter of Mars (Figure 15) (Malakhov et al., 2022). The global map produced in this study reveals intricate features and areas with notably high-water content, reaching up to 20 wt% WEH, which is unexpected for moderate latitudes where free water and ice are typically unstable. In this context, "water" likely refers to hydrogen in bound forms, such as within hydrated minerals or as adsorbed water, though it is also possible that some of it could be present as ice, but not as liquid due to the instability of liquid water on Mars (Malakhov et al., 2022).

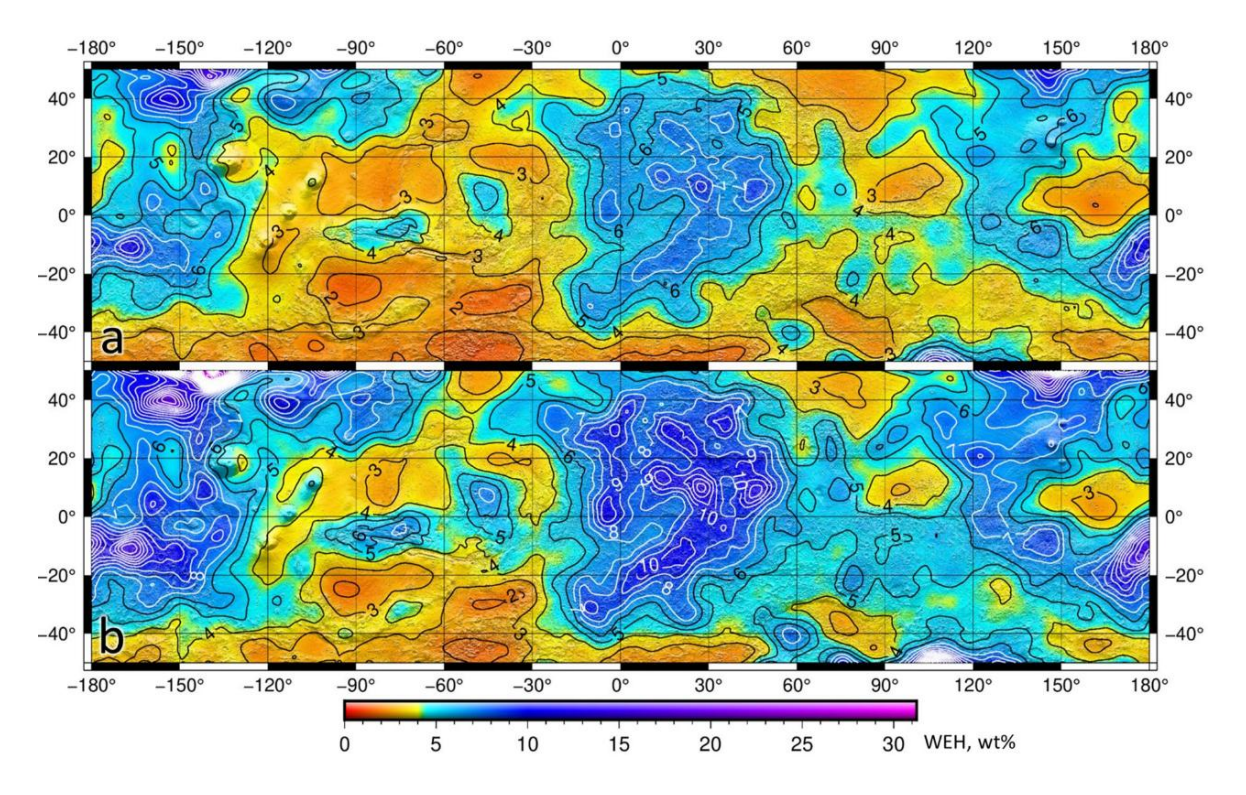


**Figure 15** — The minimum (top) and maximum (bottom) Water Equivalent Hydrogen (WEH) maps from 50°N to 50°S, display the range of potential values, accounting for measurement uncertainties with  $+\sigma$  and  $-\sigma$  (Malakhov et al., 2022).

As seen in Figure 15, the map extends from 50° north to 50° south latitudes. This is due that polar regions experience significant seasonal fluctuations in neutron flux, influenced by atmospheric CO2 deposition, which requires further dedicated research (Malakhov et al., 2022).

Moreover, Malakhov et al. (2022) highlights that some studies in the past from Byrne et al., (2009) suggested the possibility of water ice existing in the Martian subsurface, even near the equator, under specific conditions. Years later, a subsequent study by Watters et al. (2024), examined the Medusae Fossae Formation (MFF), located at the equator -approximately 5° to 25° latitude- (using updated data from the Mars Express MARSIS radar) and discovered that the presumed deposits might be even thicker than previously believed, reaching up to 3.7 km (Figure 16). They found that the radar signals correspond to what would be expected from layers of ice, resembling the signals detected from Mars' polar caps, which are known for their high ice content (Watters et al., 2024).

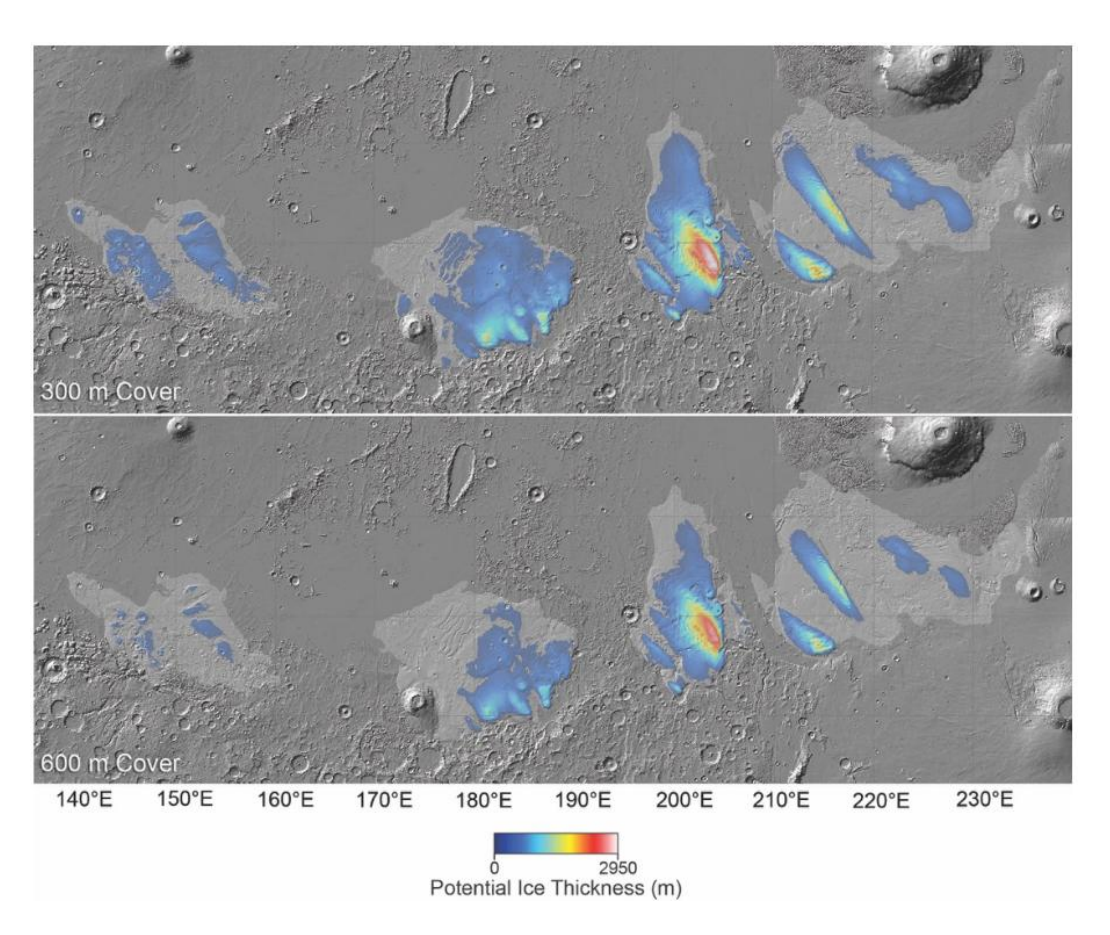


**Figure 16** — Map showing the thickness of the ice-rich portions of the Medusae Fossae Formation (MFF) deposits, with estimated ice volumes ranging from ~2.2 × 10<sup>5</sup> km³ to ~4.0 × 10<sup>5</sup> km³. The boundaries of the MFF deposits have been modified from Tanaka et al. (014) as referenced in Watters et al. (2024).

These studies of mapping water content are crucial for understanding Mars' hydrologic history, and the current state of water on the planet is a key resource for planning future robotic and human missions' ice (Malakhov et al., 2022).

Lastly, regarding the usability of Martian water, it is believed that utilizing Martian water could present challenges, considering that the chemical composition of subsurface water is largely unknown, and it may contain high levels of perchlorates and other toxic salts (Hecht et al., 2009; Georgiou et al., 2017; Puumala et al., 2023). Additionally, organic contaminants or even traces of extinct or extant microbial life could be present. Hence, to make Martian water safe for human use, rigorous purification and continuous quality monitoring would be required (Puumala et al., 2023).

## **2.6.2.3 ENERGY**

The feasibility of Martian settlement hinges on a reliable and sufficient energy supply. Proposed plans assume that part of this energy will be derived from local resources, including solar and wind power, as well as water for hydrogen and methane production (Amini et al., 2022; Heldmann et al., 2022; Puumala et al., 2023; Starr, 2020). While these energy sources are available in varying quantities depending on location, time of day, and season, harnessing them requires specialized infrastructure, such as photovoltaic panels and wind turbines, which must be transported from Earth. However, these methods face challenges, particularly from Martian dust storms. The fine dust particles carried by strong winds can accumulate on solar panels, reducing their efficiency, and potentially interfere with the mechanical components of wind turbines (Puumala et al., 2023). A backup/emergency alternative introduced to past and actual Mars rovers, that could be included in a settlement, is the Radioisotope Thermoelectric Generators (RTGs), which provide a reliable and continuous power by converting heat from the natural radioactive decay of plutonium-238 into electricity (Golombek et al., 2012).

Additionally, to ensure a stable power supply, current mission plans incorporate nuclear fission reactors as a backup for local energy sources. NASA's reference missions suggest the use of multiple 160 kW reactors to meet energy demands (Puumala et al., 2023; Rapp, 2023). Additionally, smaller 10 kW nuclear reactors have been proposed to power the expandable crew habitat, initially designed to support up to nine occupants (Amini et al., 2022; Puumala et al., 2023).

## **2.6.2.4 HABITATS**

The initial crew habitats are envisioned as compact, transportable modules—such as landers, barracks, or spacecraft—that provide essential shelter, radiation shielding, and survival necessities (Amini et al., 2022; Heldmann et al., 2022; Puumala et al., 2023). Long-term habitation on Mars requires structures that are not only functional but also conducive to human well-being. To minimize reliance on transported materials, local resources like regolith and water ice should be extensively utilized for construction. A regolith layer approximately two meters thick could reduce radiation exposure to levels within ESA safety thresholds, while a 90 cm cover might suffice for short-term protection (Puumala et al., 2023; Rostel et al., 2020).

Alternatively, instead of constructing radiation-shielded habitats, astronauts could take advantage of natural shelters such as caves, which offer protection from intense ionizing radiation and ultraviolet exposure. Lava tubes, also referred to as "pyro-ducts," have been proposed as viable locations for long-term Martian settlements (Romioa, 2022). Additionally, according to Schulze-Makuch & Irwin (2008), due to Mars' lower gravitational force of 0.38g, caves on the planet are expected to be significantly larger than their terrestrial counterparts, as reduced gravity allows for wider spans of unsupported rock to remain stable. Moreover, martian caves could help meet the water and oxygen demands, further enhancing their viability as habitat locations (Schulze-Makuch & Irwin, 2008).

Additional challenges for human settlements on Mars include the potential risks posed by ultramafic soils. As highlighted by Vithanage et al. (2019), these soils, rich in trace metals like Cr, Ni, Mn, and Co, present significant concerns for agriculture and human health due to their low nutrient content and the potential for harmful metal mobility. Although extremophile plants have adapted to such environments, understanding these soils is crucial for the success of Martian agriculture.

## 2.7 MARS CLIMATE DATABASE

The Mars Climate Database (MCD) developed by the Laboratoire de Météorologie Dynamique (LMD) (Millour et al., 2022; Millour et al., 2014; Forget et al., 1999), compiles atmospheric statistics from advanced General Circulation Model (GCM) simulations of the Martian atmosphere.

A GCM is a complex mathematical computational model used to simulate the atmospheric evolution of a planet over time -circulation and climate. It solves established Navier–Stokes

equations of motion and thermodynamics across a rotating 3D grid that encompasses the entire martian atmosphere (Millour et al., 2022; Millour et al., 2014; Forget et al., 1999). The LMD Mars GCM incorporates the unique physical processes on Mars, from the surface to the exobase, including radiative transfer, dust and ice aerosols, CO<sub>2</sub> ice condensation and sublimation, and the water cycle -including cloud microphysics-. The model also simulates dust particle transport, atmospheric composition influenced by photochemistry, and local enrichment and depletion of non-condensable gases due to CO<sub>2</sub> processes, along with other various chemical reactions that occur in the atmosphere. Additionally, as it extends into the thermosphere, it can also model ionospheric chemical processes (Millour et al., 2022; Millour et al., 2014; Forget et al., 1999). This model has been rigorously validated with available observational data, representing the best current understanding of Martian atmospheric conditions (Millour et al., 2022; Millour et al., 2014; Forget et al., 1999).

The MCD provides simulated data on a  $5.625^{\circ} \times 3.75^{\circ}$  longitude-latitude grid, extending from the surface to about 300 km altitude. It includes data on temperature, wind, density, pressure, radiative fluxes, atmospheric composition,  $CO_2$  ice surface layers, and convection. Data is averaged and stored twelve times per day for twelve Martian months, covering both annual and diurnal cycles. Each month spans  $30^{\circ}$  in solar longitude (L<sub>s</sub>) and lasts 50-70 days. The database includes data for twelve typical days per grid point, one for each month, and also stores information on intra-month variability and daily fluctuations. Tools are available to reconstruct and synthesize this variability (Millour et al., 2022; Millour et al., 2014; Forget et al., 1999).

On the other hand, according to Millour et al. (2022), Millour et al. (2014) and Forget et al. (1999), in the MCD there are multiple climatology scenarios, climatology scenario is provided with 3 solar EUV conditions: solar min, solar ave, solar max; which the authors define as a simulation using the latest version of the Mars MCD forced by a dust distribution reconstructed from observations over Mars Years 24 to 35, and thus representative of a standard (i.e.: devoided of a planet-encircling global dust storm) Martian year.

Finaly, database was widely used for this geospatial thesis project due to its data availability advantages and because, as noted by Millour et al. (2024), the MCD is designed to support both engineering and scientific research. It is commonly used for entry, descent, and landing (EDL) studies on Mars missions, addressing specific Martian challenges, and analyzing observational data.

## 3. METHODOLOGY

The goal of this project is to identify the most suitable regions on Mars for establishing robotic colonies as precursors to human settlements by using relevant key criteria related to safe landing, robotic operability, and human habitability, based on the literature review (see sections 2.4.2 Landing Site Engineering Constraints and 2.6.2 Human Habitability on Mars, respectively).

## 3.1 METHODOLOGICAL FRAMEWORK

The methodological framework of this project (Figure 17) is mostly divided in two parts: determining the restricted zones for Mars settlements—based on key engineering constraints from the Mars 2020 Perseverance Rover mission (right)—and selecting the most suitable regions for human habitability from within these restricted areas (left). Scientific criteria will not be considered in the selection of the optimal site, as the focus is solely on prioritizing robotic and human preservation without any trade-offs related to scientific investigation.

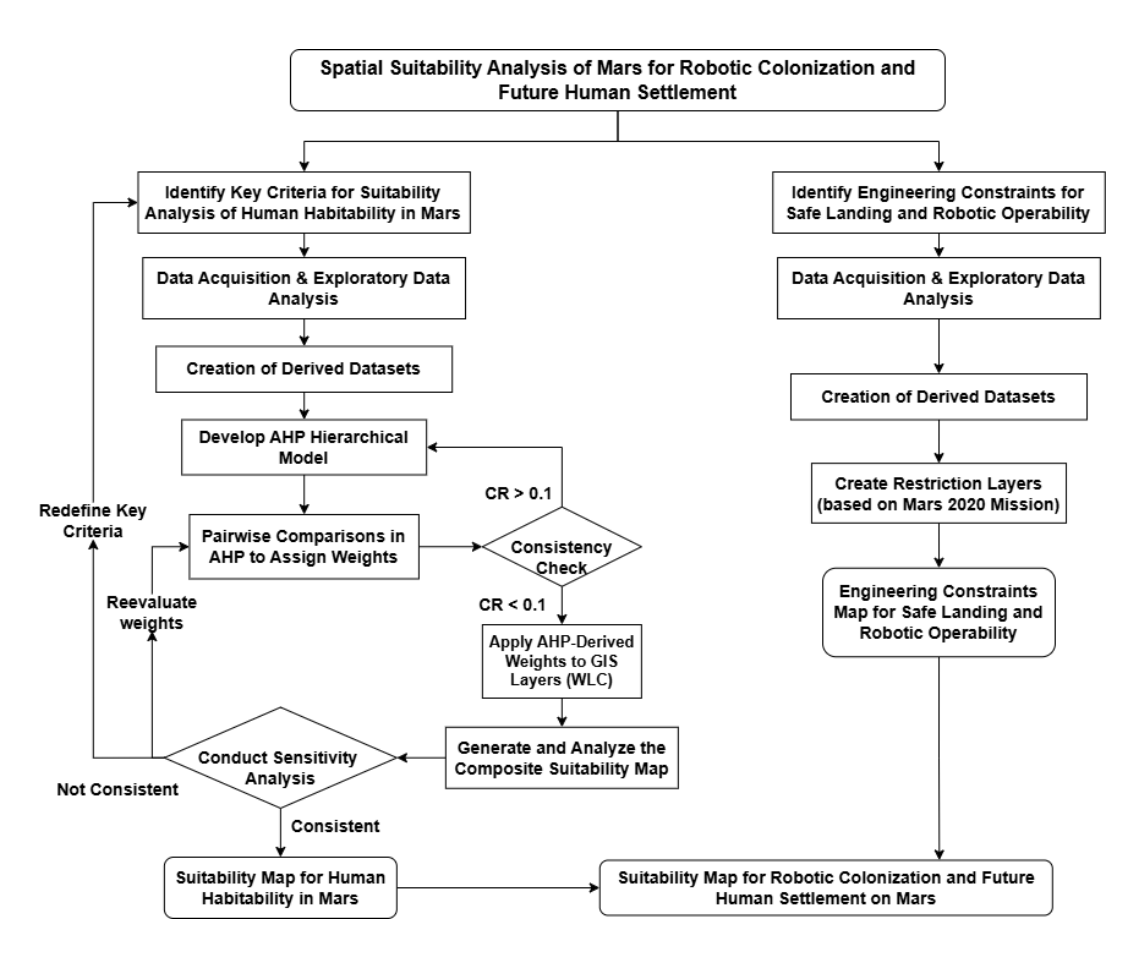


**Figure 17** — Methodological framework for the identification of most suitable regions for robotic colonization and Future Human settlement.

This integrated approach ensures a balanced consideration of both technological limitations and human requirements, aiming to support robotic operability and safe landing while also promoting the long-term sustainability of both precursor robotic and human colony on Mars.

#### 3.2 EXPLORATORY SPATIAL DATA ANALYSIS

## 3.2.1 DATA OVERVIEW

The first step of the methodology (Figure 17) involved acquiring data from multiple sources (Table 6), focusing on engineering constraints for safe landing and robotic operability on Mars, as well as factors critical to the establishment of human colonies.

**Table 6** — Key spatial criteria selected to identify the most suitable Martian regions for robotic colonies as precursors to human settlement, along with their data sources, factor type (Static/Dynamic), seasonal data details and data extent.

Initial Key Criteria	Units	Factor Type	Source	Reference	Seasonal Data	Data Extent
Elevation (DEM)	Meters (m)	Static	MOLA	(Fergason et al., 2018)	No	180°W to 180°E 90°N to 90°S
Water Equivalent Hydrogen (WEH)	wt %	Static	FREND	(Malakhov et al., 2022)	No	180°W to 180°E <b>50°N</b> to <b>50°S</b>
Thermal Inertia	$J\!\cdot\! m^{-2}\!\cdot\! K^{-1}\!\cdot\! s^{-1/2}$	Static	MGS TES	(Putzig et al., 2005)	No	180°W to 180°E <b>80°N</b> to <b>80°S</b>
Albedo	Reflection Index 0 to 1	Static	MGS TES	(Putzig & Mellon, 2007)	No	180°W to 180°E 80°N to 80°S
Surface Temperature	Kelvin (K)	Dynamic	GCM	MCD (Millour et al., 2014, 2022; Forget et al., 1999)	12 Martian Months*	180°W to 180°E 90°N to 90°S
Surface Pressure	Pascal (Pa)	Dynamic	GCM	MCD (Millour et al., 2014, 2022; Forget et al., 1999)	12 Martian Months*	180°W to 180°E 90°N to 90°S
Incoming Radiative Flux to Surface	W/m²	Dynamic	GCM	MCD (Millour et al., 2014, 2022; Forget et al., 1999)	12 Martian Months*	180°W to 180°E 90°N to 90°S

<sup>\*</sup> The solar average EUV was selected as the climatology scenario from the Mars Climate database as it is more representative of a standard Martian year.

Table 6 presents the key criteria selected for analysis, along with their data sources, references, details of seasonal variations, and data coverage. The criteria were classified as either Dynamic or Static, based on their nature and the spatial and temporal scales over which they change.

Notably, the static data corresponds to criteria that exhibit seasonal variation. While, in theory, nearly all of these criteria could be considered dynamic on a small geographical scale and over extended time frames, this geospatial analysis focuses on criteria that change at a large spatial scale and that can be modeled by the General Circulation Model of the Mars Climate Database.

The study area for the entire project was limited to the latitudinal range of 50°N to 50°S, as this represents the maximum coverage available across all datasets (Table 6). This selection is aligned with the considerations outlined in section 2.6.2.2 Water, where it was noted that the polar regions experience significant seasonal variations in neutron flux due to atmospheric CO<sub>2</sub> deposition (Malakhov et al., 2022). Additionally, this range does not pose a major limitation, as one of the key engineering constraints for landing site selection—discussed in section 2.4.2.2 Latitude and Thermal Conditions—requires restricting potential landing areas from 30°N and 30°S toward the poles. Thus, the chosen range effectively balances data availability with operational constraints.

The initial datasets are categorized according to their application in one of the two main methodological approaches: human habitability multi-criteria analysis or engineering constraints for safe landing and robotic operability (Figure 17), with some criteria serving both purposes. Table 7 presents this classification, which is grounded in a comprehensive literature review. This classification ensures that each dataset is applied appropriately within the analytical framework, aligning with the specific requirements of either habitat selection or landing site engineering constraints.

**Table 7** — Classification of initial key criteria based on their application in the methodological framework: human habitability multi-criteria analysis and engineering constraints for safe landing and robotic operability.

Initial Key Criteria	Human Habitability	Engineering Constraints for Safe Landing & Robotic Operability
Elevation (DEM)	✓	✓
Water Equivalent Hydrogen (WEH)	✓	
Thermal Inertia		✓
Albedo		✓
Surface Temperature	✓	✓
Surface Pressure	✓	
Incoming Radiative Flux to Surface	✓	

It is important to note that some of these variables may be reconsidered or removed based on the results of the subsequent exploratory spatial data analysis. If certain criteria exhibit high correlation with others, lack significant variation, or provide limited contribution to the analysis, they may be excluded to enhance the robustness and efficiency of the methodological framework.

## 3.2.2 DATA PREPARATION

## 3.2.2.1 PREPARATION OF SEASONAL DATA

Given the seasonal nature of some of the data, which corresponds to Mars' position in its orbit (as detailed in the Table 8 and Figure 18, with each month representing a specific range of the solar longitude, Ls), it was necessary to average the spaciotemporal data over the entire Martian year. This approach ensured a more representative layer of each of the criteria across the full dataset, accounting for the variability associated with the planet's orbital position.

**Table 8 (Left)** — Mars' Orbital Position (Solar Longitude, L<sub>s</sub>) in Relation to each of the 12 Martian months for the seasonal datasets of the MCD: Surface Temperature, Surface Pressure and Incoming Radiative Flux.

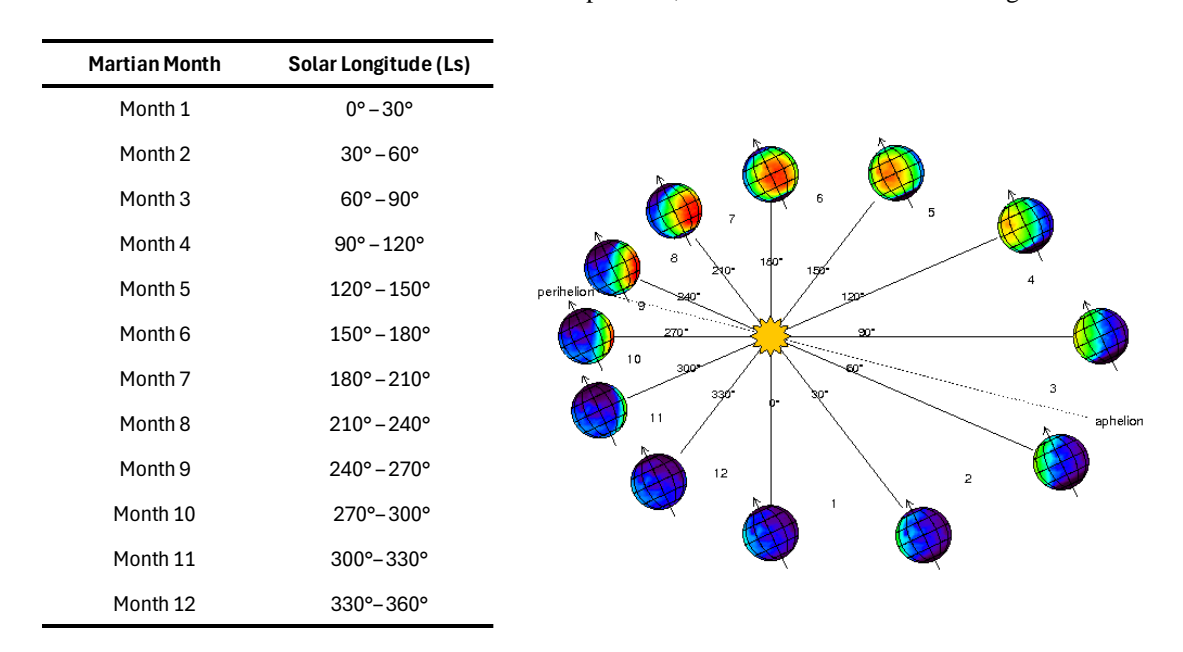


**Figure 18 (Right)**— Mars' Orbital Position in Relation to each of the 12 Martian months for the seasonal datasets of the MCD (Millour et al., 2022; Millour et al., 2014; Forget et al., 1999).

Averaging the seasonal data was a time-intensive process, as each dataset contained one representative day (24 hours) with a 2-hour time interval, for each of the 12 Martian months. Additionally, the datasets were in NetCDF format, a multidimensional scientific file format, requiring additional pre-processing steps to extract the variables for each Martian month. The software used for the entire project was ArcGIS Pro v3.4.

First, the *Multidimensional Raster Layer* ArcGIS Pro tool was used to extract specific datasets—surface temperature, surface pressure and incoming radiative flux to the surface—from the NetCDF files. This process generated 12 spatiotemporal raster layers for each variable (one for each Martian month), resulting in a total of 36 seasonal spatiotemporal raster layers.

Given that the temporal data interval was recorded every 2 hours over a 24-hour period, the next step was to derive the representative day of each Martian month by averaging the spatiotemporal raster data. This was accomplished by using the *Mean* tool from the Summary Statistics toolset at the *Multidimensional* pane. As an example, the process is illustrated below for the surface temperature spatiotemporal data for the representative day of the first Martian month, corresponding to a solar longitude of 0° to 30° (Figure 19 to 30).

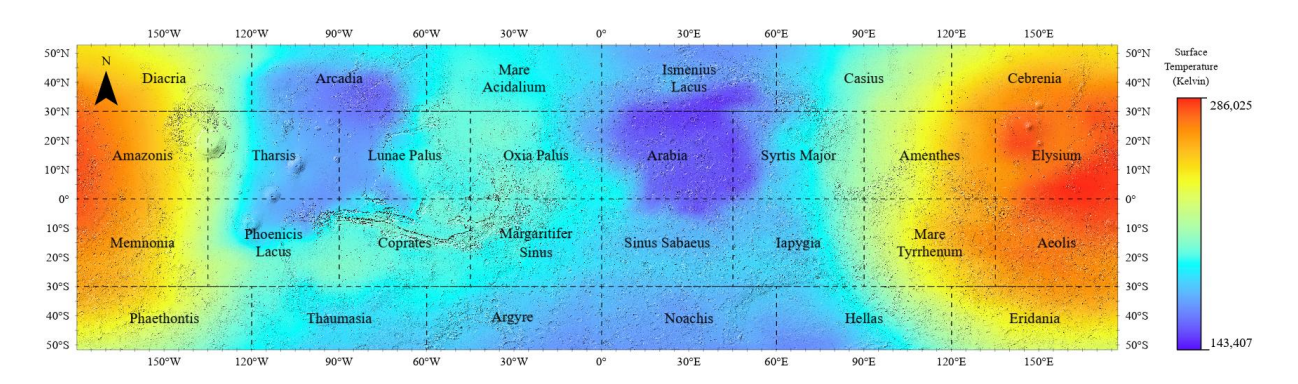


**Figure 19** — Surface temperature layer at 02:00:00, first Martian month (solar longitude 0° to 30°).

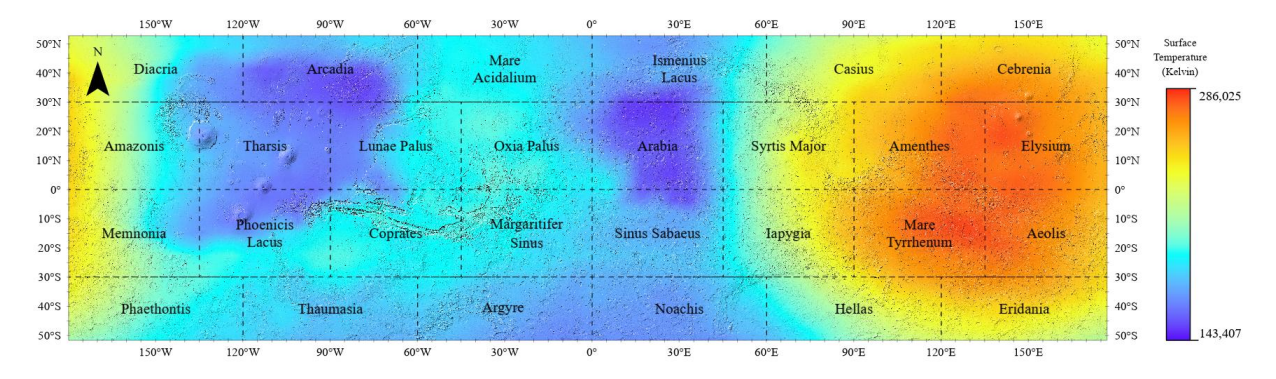


**Figure 20** — Surface temperature layer at 04:00:00, first Martian month (solar longitude 0° to 30°).

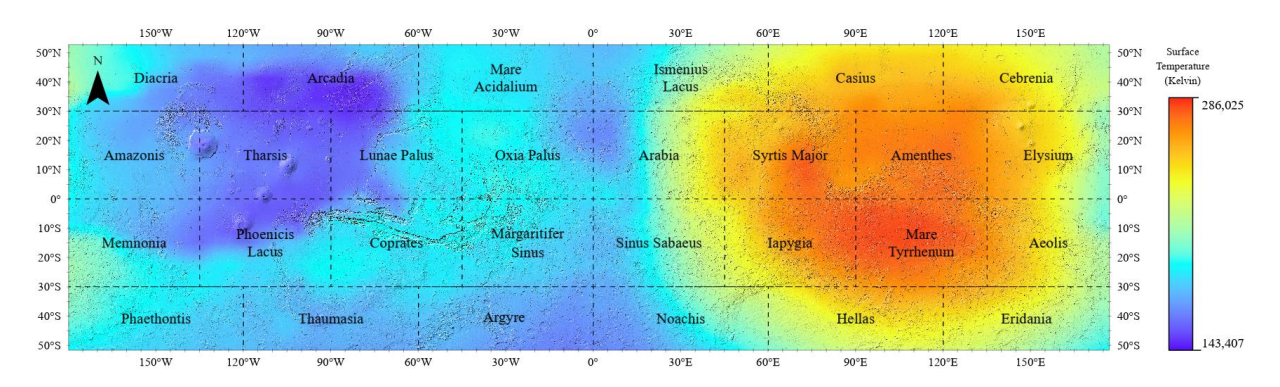


**Figure 21** — Surface temperature layer at 06:00:00, first Martian month (solar longitude 0° to 30°).

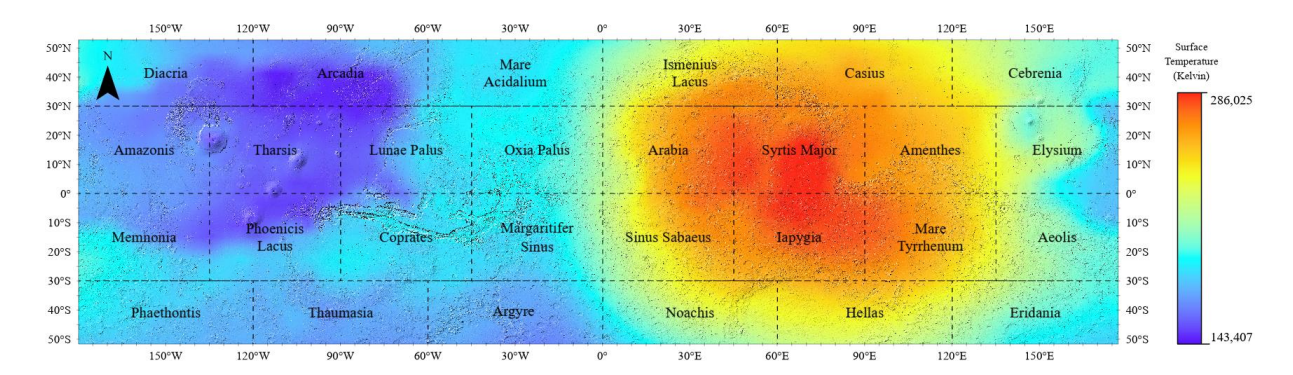
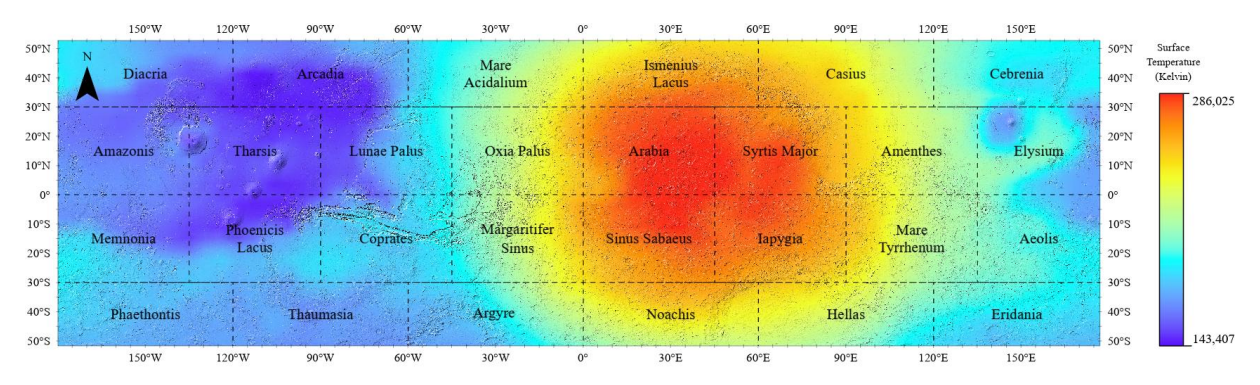
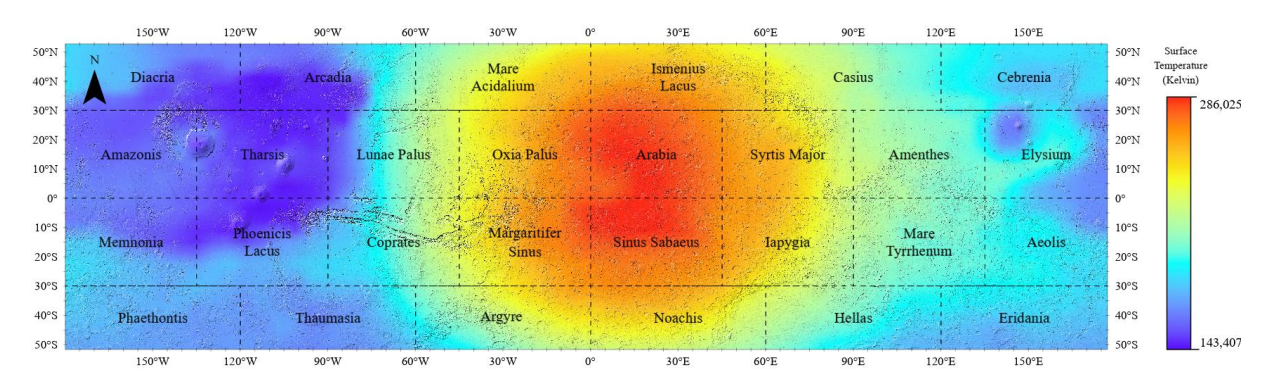


Figure 22 — Surface temperature layer at 08:00:00, first Martian month (solar longitude 0° to 30°).



**Figure 23** — Surface temperature layer at 10:00:00, first Martian month (solar longitude 0° to 30°).



**Figure 24** — Surface temperature layer at 12:00:00, first Martian month (solar longitude 0° to 30°).

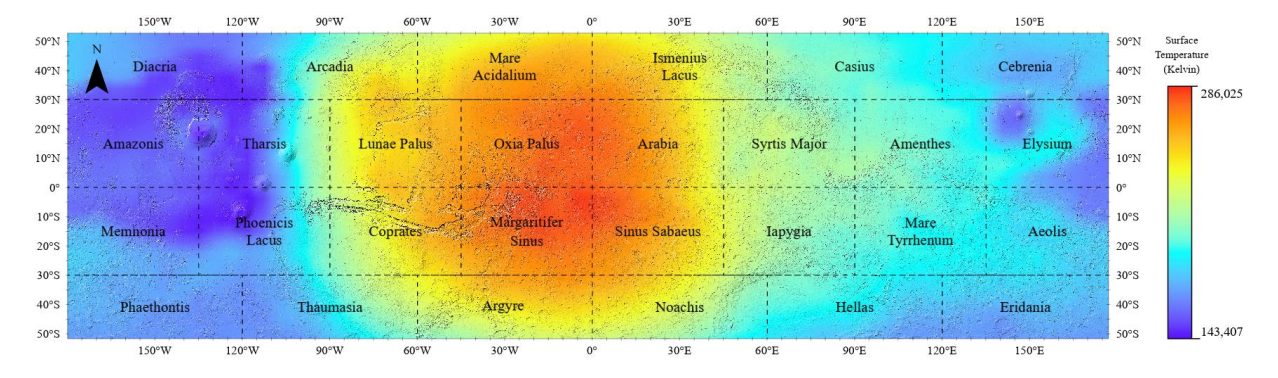


**Figure 25** — Surface temperature layer at 14:00:00, first Martian month (solar longitude 0° to 30°).

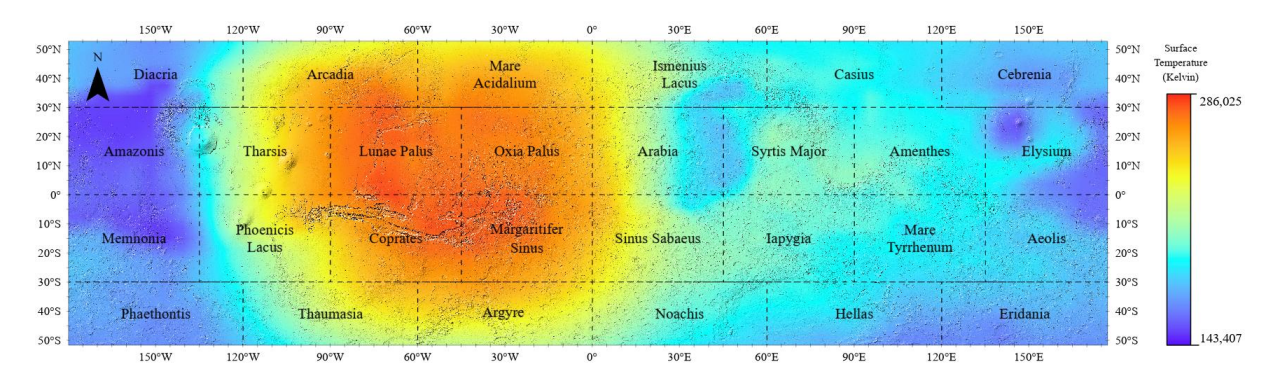


**Figure 26** — Surface temperature layer at 16:00:00, first Martian month (solar longitude 0° to 30°).

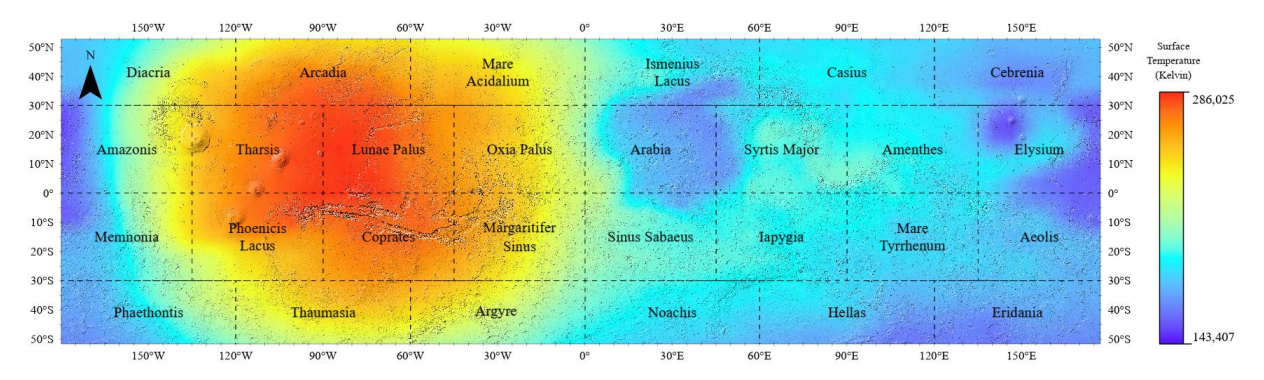


**Figure 27** — Surface temperature layer at 18:00:00, first Martian month (solar longitude 0° to 30°).

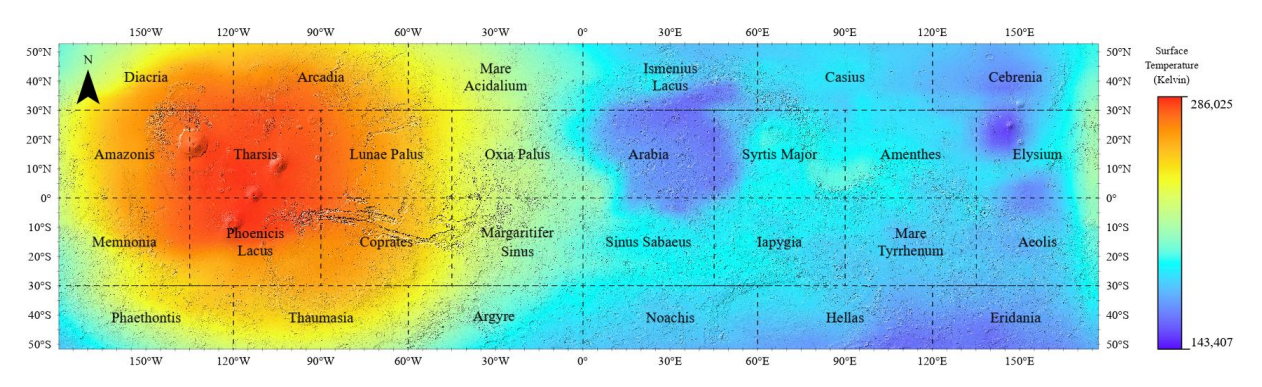


**Figure 28** — Surface temperature layer at 20:00:00, first Martian month (solar longitude 0° to 30°).

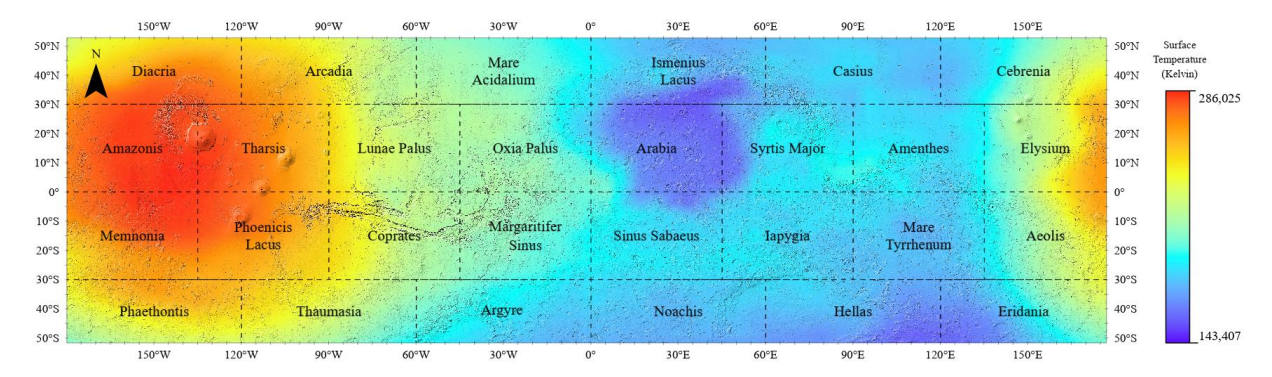


**Figure 29** — Surface temperature layer at 22:00:00, first Martian month (solar longitude 0° to 30°).

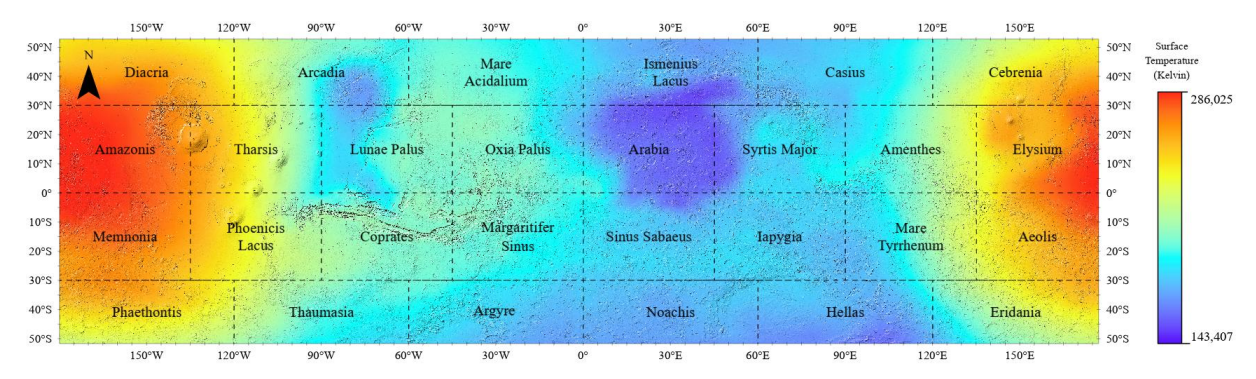


**Figure 30** — Surface temperature layer at 00:00:00, first Martian month (solar longitude 0° to 30°).

The process shown in Figures 19 to 30 using the surface temperature data was also applied to all the seasonal datasets to obtain the respective representative mean day for each Martian month in the form of a non-spatiotemporal raster dataset. The result of the example is presented in Figure 31, which depicts the mean raster for the 1<sup>st</sup> Martian Month, created by calculating the average pixel value across all slices (Figure 19 to Figure 30) within the interval.

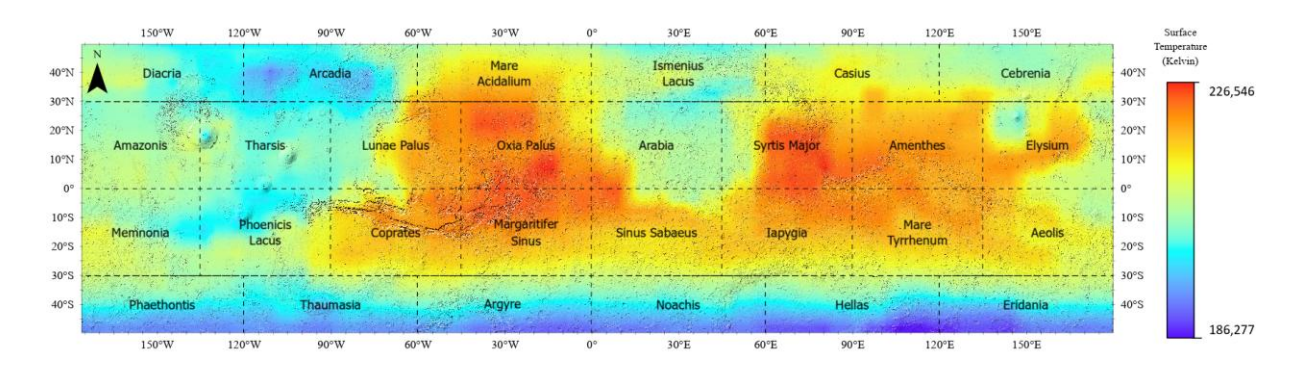


**Figure 31** — Mean surface temperature layer of the 1st Martian month (solar longitude of  $0^{\circ}$  to  $30^{\circ}$ ).

For later visualization of the example, the mean surface temperature layers for the remaining Martian year (months  $2^{nd}$  to  $12^{th}$ ), are shown in Figures 32 to 42.

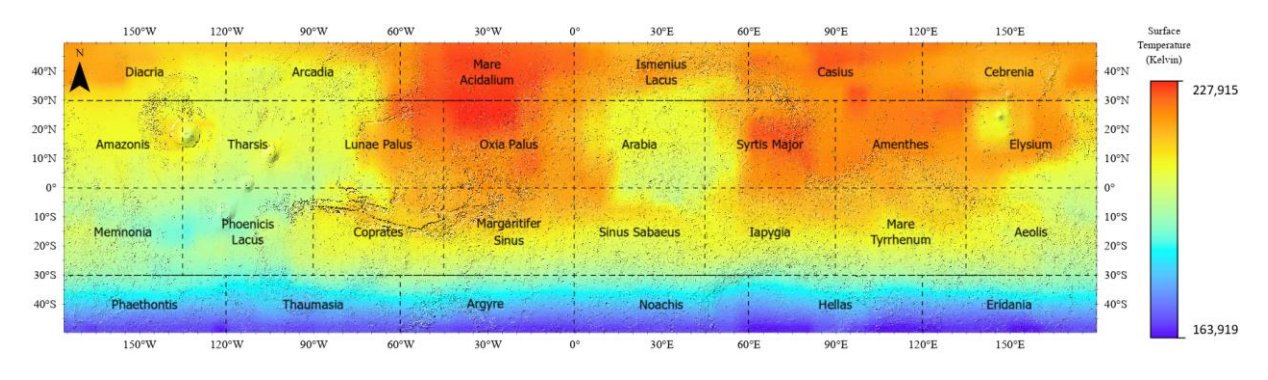


**Figure 32** — Mean surface temperature layer of the 2nd Martian month (solar longitude of 30° to 60°).

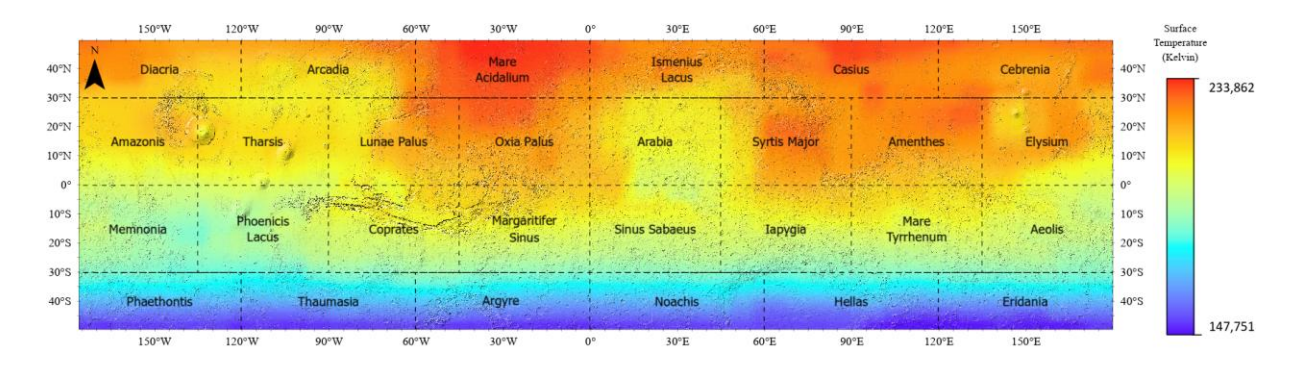


Figure 33 — Mean surface temperature layer of the 3<sup>rd</sup> Martian month (solar longitude of 60° to 90°).

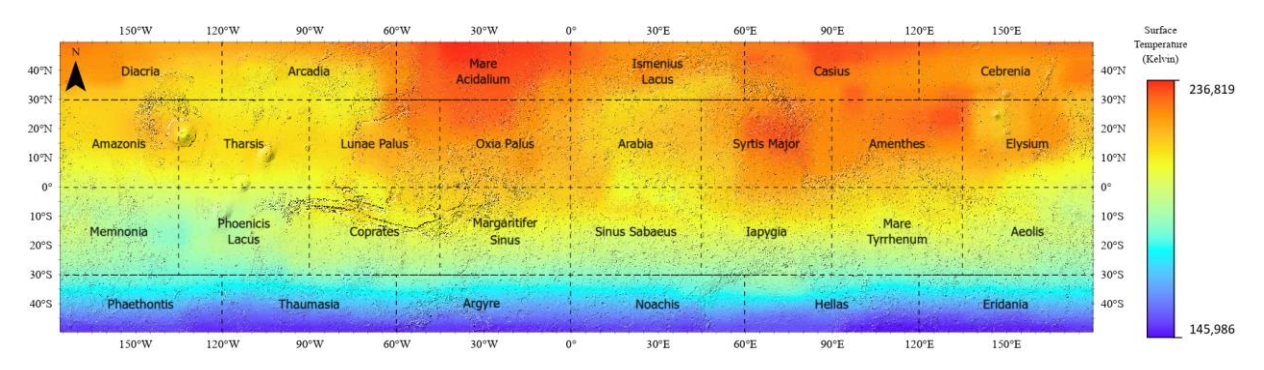


Figure 34 — Mean surface temperature layer of the 4<sup>th</sup> Martian month (solar longitude of 90° to 120°).

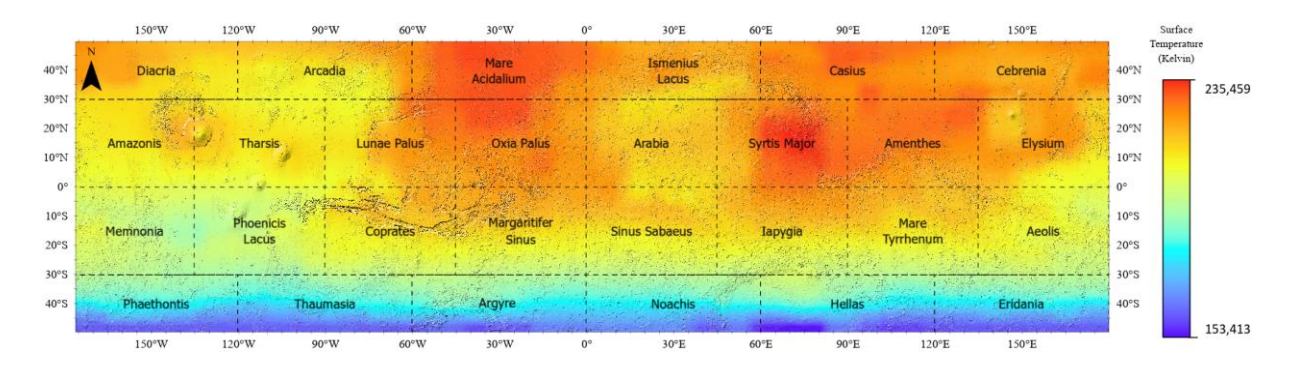


Figure 35 — Mean surface temperature layer of the  $5^{th}$  Martian month (solar longitude of  $120^{\circ}$  to  $150^{\circ}$ ).

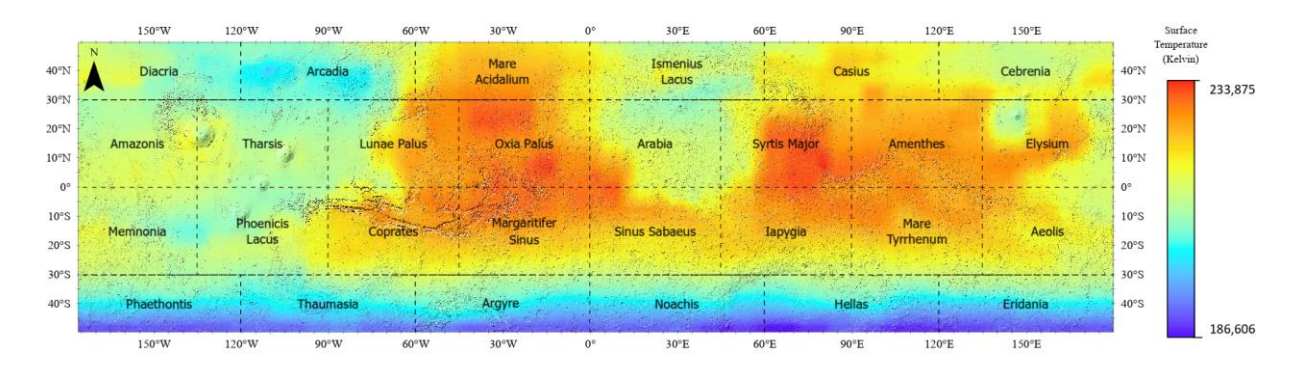


Figure 36 — Mean surface temperature layer of the 6th Martian month (solar longitude of 150° to 180°).

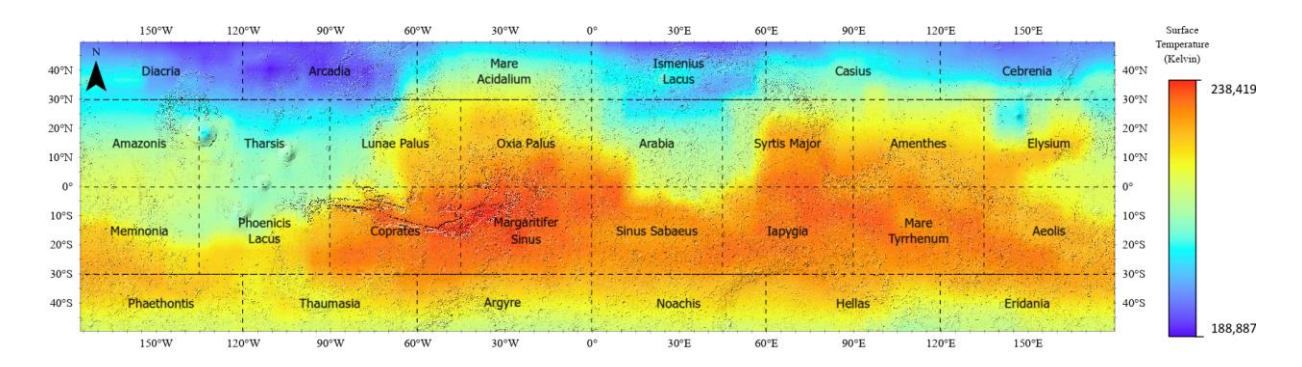


Figure 37 — Mean surface temperature layer of the 7<sup>th</sup> Martian month (solar longitude of 180° to 210°).

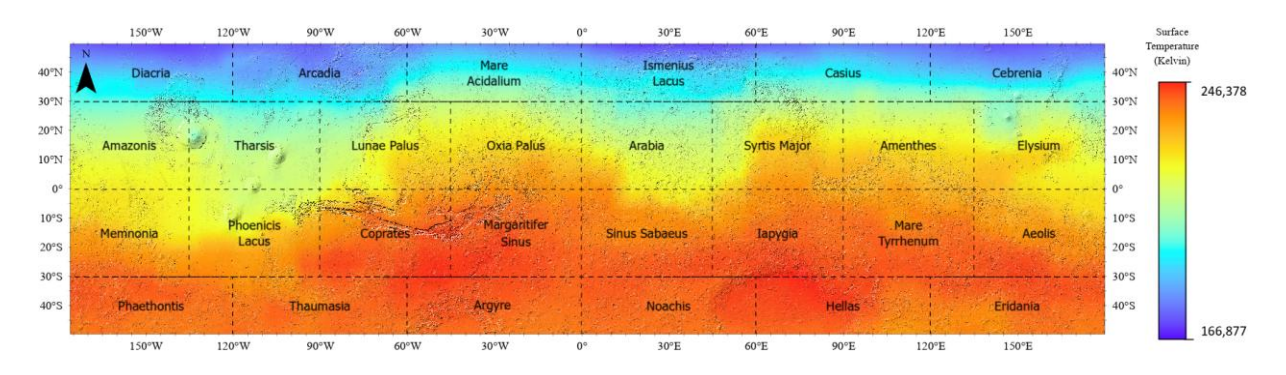
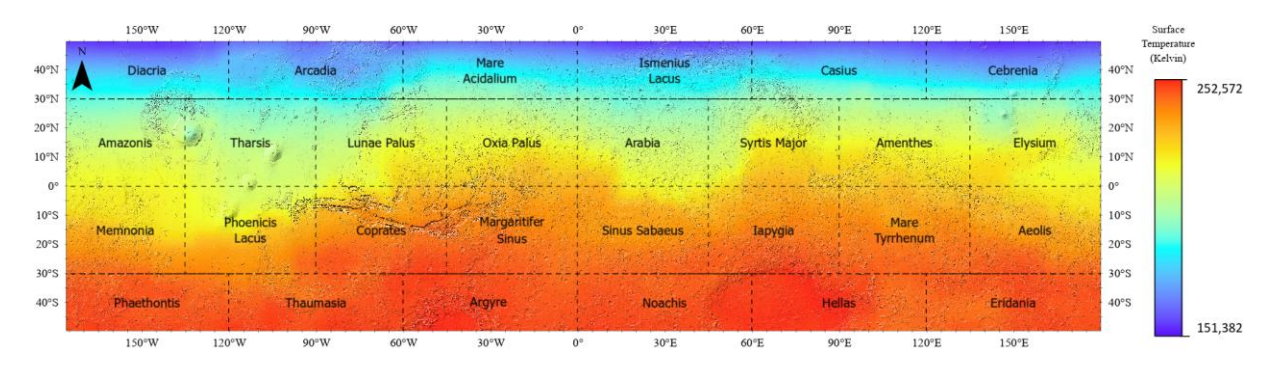
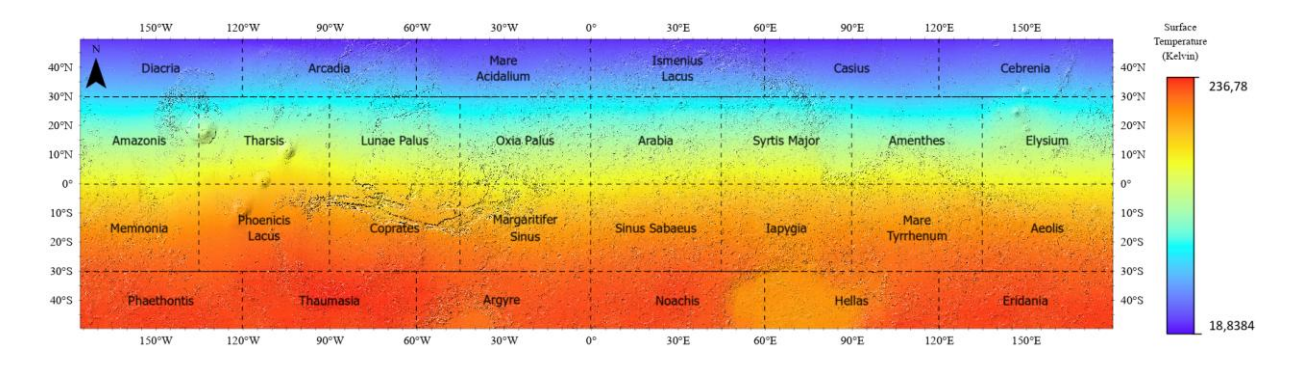


Figure 38 — Mean surface temperature layer of the 8<sup>th</sup> Martian month (solar longitude of 210° to 240°).



**Figure 39** — Mean surface temperature layer of the 9<sup>th</sup> Martian month (solar longitude of 240° to 270°).



**Figure 40** — Mean surface temperature layer of the 10<sup>th</sup> Martian month (solar longitude of 270° to 300°).

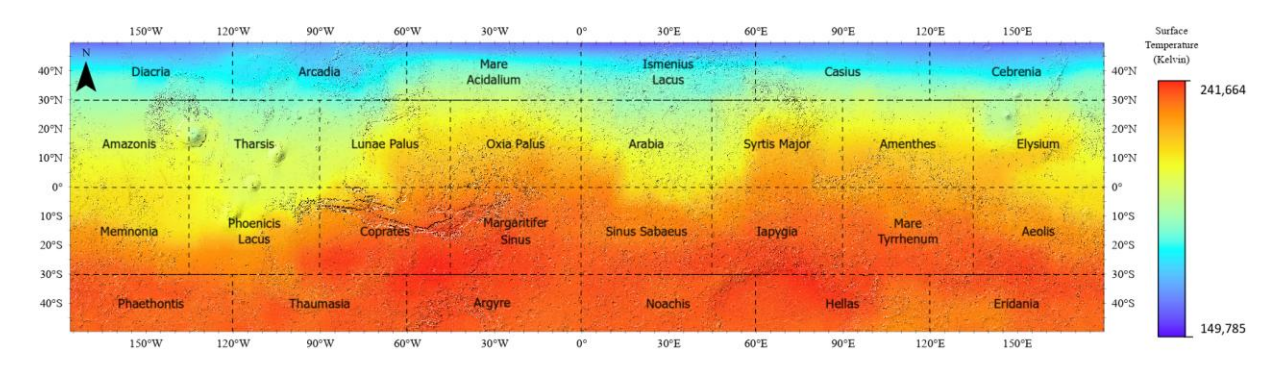


**Figure 41** — Mean surface temperature layer of the 11<sup>th</sup> Martian month (solar longitude of 300° to 330°).

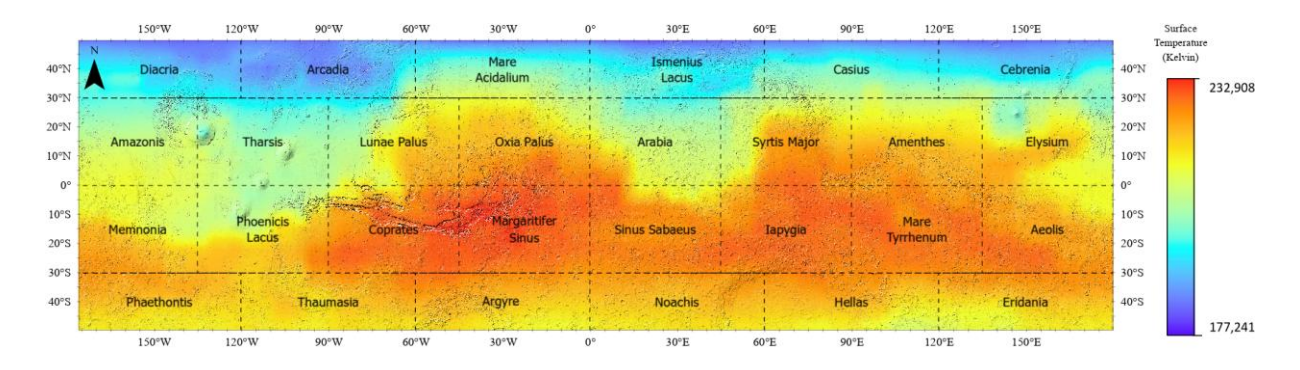


Figure 42 — Mean surface temperature layer of the 12th Martian month (solar longitude of 330° to 360°).

Subsequently, to obtain a representative layer for the entire Martian year from the Monthly data from Figures 32 to 42, the 12 Martian months of each dataset were averaged using the Cell Statistics tool, covering the full range of solar longitude from 0° to 360° (Figure 43).

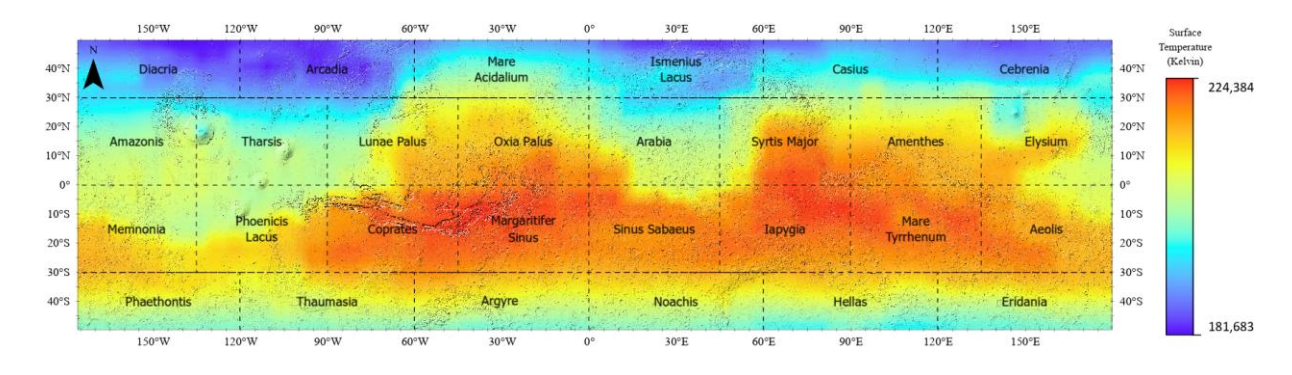


Figure 43 —Surface temperature layer representative of a standard Martian year.

The example shown above for the surface temperature and the above explained method was also applied to all seasonal datasets. Obtaining a representative dataset for a complete Martian year (solar longitude from  $0^{\circ}$  to  $360^{\circ}$ ). The following maps illustrate the representative dataset for a whole year for the surface pressure (Figure 44) and for the incoming radiative flux to surface (Figure 45).

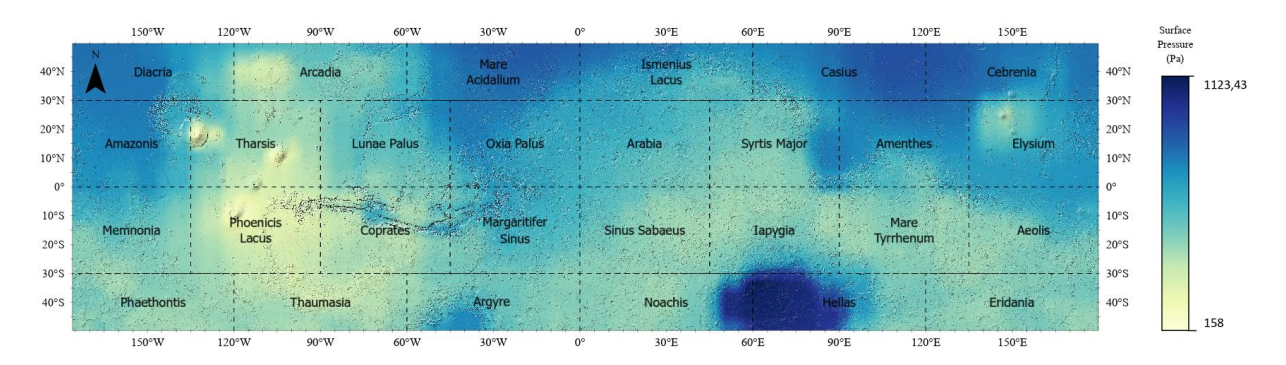


Figure 44 —Surface pressure layer representative of a standard Martian year.

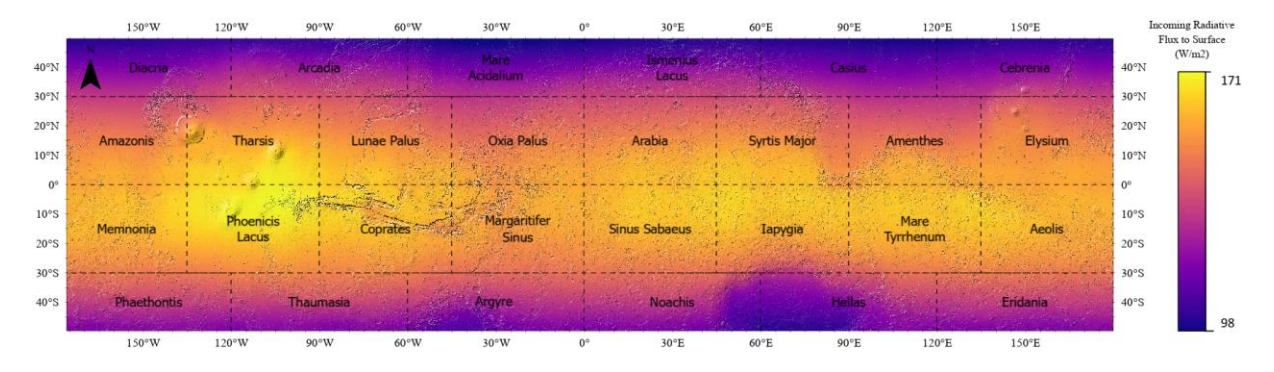


Figure 45 — Incoming radiative flux to surface layer representative of a standard Martian year.

## 3.2.2.2 COORDINATE SYSTEM ALIGNMENT

During data preparation, all spatial datasets were standardized by projecting them into the Mars 2000 Equidistant Cylindrical (Sphere) coordinate system (WKID 103885), which uses a spherical model of Mars with semimajor and semiminor axes of 3,396,190 meters. This projection was chosen for its ability to preserve distances along meridians and parallels, making it ideal for global analysis of Martian terrain. Using ArcGIS Pro version 3.4, the datasets were organized within file geodatabases to maintain integrity and streamline processing. This alignment ensured that spatial relationships and measurements were accurately represented, supporting reliable exploratory spatial data analysis and suitability modelling for robotic colonization and future human settlement on Mars.

## 3.2.3 ANALYSIS OF SEASONAL VARIABILITY

Averaging annual Martian surface temperature data simplifies the overall picture but may hide seasonal variations caused by Mars' axial tilt, orbital position, and eccentricity. To assess this limitation, standard deviation maps were generated for each seasonal variable over the entire Martian year (Figure 46 to 48).

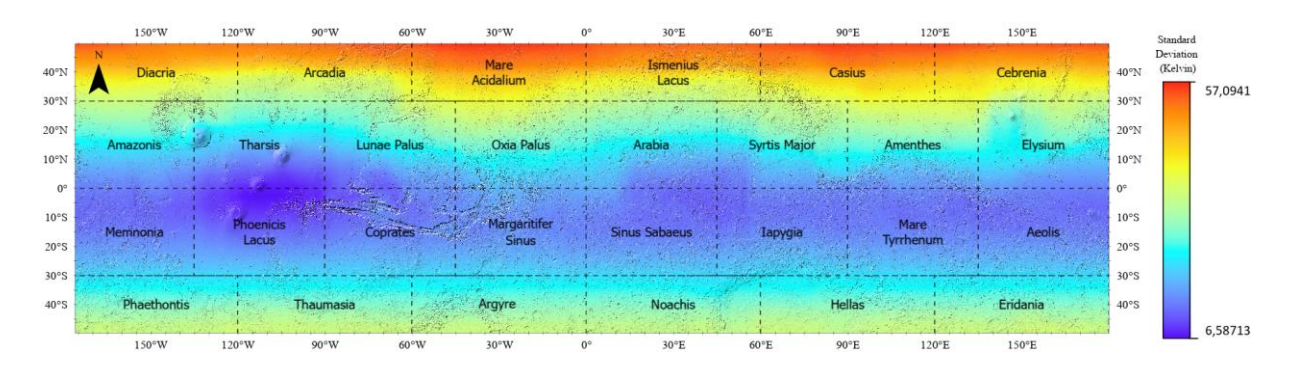


**Figure 46** — Standard Deviation map of the surface temperature dataset representative of a standard Martian year (solar longitude of  $0^{\circ}$  to  $360^{\circ}$ ).

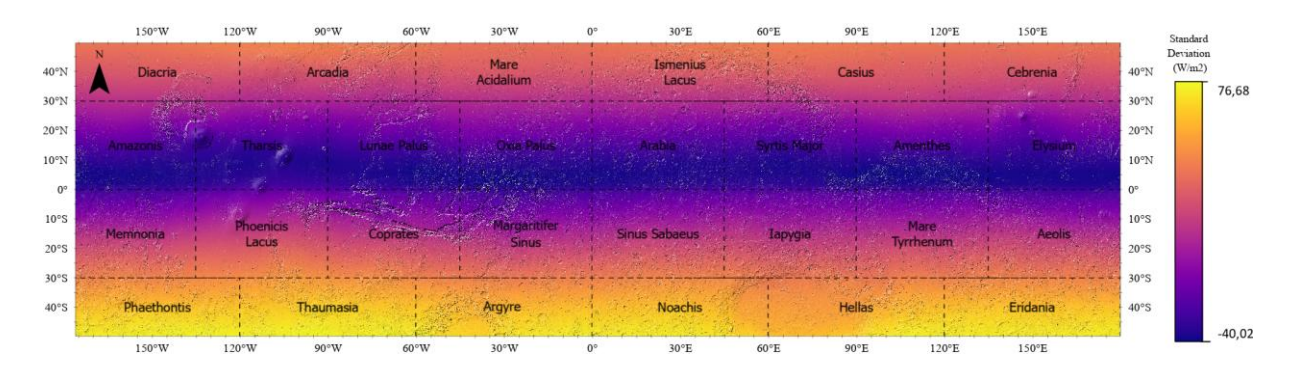


**Figure 47** — Standard Deviation map of the Incoming radiative flux to surface dataset representative of a standard Martian year (solar longitude of 0° to 360°).

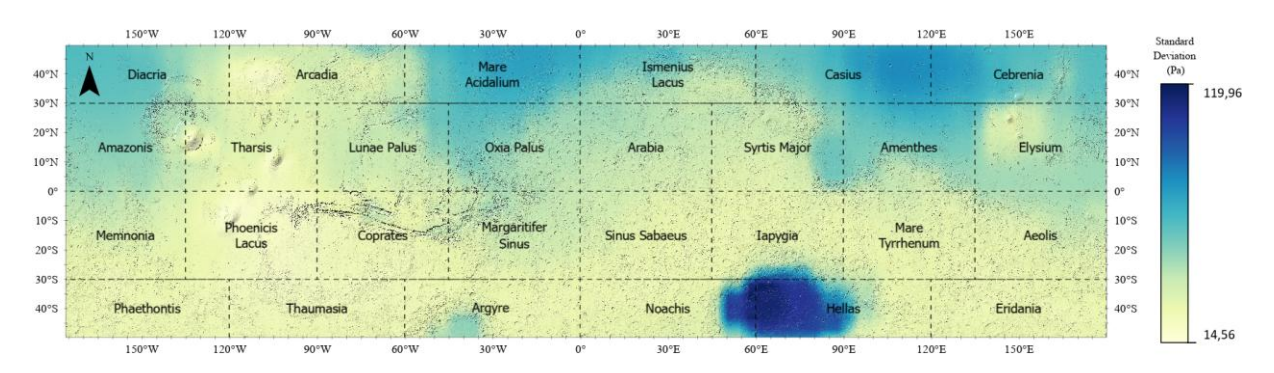


**Figure 48** — Standard Deviation map of the surface pressure dataset representative of a standard Martian year (solar longitude of  $0^{\circ}$  to  $360^{\circ}$ ).

The standard deviation measures seasonal variability across the 12 Martian months and provides insight into how conditions change throughout the year. This analysis identifies regions where seasonal fluctuations are most significant and where annual averages might obscure important temporal variations. By evaluating this variability, the study assesses the stability of key parameters in the equatorial region and determines whether averaging data over a Martian year simplifies the model without compromising accuracy.

The results reveal distinct spatial patterns in seasonal variability on Mars. The equatorial region exhibits the lowest standard deviation values, indicating stable conditions—especially in

surface temperature (Figure 46) and incoming radiative flux (Figure 47)—due to consistent solar insolation and milder seasonal extremes. In contrast, surface pressure at the equator shows no clear seasonal pattern (Figure 48). At higher latitudes, particularly near the poles, all parameters display greater variability driven by Mars' axial tilt and orbital eccentricity, resulting in pronounced temperature swings between the warmest and coldest months.

These findings confirm that in the equatorial region -30°N to 30°S approximately-, where seasonal variability is minimal, averaging data over a full Martian year effectively simplifies the model while maintaining temporal accuracy. However, at higher latitudes, where fluctuations are more pronounced, averaging may obscure key trends and reduce resolution.

## 3.2.4 DESCRIPTIVE STATISTICS & DATA VISUALIZATION

After preparing all datasets, including seasonal data, the next step was to visualize them and compute descriptive statistics to gain initial insights into their spatial and statistical properties.

## **3.2.4.1 ELEVATION**

The elevation dataset, derived from the Mars Orbiter Laser Altimeter (MOLA), provides a comprehensive representation of the Martian topography. Figure 49 illustrates the elevation map of Mars, covering the latitudinal range from 50°N to 50°S, which captures a wide variety of topographic features across the planet.

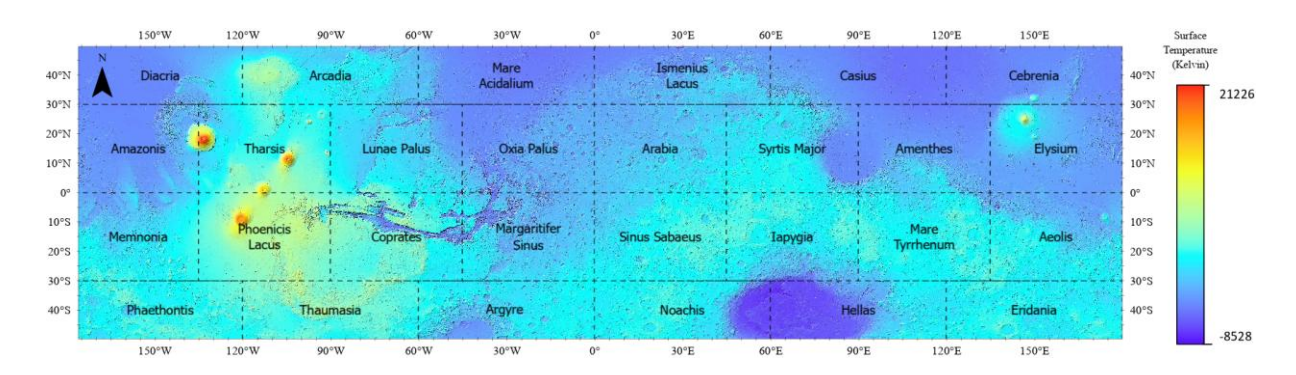


**Figure 49** — Elevation Map of Mars (50°N to 50°S). Elevation in meters; quadrangles represent standard geographic divisions of Mars.

Complementing the map, Figure 50 presents a histogram of elevation values, which reveals the frequency distribution of elevation within the 50°N to 50°S latitudinal range. The histogram highlights key characteristics of the Martian surface, such as its central tendency and variability.

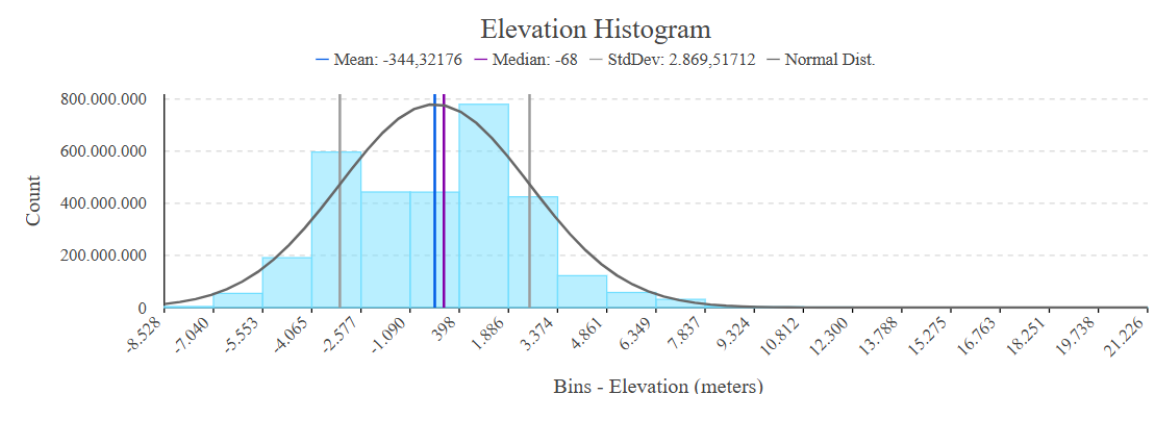


**Figure 50** — Elevation Histogram of Mars (50°N to 50°S).

The elevation histogram (Figure 50) reveals a bimodal distribution with a mean of -344.32 meters, a median of -68 meters, and a standard deviation of 2869.53 meters. This high variability reflects Mars' contrasting topography, where the low-lying northern plains differ markedly from the elevated southern highlands. The right tail of the distribution represents the highest elevations, including prominent volcanic features such as Olympus Mons, which reaches 22,226 meters.

## 3.2.4.2 WATER EQUIVALENT HYDROGEN (WEH)

The Water Equivalent Hydrogen (WEH) dataset, derived from neutron spectroscopy measurements by the Fine Resolution Epithermal Neutron Detector (FREND) aboard the ExoMars Trace Gas Orbiter (TGO), provides detailed insights into the distribution of hydrogen in the Martian subsurface. Figure 51 presents the WEH map of Mars, covering latitudes from 50°N to 50°S, highlighting regions with varying hydrogen concentrations.

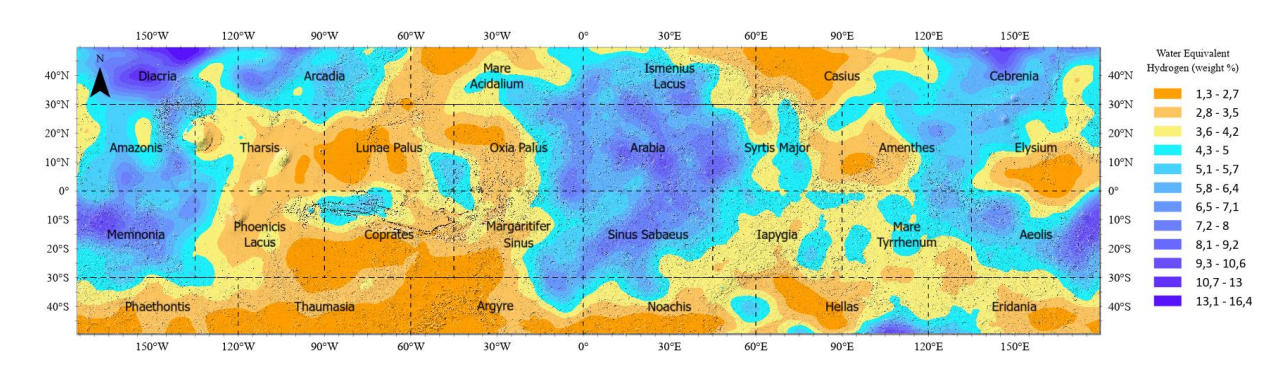


**Figure 51** —Water Equivalent Hydrogen Map of Mars (50°N to 50°S). Measured in percentage by weight, quadrangles represent standard geographic divisions of Mars. Data extracted from (Malakhov et al., 2022).

This dataset, obtained from Malakhov et al. (2022), reveals intricate spatial patterns of subsurface water content (Mean scenario), with some areas exhibiting unexpectedly high WEH

values—reaching up to 15 wt%—at moderate latitudes where free water and ice are typically unstable (Malakhov et al., 2022).

The histogram of Water Equivalent Hydrogen (Figure 52) values presents a right-skewed distribution, with a mean of 4.39 wt% and a standard deviation of 1.60 wt%, indicating moderate variability in the subsurface hydrogen content across the studied latitudinal range. The majority of WEH values cluster around the mean, with a gradual decrease in frequency toward higher values. However, a noticeable tail extends beyond 10 wt%, with some values reaching up to 15 wt%, suggesting localized anomalies.

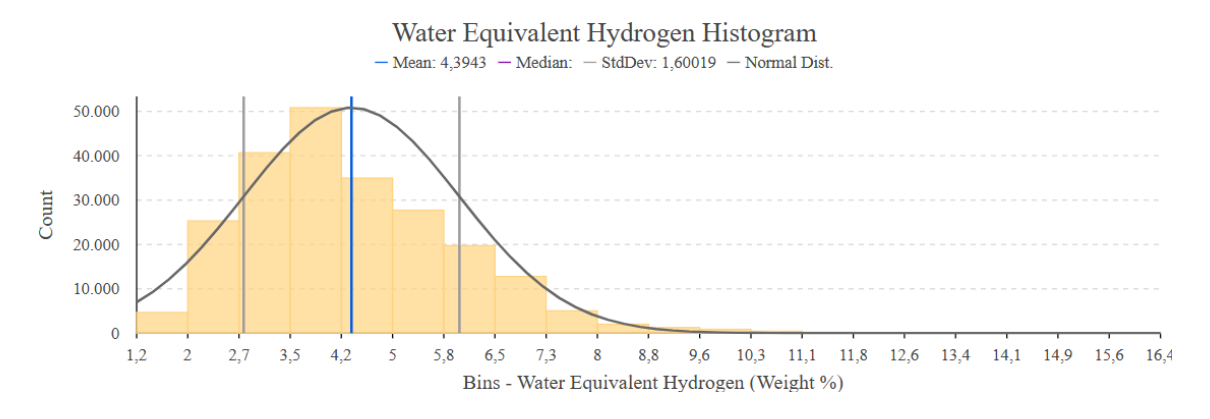


Figure 52 —Water Equivalent Hydrogen Histogram of Mars (50°N to 50°S).

This pattern aligns with the findings of Malakhov et al. (2022), where certain regions show unusually high WEH concentrations. Since hydrated minerals typically contain no more than 15 wt% water, these elevated values may indicate the presence of subsurface water ice rather than merely hydrogen in minerals. Such anomalies likely result from geological or climatic factors that enhance water retention. Furthermore, the histogram's right-skewed distribution suggests that, although high WEH values are rare, they could pinpoint key areas for future exploration and resource utilization on Mars (Malakhov et al., 2022).

## 3.2.4.3 THERMAL INERTIA

The Thermal Inertia dataset (Figure 53), derived from measurements by the Thermal Emission Spectrometer (TES) aboard the Mars Global Surveyor (MGS), provides critical insights into the physical properties of the Martian surface. Higher thermal inertia values indicate regions with dense, compacted materials such as bedrock, while lower values suggest loose, fine-grained materials like dust. Figure 53 presents the Thermal Inertia map of Mars, covering latitudes from 50°N to 50°S, highlighting variations in surface composition and thermal

response. The dataset, obtained from Putzig et al. (2005), serves as a key parameter in assessing the stability and suitability of potential landing and exploration sites.

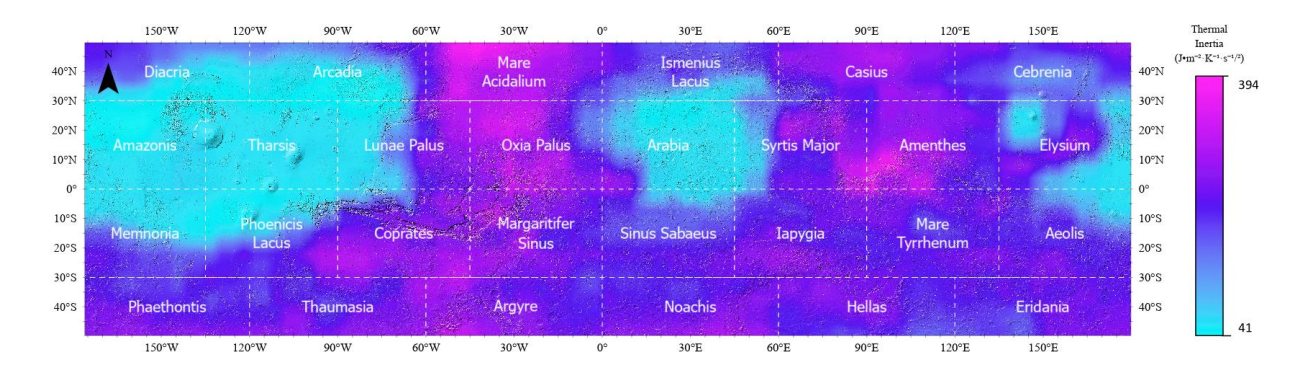


**Figure 53** —Thermal Inertia Map of Mars (50°N to 50°S). Measured in J·m<sup>-2</sup>·K<sup>-1</sup>·s<sup>-1/2</sup>; quadrangles represent standard geographic divisions of Mars. Data extracted from (Putzig et al., 2005).

The thermal inertia histogram (Figure 54) displays a broad spread in surface properties, with a mean of approximately  $189 \text{ J} \cdot \text{m}^{-2} \cdot \text{K}^{-1} \cdot \text{s}^{-1/2}$  and a standard deviation of  $83 \text{ J} \cdot \text{m}^{-2} \cdot \text{K}^{-1} \cdot \text{s}^{-1/2}$ . The median value of 214, which is higher than the mean, indicates a skewed distribution with a prominent peak around  $200 \text{ J} \cdot \text{m}^{-2} \cdot \text{K}^{-1} \cdot \text{s}^{-1/2}$  and a longer tail extending toward lower values.

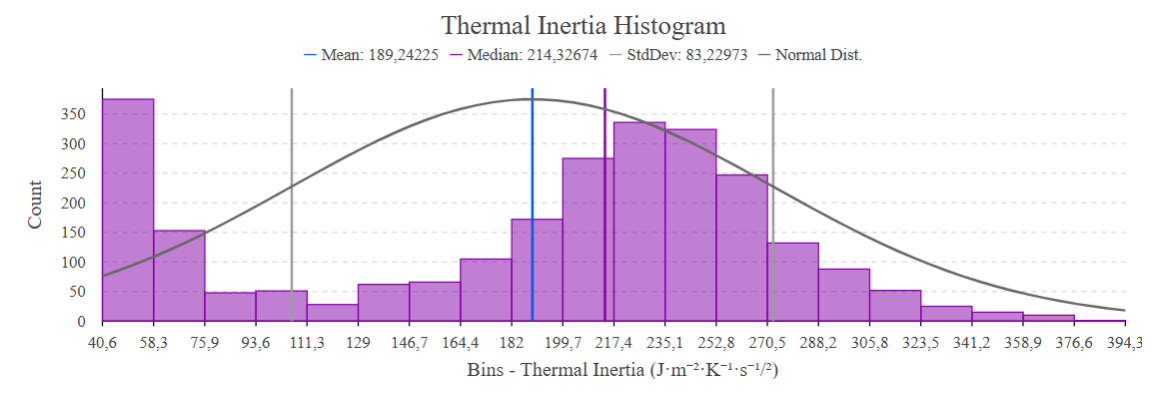


**Figure 54** —Thermal Inertia Histogram of Mars (50°N to 50°S).

The secondary peak at lower thermal inertia values indicates the presence of two distinct surface materials: fine-grained, unconsolidated dust or sand (with low thermal inertia) and more cohesive materials like duricrusts, bedrock, or indurated regolith (with higher thermal inertia). Frequent values below  $100~\rm J\cdot m^{-2}\cdot K^{-1}\cdot s^{-1/2}$  suggest extensive dust coverage, while the long tail toward higher values points to regions with exposed bedrock or compacted soils. These variations are crucial for understanding surface stability, heat retention, and energy balance, which are key factors in selecting sites for robotic exploration and future human missions.

## 3.2.4.4 ALBEDO

The Albedo dataset (Figure 55), derived from measurements by the Thermal Emission Spectrometer (TES) aboard the Mars Global Surveyor (MGS), provides essential information on the reflectivity of the Martian surface. Higher albedo values indicate bright, dust-covered regions, while lower values correspond to darker, rockier terrains with less surface dust. Figure 55 presents the Albedo map of Mars, covering latitudes from 50°N to 50°S, capturing spatial variations in surface reflectance. The dataset, obtained from Putzig and Mellon (2007), is crucial for understanding surface composition, thermal properties, and potential dust accumulation, all of which influence the selection of suitable landing and exploration sites.

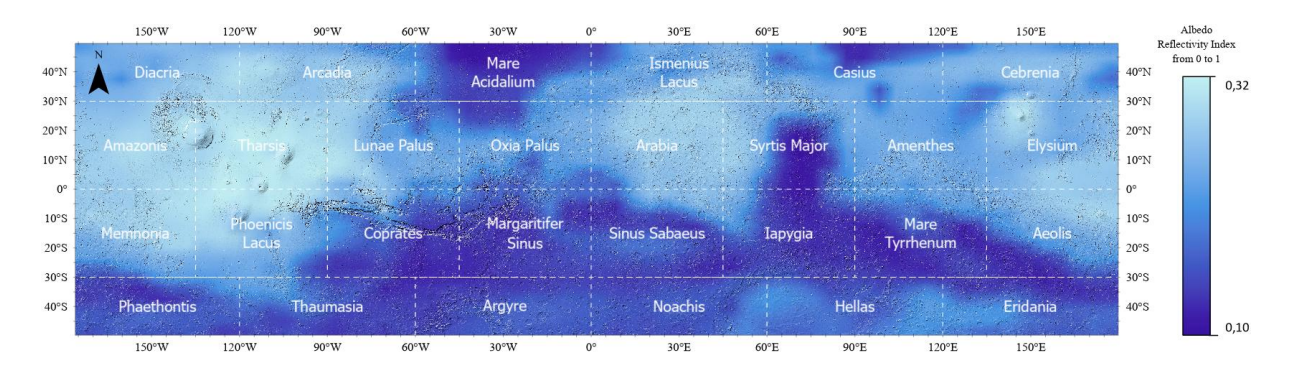


**Figure 55** —Albedo Map of Mars (50°N to 50°S). Ranges from 0 (full absorption) to 1 (full reflectivity); quadrangles represent standard geographic divisions of Mars. Data extracted from (Putzig & Mellon, 2007).

The histogram of Albedo values (Figure 56), derived from MGS TES data (Putzig & Mellon, 2007), exhibits a multimodal distribution, suggesting the presence of distinct surface types across latitudes 50°N to 50°S. The dataset has a mean albedo of 0.209 and a standard deviation of 0.057, indicating moderate variability in surface reflectivity.

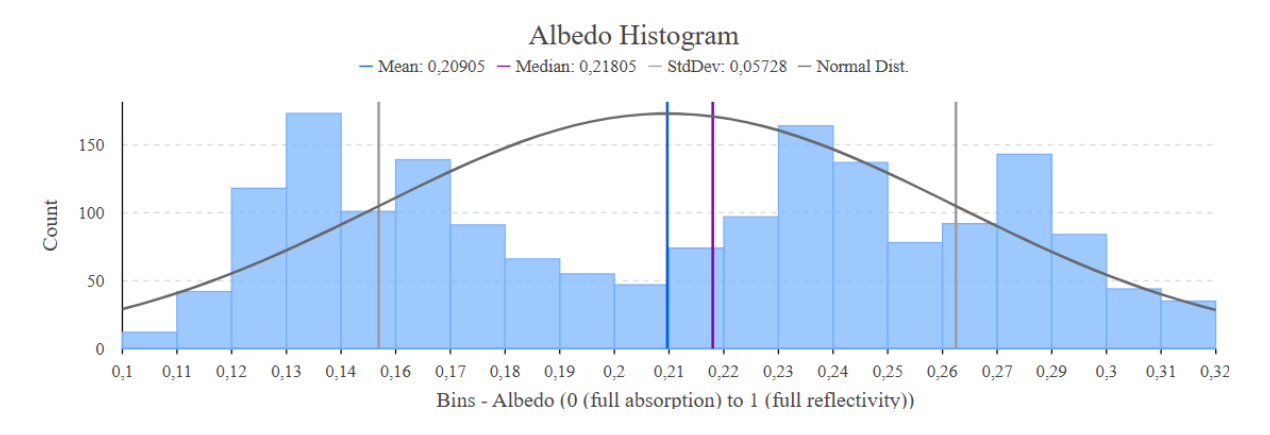


**Figure 56** —Albedo Histogram of Mars (50°N to 50°S).

## 3.2.4.5 SURFACE TEMPERATURE

The Surface Temperature dataset (Figure 57), derived from the Mars Climate Database General Circulation Model (GCM), represents the mean temperature of a martian year. Figure 55 presents the Surface Temperature map of Mars and highlights the planet's thermal variations. As one moves toward the poles, surface temperatures decrease, with colder regions found at higher latitudes. Seasonal impacts are less pronounced near the equator, where temperatures remain generally higher throughout the Martian year.

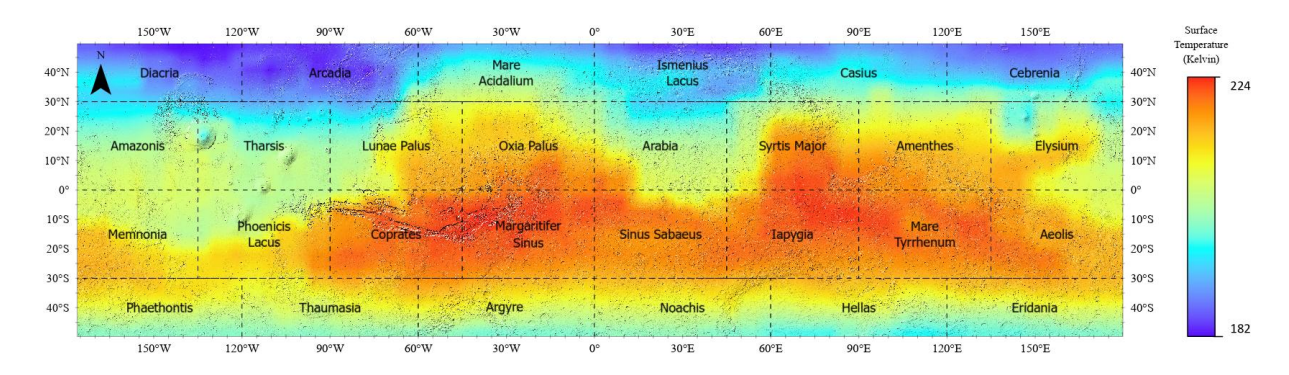


**Figure 57** —Surface Temperature Map of Mars (50°N to 50°S). Measured in Kelvin, quadrangles represent standard geographic divisions of Mars.

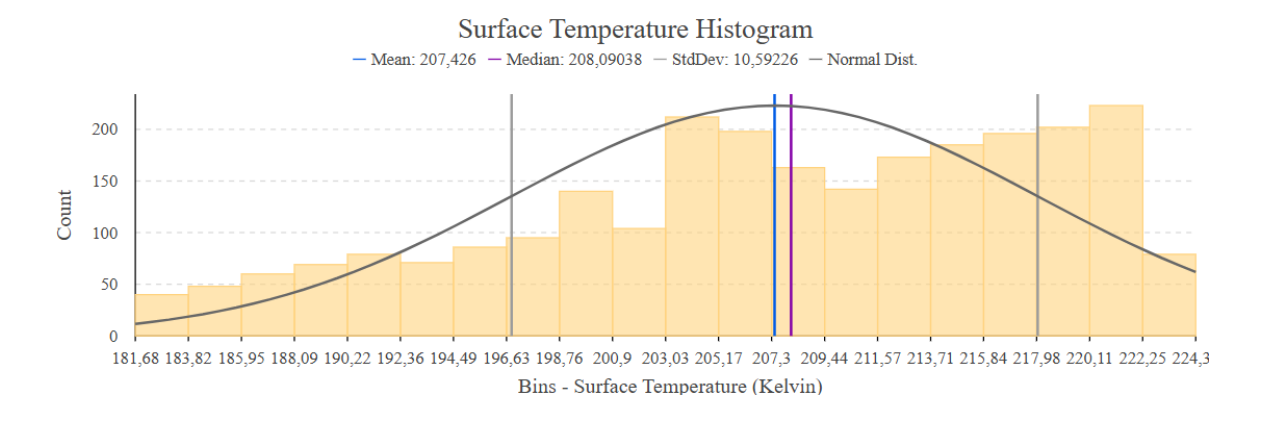


**Figure 58** —Surface Temperature Histogram of Mars (50°N to 50°S).

The histogram of surface temperature values (Figure 58) shows a negatively skewed distribution with a mean of 207.43 K and a standard deviation of 10.59 K, indicating moderate variability between 50°N and 50°S. Most values fall between 205–210 K, with a range from about 180 K to 225 K and a longer tail toward lower temperatures, suggesting that colder regions are less frequent. This thermal diversity reflects the influence of latitude, insolation, and surface material properties, with colder temperatures linked to high-latitude, low thermal inertia areas and warmer temperatures common in equatorial regions.

## 3.2.4.6 SURFACE PRESSURE

The Surface Pressure dataset (Figure 59), derived from the Mars Climate Database General Circulation Model (GCM), provides critical insights into the atmospheric conditions of Mars. Surface pressure is strongly influenced by topography, with higher values corresponding to low-lying regions and lower values occurring in elevated terrains.

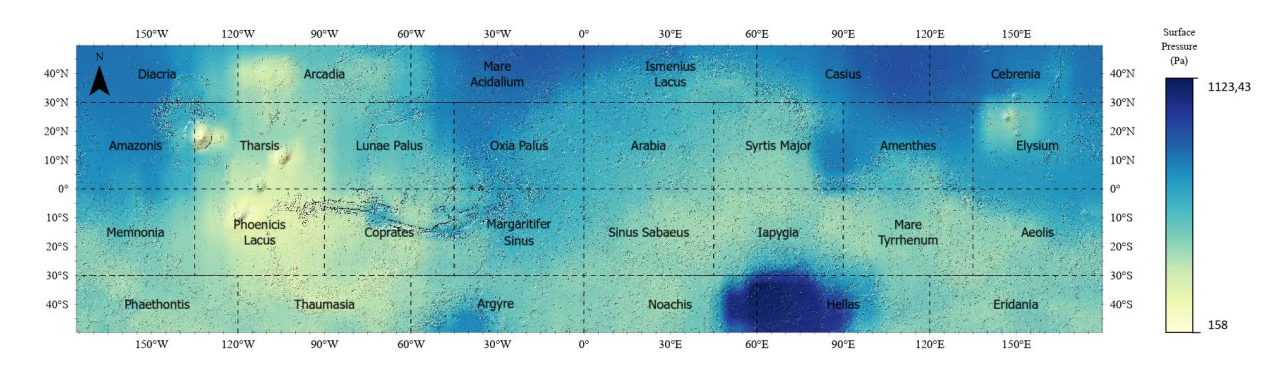


**Figure 59**—Surface Pressure Map of Mars (50°N to 50°S). Measured in Pascal, quadrangles represent standard geographic divisions of Mars.

Figure 59 presents the Surface Pressure map of Mars, covering latitudes from 50°N to 50°S, highlighting significant spatial variations. The highest surface pressures, exceeding 1000 Pa, are found in deep basins such as Hellas Planitia, while the lowest pressures, below 200 Pa, are observed over high-altitude regions like Tharsis and parts of Arabia Terra. This dataset is essential for understanding atmospheric dynamics and serves as a key parameter for mission planning.

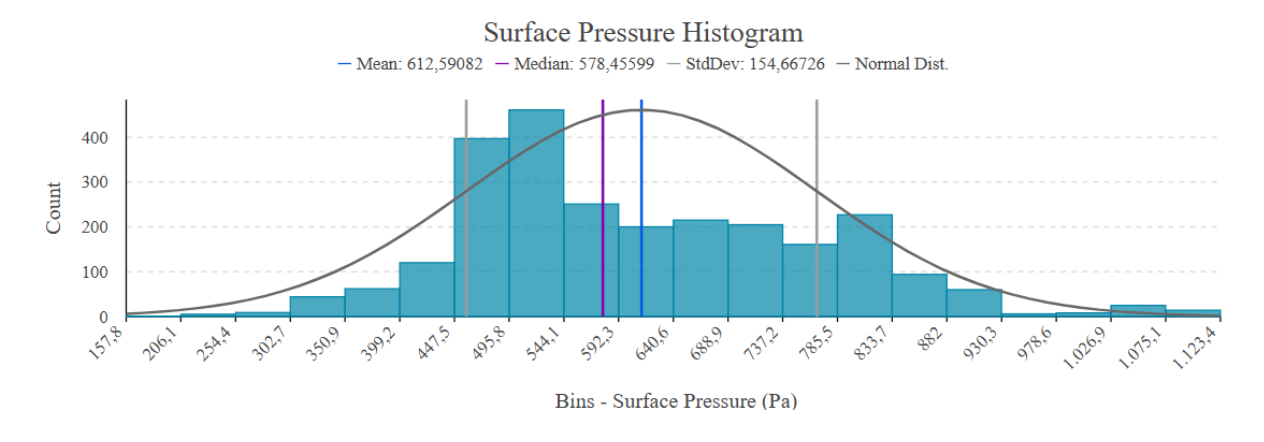


**Figure 60** —Surface Pressure Histogram of Mars (50°N to 50°S).

The histogram of surface pressure values (Figure 60) displays a right-skewed distribution with a mean of 612.59 Pa and a median of 578.46 Pa, indicating moderate variability across latitudes 50°N to 50°S. The values range from approximately 158 Pa to 1,123 Pa, reflecting the impact of topography on atmospheric pressure. Most values cluster between 500 and 700 Pa, with the

skewness suggesting that low-pressure regions—typically associated with high altitudes such as Tharsis and Arabia Terra—are more common, while higher pressure areas, like low-lying basins such as Hellas Planitia, are less frequent yet significant. This distribution reinforces the influence of Mars' surface elevation on its atmospheric pressure variations.

## 3.2.4.7 Incoming Radiative Flux to Surface

The Incoming Radiative Flux to Surface dataset (Figure 61), derived from the Mars Climate Database General Circulation Model (GCM), provides key insights into the distribution of solar energy reaching the Martian surface. Figure 61 presents the Incoming Radiative Flux map of Mars, covering latitudes from 50°N to 50°S, highlighting a strong latitudinal gradient.

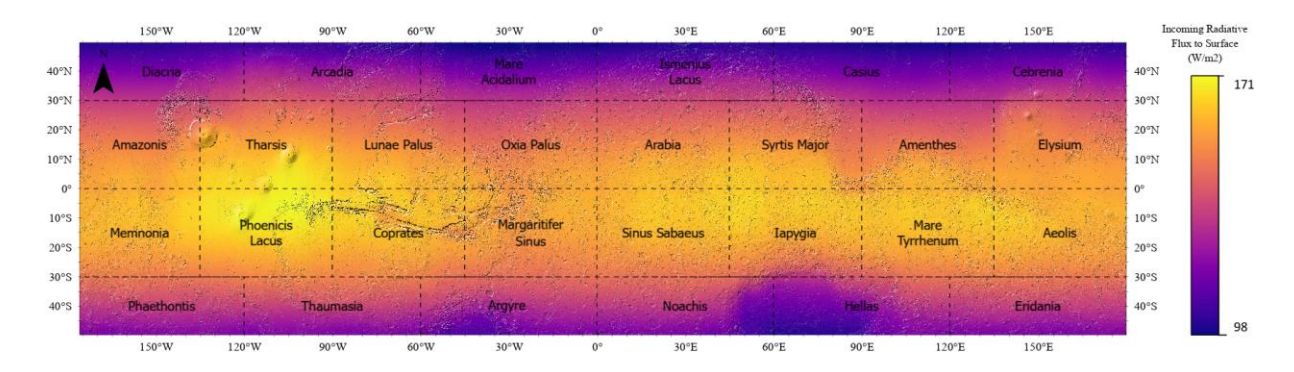


**Figure 61** — Incoming Radiative Flux to Surface Map of Mars (50°N to 50°S). Measured in W/m² (watts per square meter), quadrangles represent standard geographic divisions of Mars.

The highest flux values, exceeding 170 W/m², are concentrated in equatorial regions such as Sinus Sabaeus, Syrtis Major, and Mare Tyrrhenum, while the lowest values, below 100 W/m², are found toward higher latitudes, including Diacria, Cebrenia, and Phaethontis. These variations align with Mars' solar insolation cycle and atmospheric transparency, making radiative flux a crucial factor in energy balance studies and the design of solar-powered robotic missions.

The histogram of incoming radiative flux to the surface (Figure 62), derived from the Mars Climate Database General Circulation Model (GCM), exhibits a slightly right-skewed distribution, with a mean of 141.54 W/m² and a median of 146.04 W/m², indicating moderate variability across latitudes 50°N to 50°S.

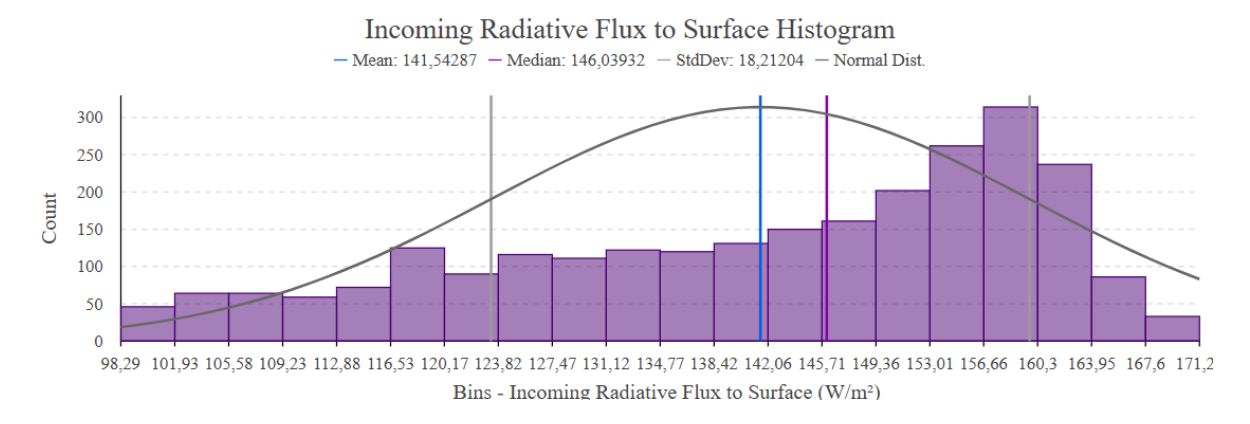


**Figure 62** — Incoming Radiative Flux to Surface Histogram of Mars (50°N to 50°S).

The dataset ranges from approximately 98 W/m² to 171 W/m², with most values between 120 and 160 W/m². This reflects Mars' latitudinal gradient in solar insolation, where higher radiative flux near the equator results in a slight skew toward elevated values, while lower flux at higher latitudes is less common. This pattern is consistent with the decrease in radiative flux due to lower solar incidence angles at higher latitudes.

## 3.2.5 SPATIAL CORRELATION ANALYSIS

This chapter's exploratory spatial data analysis assesses correlations among variables used in the human habitability suitability analysis (Table 7) to remove redundant, highly correlated factors. This refinement ensures that only independent, relevant factors are included, enhancing the efficiency and interpretability of the multi-criteria decision analysis while preserving scientific rigor. Notably, this correlation analysis from Table 9 applies solely to the human habitability methodology, as the engineering constraints framework follows a different approach that does not require such variable reduction.

Table 9—	Correlation	Matrix of	selected	variables	for human	habitability	suitability	analysis.
----------	-------------	-----------	----------	-----------	-----------	--------------	-------------	-----------

Layer	Surface Pressure	Elevation	Incoming Radiative Flux to Surface	Surface Temperature	Water Equivalent Hydrogen
Surface Pressure	1,00	-0,93	-0,49	-0,33	0,13
Elevation	-0,93	1,00	0,52	0,38	-0,13
Incoming Radiative Flux to Surface	-0,49	0,52	1,00	0,82	0,07
Surface Temperature	-0,33	0,38	0,82	1,00	-0,20
Water Equivalent Hydrogen	0,13	-0,13	0,07	-0,20	1,00

The correlation analysis (Table 9) reveals a strong negative correlation (-0.93) between surface pressure and altitude. This relationship is expected, as lower-altitude regions have denser air

columns and higher surface pressure, while higher-altitude areas, like Tharsis, experience reduced atmospheric mass and lower pressure. To avoid redundancy, surface pressure is removed from the model, and altitude is retained for its higher resolution and broader environmental influence. Similarly, incoming radiative flux shows a high correlation (0.82) with surface temperature; hence, it is also excluded, while surface temperature is maintained for its direct relevance to human habitability. These refinements ensure that the suitability model remains robust, efficient, and interpretable.

#### 3.3 DERIVED DATASETS: SLOPE & THERMOPHYSICAL UNITS

To enhance the analysis of human habitability and engineering constraints, two additional datasets were derived: slope and thermophysical units. These datasets offer critical insights into terrain stability and surface composition, which are essential for evaluating long-term operational feasibility on Mars.

The slope dataset (Figure 63), derived from the elevation (DEM) data, plays a key role in assessing the accessibility and safety of potential landing and settlement sites. Steeper slopes can hinder robotic navigation and infrastructure development, whereas flatter terrains generally favor stability and ease of construction.

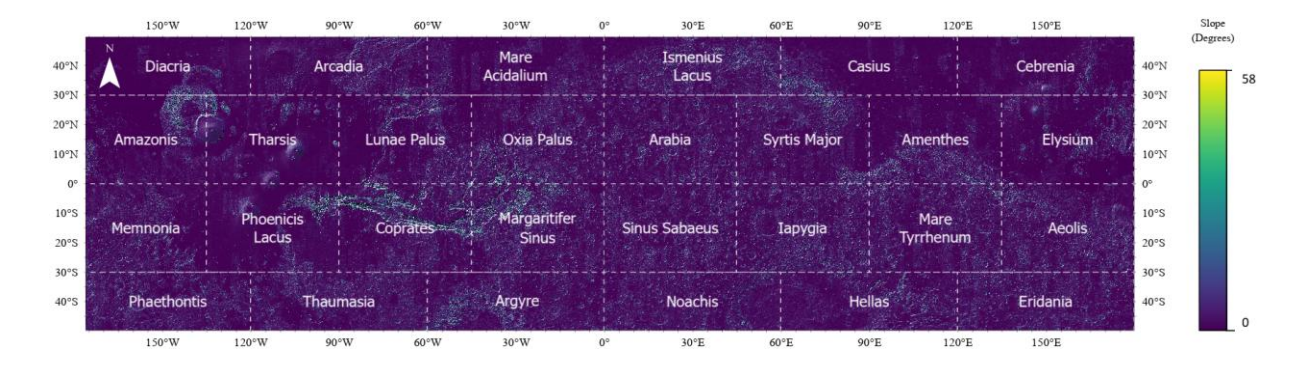


**Figure 63** —Slope Map of Mars (50°N to 50°S). measured in degrees (°) represents the angle of terrain inclination derived from the elevation dataset; quadrangles represent standard geographic divisions of Mars.

The slope map of Mars (Figure 63) reveals significant terrain steepness variations between 50°N and 50°S. High slopes concentrate in major geological features—such as Valles Marineris with its steep canyon walls, the Tharsis volcanic region (including Olympus Mons with its sharp elevation changes), and numerous impact craters with steep rims and ejecta patterns. In contrast, vast plains with low slopes suggest more favorable conditions for landing and surface operations. This dataset provides essential insights into terrain stability, navigability, and the feasibility of exploration activities.

The Thermophysical Units dataset (Figure 64) was created to identify whether Mars' load bearing and radar reflectivity surfaces are dominated by dust or other materials, a critical factor affecting mobility and structural support. Derived from thermal inertia and albedo datasets as intermediate layers, this dataset was produced using the methodology of Putzig et al. (2005), specifically following the approach detailed in section 2.4.2.5 on Thermophysical Properties: Dust and Load-Bearing Surface.

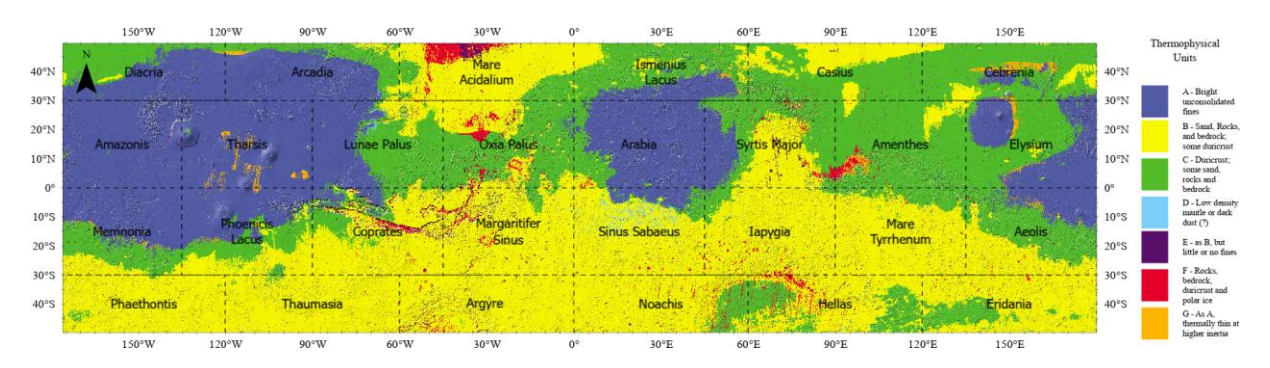


**Figure 64** —Thermophysical Unit Map of Mars (50°N to 50°S). Each unit is interpreted based on surface properties (Table 3); quadrangles represent standard geographic divisions of Mars.

By combining thermal inertia and albedo—key indicators of terrain composition and load-bearing capacity—the Martian surface was classified into distinct types, ranging from fine-grained dust deposits to exposed bedrock (Putzig et al., 2005). Using a two-dimensional histogram analysis, Putzig et al. (2005) identified seven thermophysical units (A–G), as outlined in Table 3, which distinguish between regions dominated by unconsolidated fines, duricrust, and rock-rich surfaces. This classification enhances our understanding of terrain suitability for exploration and settlement. Moreover, the reproduced thermophysical unit map closely aligns with the original findings (Figure 12 in Putzig et al., 2005), confirming a high degree of accuracy in capturing Mars' spatial distribution of thermophysical properties.

# 3.4 ENGINEERING CONSTRAINTS FOR SAFE LANDING AND ROBOTIC OPERABILITY

From the methodological framework, the next step is to develop engineering constraints layers for safe landing and robotic operability, following the parameters set for the Mars 2020 Perseverance mission from Table 10 (Grant et al., 2018) as also detailed in section 2.4.2 on Landing Site Engineering Constraints (Table 2). These constraints—based on elevation, slope, latitude, and thermophysical surface properties—delineate restricted zones to ensure that only suitable areas remain for further human habitability analysis. The following sections present

the individual restriction layers, followed by the final unified constraint map, which clearly distinguishes between restricted and non-restricted areas for subsequent analysis.

**Table 10** — Landing site engineering constraints and safety criteria used. Taken from the Mars 2020 Perseverance rover mission (Grant et al., 2018)

Engineering Parameter	Requirements	Rationale/Notes
Elevation	< -0.5 km	Sites at high elevations compromise safe landing at EDL sequence
Slope	$< 5^{\circ} (1 \text{ km scale})$	Sites with high slopes affect safe landing, control authority and energy consumption
Latitude	30°N to 30°S	Sites poleward of $30^\circ N$ and $30^\circ S$ have less stable thermal conditions and less consistent solar energy
Load Bearing Surface	Thermophysical Units A & B	Sites dominated by dust potentially have thick dust deposits, which affect the load bearing surface for Safe Landing, mobility and operability.
Radar Reflectivity	Thermophysical Units A & B	Sites dominated by dust have poor radar reflectivity, required for EDL sequence.

## 3.4.1 ALTITUDE-BASED ENGINEERING CONSTRAINT

The altitude constraint map (Figure 65) delineates restricted areas based on elevation thresholds for safe landing and robotic operability, following the Mars 2020 Perseverance mission criteria (Grant et al., 2018). Regions with elevations higher than -0.5km are restricted due to lower surface pressure, which can complicate atmospheric entry, descent, and landing. This restriction layer ensures that only low-elevation areas with favorable atmospheric conditions are considered for further analysis.

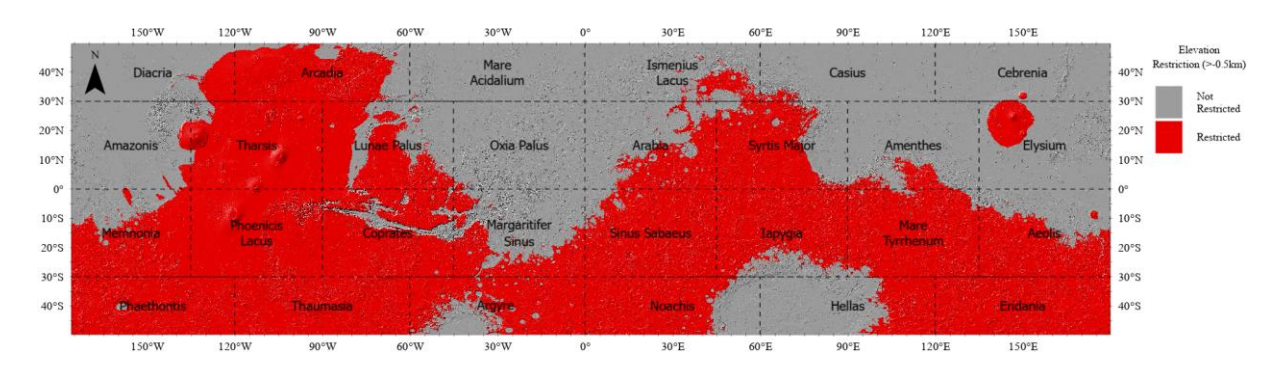


**Figure 65** — Altitude constraint map of Mars (50°N to 50°S). Areas above -500 meters are restricted (red), while non-restricted areas are shown in gray; quadrangles represent standard geographic divisions of Mars.

The Figure 65 map reveals an asymmetry between hemispheres: the southern hemisphere, characterized by higher elevations and heavy cratering, has significantly more restricted areas compared to the northern hemisphere's vast lowland plains. Additionally, volcanic features such

as Tharsis, Elysium, and other major constructs are entirely restricted, as expected given their high elevations.

## 3.4.2 SLOPE-BASED ENGINEERING CONSTRAINT

The slope-based engineering constraint (Figure 66) restricts areas where terrain slopes exceed 5° at a 1 km spatial scale (Table 10). This ensures that landing and operational zones are situated on relatively flat terrain, thereby reducing risks associated with instability, mobility challenges, and structural deployment. Steeper slopes can hinder entry, descent, and landing (EDL) by limiting control authority and increasing energy consumption, making these areas unsuitable for safe operations.

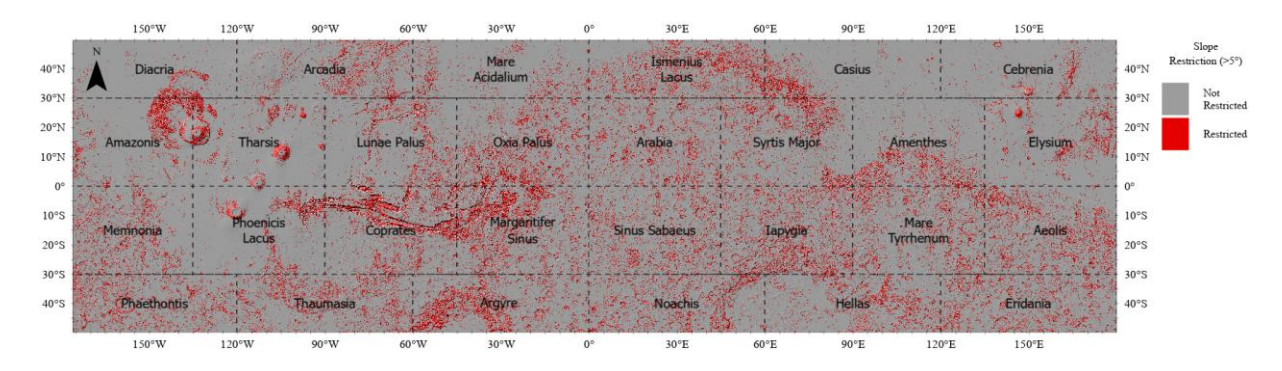


**Figure 66** — Slope constraint map of Mars (50°N to 50°S). Areas with slopes greater than 5° are restricted (red), while non-restricted areas are shown in gray; quadrangles represent standard geographic divisions of Mars.

The slope restriction layer identifies rough and geologically complex regions—including volcanic constructs, impact crater rims, and canyon systems like Valles Marineris—as restricted. In contrast, large lowland plains remain mostly unrestricted, reinforcing their suitability for safe landing and robotic operations.

## 3.4.3 LATITUDE-BASED ENGINEERING CONSTRAINT

The latitude-based constraint (Figure 67) restricts areas outside the 30°N to 30°S range (Table 11) to ensure optimal energy availability and thermal stability for robotic operations. This restriction aligns with Mars 2020 Perseverance mission parameters (Grant et al., 2018), favoring equatorial regions for their consistent solar energy intake and stable temperatures. Even missions using Radioisotope Thermoelectric Generators (RTGs) struggle to maintain stable temperatures, further underscoring the advantage of operating in equatorial regions (Golombek et al., 2012).

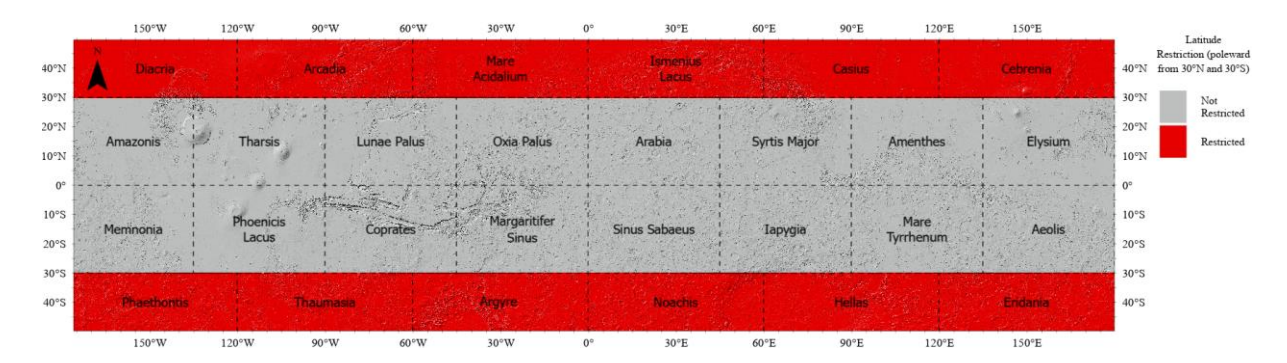


**Figure 67**— Latitude constraint map of Mars (50°N to 50°S). Areas beyond 30°N and 30°S are restricted (red), while non-restricted areas are shown in gray; quadrangles represent standard geographic divisions of Mars.

The latitude restriction layer excludes higher-latitude terrains, particularly in the northern and southern mid-latitudes, where thermal variability and seasonal effects are more extreme. As shown in Figure 65, areas beyond 30°N and 30°S are restricted (red) due to colder temperatures, limited solar energy, and higher energy demands for thermal regulation. In contrast, regions within the 30°N–30°S range remain unrestricted (gray), emphasizing their suitability for long-term energy efficiency and stable conditions—both crucial for safe landing and robotic operations.

# 3.4.4 LOAD BEARING SURFACE AND RADAR REFLECTIVITY-BASED ENGINEERING CONSTRAINT

The load-bearing surface and radar reflectivity constraint (Figure 68) defines restricted areas based on thermophysical units (Table 10), which classify the Martian surface according to thermal inertia and albedo properties.

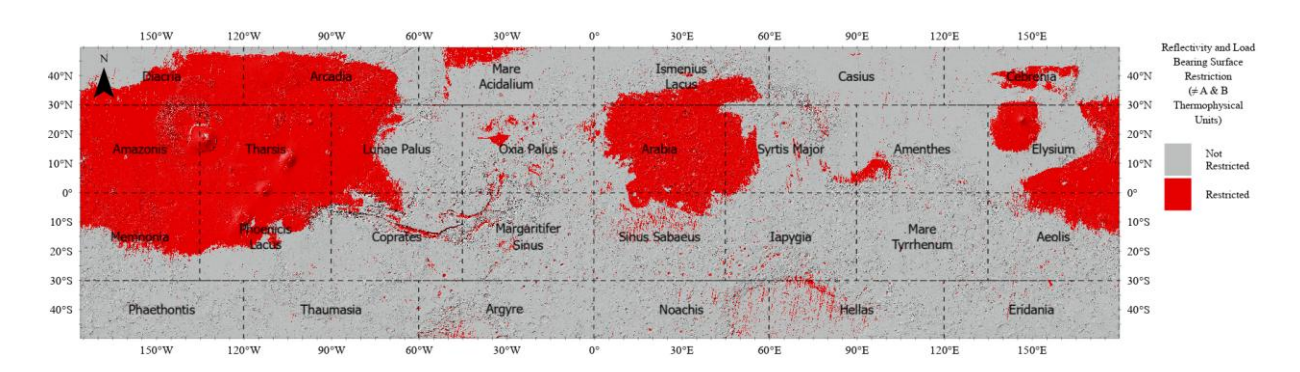


**Figure 68** — Load-bearing surface and radar reflectivity constraint map of Mars (50°N to 50°S). Areas dominated by unconsolidated fines or unstable surfaces (units other than B and C) are restricted (red), while stable surfaces remain non-restricted (gray); quadrangles represent standard geographic divisions of Mars.

Following the Mars 2020 Perseverance mission parameters (Grant et al., 2018), only thermophysical units B and C are considered non-restricted, as they represent duricrust, rocks,

and bedrock—stable surfaces suitable for safe landing and rover mobility. In contrast, units dominated by fine-grained, unconsolidated dust (e.g., Unit A) are restricted, as these surfaces present poor load-bearing capacity and low radar reflectivity, which can compromise landing success and long-term operability.

The restricted areas (Figure 68) correspond to dust-dominated regions where thick unconsolidated deposits compromise terrain stability and radar reflectivity. Conversely, rockier terrains and regions stabilized by duricrust remain non-restricted, highlighting their suitability for safe landing and long-term robotic operations.

## 3.4.5 Unified Engineering Constraints Map

To establish a comprehensive constraint layer, the previously defined engineering constraints—altitude, slope, latitude, and load-bearing surface/radar reflectivity—are merged into a unified map (Figure 69). This integration ensures that only areas meeting all safety and operability requirements remain available for further analysis. By combining these layers, regions failing to meet criteria for elevation, terrain stability, thermal conditions, and energy availability are excluded, resulting in a refined selection of potential landing and operational zones. The final unified constraint map (Figure 69) delineates restricted and non-restricted areas and serves as the foundation for subsequent human habitability suitability analysis.

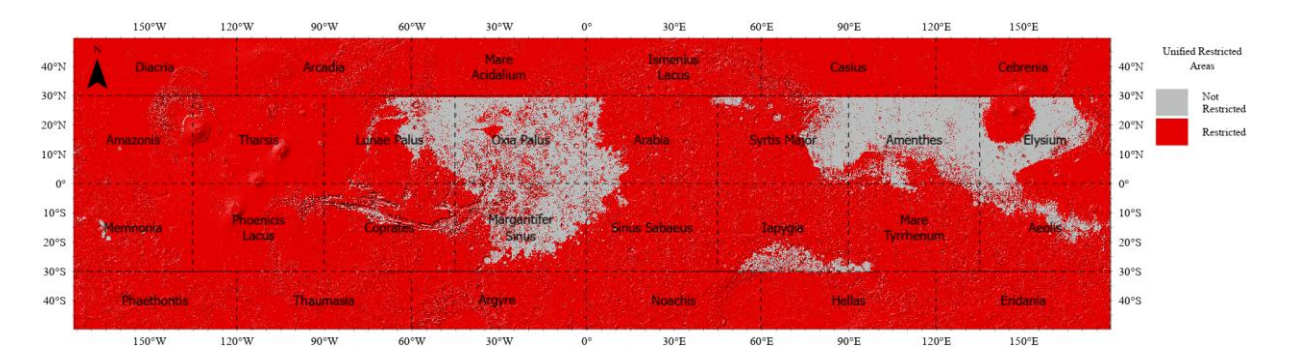


**Figure 69** — Unified engineering constraints map of Mars (50°N to 50°S). Areas that fail to meet one or more engineering constraints (altitude, slope, latitude, or load-bearing surface/radar reflectivity) are restricted (red), while regions that satisfy all constraints remain non-restricted (gray); quadrangles represent standard geographic divisions of Mars.

To provide a clearer visualization of the safe landing and robotic operability zones, the unified constraints map is presented with an alternative symbology (Figure 70). In this version, non-restricted areas—which meet all engineering constraints—are highlighted in green, emphasizing their suitability for landing and operations, while restricted areas remain in gray. This visualization helps to identify the regions available for further human habitability analysis.

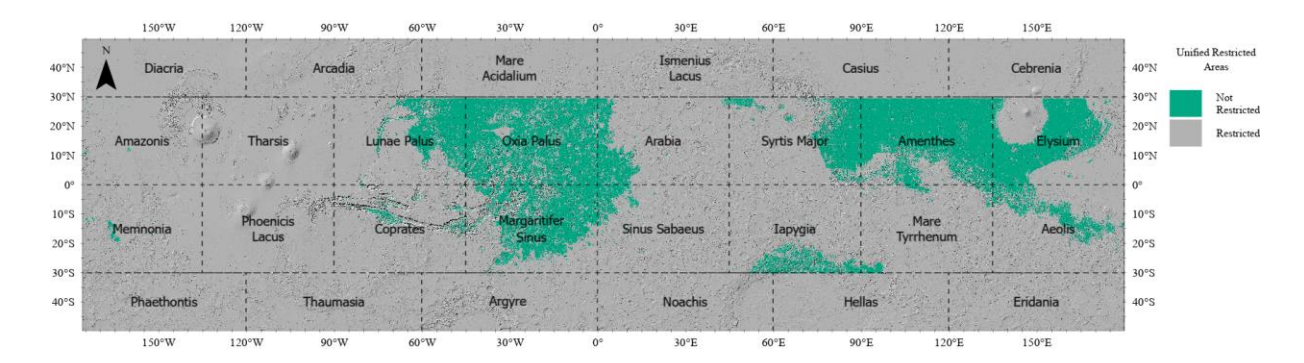


**Figure 70**— Alternative symbology for the unified engineering constraints map of Mars (50°N to 50°S). Safe landing and robotic operability zones are highlighted in green, while restricted areas remain in gray; quadrangles represent standard geographic divisions of Mars.

# 3.5 MULTI-CRITERIA HUMAN HABITABILITY ASSESSMENT USING ANALYTIC HIERARCHY PROCESS (AHP)

To complement the engineering constraint analysis, a MCDA model was developed to identify the most suitable regions for future human settlement. This analysis uses the Analytic Hierarchy Process (AHP), a structured decision-making method that weights and combines multiple geospatial factors based on their relative importance (Saaty, 2009). Based on the prior correlation analysis (Table 9), surface pressure and incoming radiative flux were removed from the model to avoid redundancy, ensuring a more robust and independent evaluation of habitability conditions. Before the analysis, it is important to review the criteria which made part of the model and their relevance and rationale for this purpose (Table 11).

Table 11 — Criteria included in AHP method for suitability analysis of Human Habitability

Human Habitability Criteria	Preferability Human Habitability	Rationale/Notes
Elevation	Low Values	Higher atmospheric pressure, improved water stability; reduced radiation exposure
Slope	Low Values	Safer landing, stable habitat/infraestructure construction, easier mobility
Water Equivalent Hydrogen	High Values	Essential for life support, agriculture, and fuel production, enables in-situ resource utilization
Surface Temperature	High Values	Lower energy requirements, improved thermal regulation

By integrating elevation, water equivalent hydrogen, slope, and surface temperature (Figure 11), this approach systematically and objectively evaluates habitability potential. The pairwise comparison model was recalculated from that proposed by Zhu et al. (2025) for aboveground habitat site selection on Mars using expert decision-making, with modifications to better align

with this study's objectives. This recalculation involved removing the dust variable from the original model.

Unlike Zhu et al. (2025), this study employs water equivalent hydrogen data from Malakhov et al. (2022) instead of the SWIM dataset (Morgan et al., 2021; Putzig et al., 2023). The Malakhov et al. (2022) dataset was chosen because, despite its less direct correlation with actual water ice, it provides continuous coverage across the entire study area. In contrast, the SWIM dataset has zones with inconclusive or missing data, particularly in regions where the altitude exceeds +1 km—a significant portion of the study area.

The Table 12 displays the matrix tables derived from the AHP evaluation. These tables illustrate the pairwise comparisons between factors, denoted as aij, which represent the extent to which factor i is considered more or less significant than factor j (Zhu et al., 2025). The values of aij are determined using Equation (1).

$$a_{ij} = \frac{importance_i}{importance_j} \tag{1}$$

Table 12 — AHP Pairwise Comparison Matrix

Criteria	Slope	Surface Temperature	Water Equivalent Hydrogen	Elevation
Slope	1	1/4	1/5	1/3
Surface Temperature	4	1	1/2	2
Water Equivalent Hydrogen	5	2	1	3
Elevation	3	1/2	1/3	1

Subsequently, the weights for each criterion were determined by calculating the average of each row in the normalized matrix (Table 13).

Table 13 — Normalized AHP Matrix with Criterion Weights

Criteria	Slope	Temperature	Water	Elevation	Weight
Slope	0,08	0,07	0,10	0,05	0,074
Surface Temperature	0,31	0,27	0,25	0,32	0,284
Water Equivalent Hydrogen	0,38	0,53	0,49	0,47	0,471
Elevation	0,23	0,13	0,16	0,16	0,171

After obtaining the criterion weights, the next step involved computing the weighted sum vector by multiplying the original pairwise comparison matrix by the weight vector. This operation produces a new matrix (Table 14) where each criterion's value reflects its weighted influence across all comparisons. Subsequently, each element of the weighted sum vector was divided by its corresponding weight to derive the consistency vector.

Table 14 — Weighted Sum Matrix for Consistency Calculation in AHP

Criteria	Slope	Temperature	Water Equivalent Hydrogen	Elevation	Weighted Sum Vector	Consistency Vector
Slope	0,074	0,071	0,094	0,057	0,296	4,019002308
Surface Temperature	0,295	0,284	0,235	0,343	1,157	4,073728447
Water Equivalent Hydrogen	0,368	0,568	0,471	0,514	1,922	4,080967237
Elevation	0,221	0,142	0,157	0,171	0,691	4,031763899

To evaluate the consistency of the AHP pairwise comparison matrix, Lambda Max ( $\lambda_{max}$ ) was computed, as shown in Table 15. Using Equation (2), the Consistency Index (CI) was then derived as follows:

$$CI = \frac{\lambda_{max} - n}{n - 1} \tag{2}$$

Where n represents the number of criteria; n = 4.

Subsequently, the Consistency Ratio (CR) was determined using Equation (3):

$$CR = \frac{CI}{RI} \tag{3}$$

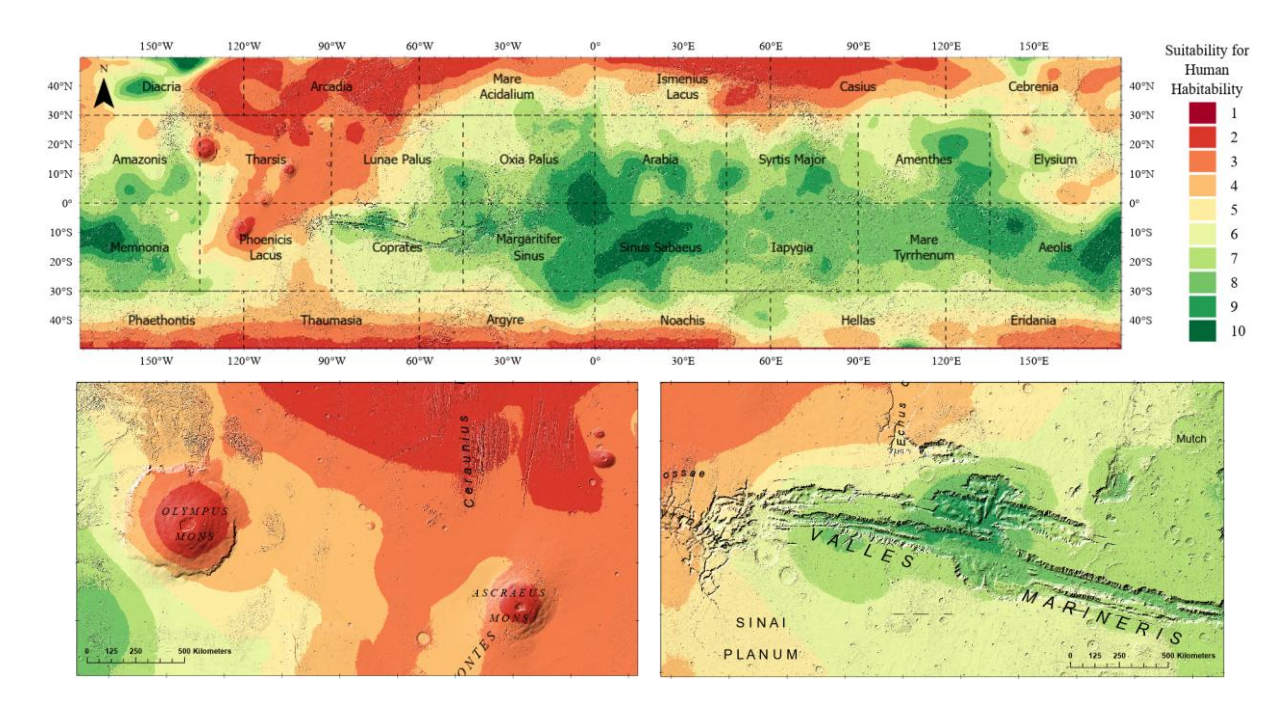
Where RI corresponds to the Random Index value based on Saaty's reference table (Saaty, 2009). The CR value obtained (Table 15) was significantly below the threshold of 0.10, indicating that pairwise comparisons were logically consistent and suitable for further analysis.

Table 15 — Consistency Analysis Results for AHP Matrix

Eigenvalue	Consistency	Random Index (RI)	Consistency	
Lambda Max	Index (CI)	(based on Saaty's table)	Ratio (CR)	
4,051365473	0,0171	0,9	0,0190	

The results in Table 15 confirm that the Consistency Ratio (CR) is 0.0190, which is well below the acceptable threshold of 0.10. This indicates that the pairwise comparison matrix exhibits a high level of consistency, ensuring that the assigned weights are reliable and do not contain significant logical inconsistencies. Consequently, the computed weights can be confidently applied in the multi-criteria human habitability assessment without the need for further adjustments.

Figure 71 illustrates the final results of the human habitability suitability analysis using the weights from the AHP method above, highlighting the most and least favorable regions for potential settlement. Two additional map views are displayed from significant Mars features, which showcase distinctive topography and geology, emblematic of Mars.



**Figure 71**— Human Habitability Suitability Map of Mars (50°N to 50°S). Suitability values classified by natural breaks, from 1 (least suitable) to 10 (most suitable). Additional map views highlight key geological features—Olympus Mons & Ascraeus Mons (Bottom-Left); and the Valles Marineris zone (Bottom-Right).

From the results depicted in the final map of Figure 71 it is evident that mid-latitude regions around the Martian equator generally exhibit higher habitability scores (green areas) —except on areas with volcanic features—, while higher latitudes and southern highlands show lower suitability (red areas). These variations reflect the combined influence of temperature, terrain stability, and resource availability, suggesting that —based on the model— the more central latitudes may offer the most favorable conditions for human settlement.

# 3.5.1 SENSITIVITY ANALYSIS

A sensitivity analysis was conducted to evaluate the impact of weight variations on the final suitability results and assess the model's robustness. This process ensures that the final suitability map (Figure 71) is not overly dependent on specific weight assignments, thereby enhancing the reliability of the results.

Several alternative weighting scenarios were tested to examine the model's response to different weighting configurations. These variations include adjustments to individual criteria weights, randomized perturbations, and structural modifications to the weighting hierarchy. The details of these sensitivity models, including the assigned weights, are presented in Table 16.

**Table 16** — Criteria Weights of Suitability Models created for sensitivity analysis

Suitability Model	Slope	WEH	Elevation	Temperature	Description
Baseline Model (AHP)	0.074	0.471	0.171	0.284	Reference model using original weights.
Equal Weights	0.25	0.25	0.25	0.25	All criteria have the same weight to test weight influence.
High-Impact (+20%)	0.067	0.517	0.156	0.26	Increases the most influential criterion (WEH) by 20% to test sensitivity.
High-Impact (-20%)	0.081	0.416	0.189	0.314	Decreases the most influential criterion (WEH) by 20% to test sensitivity.
Random Perturbation	0.080	0.447	0.187	0.286	Introduces small random weight variations (+/-10%) to assess overall stability.
Inverted Priority	0.471	0.074	0.171	0.284	Swaps the highest and lowest weighted criteria to evaluate extreme changes.

Statistical and spatial analyses were conducted — using the above suitability models, to quantify variations, assess model robustness, and identify the most influential criteria, providing insight into the stability, reliability, and sensitivity of the suitability assessment.

# 3.5.1.1 PEARSON'S CORRELATION ANALYSIS

Pearson's correlation (Table 17) was used to assess the numerical similarity between the suitability models, measuring how weight variations influenced the overall suitability values. High correlation coefficients indicate that the models produce similar results despite changes in weighting, whereas lower values suggest greater sensitivity to specific weight modifications.

**Table 17** — Pearson's Correlation Sensitivity Analysis of suitability models

Suitability Model	Baseline (AHP)	Equal Weights	High-Impact (+20%)	High-Impact (-20%)	Random Perturbation	Inverted Priority
Baseline (AHP)	1,000	0,943	0,994	0,995	0,999	0,824
<b>Equal Weights</b>	0,943	1,000	0,959	0,920	0,953	0,946
High-Impact (+20%)	0,994	0,959	1,000	0,978	0,996	0,868
High-Impact (-20%)	0,995	0,920	0,978	1,000	0,992	0,777
Random Perturbation	0,999	0,953	0,996	0,992	1,000	0,840
Inverted Priority	0,824	0,946	0,868	0,777	0,840	1,000

The results show that most models exhibit high correlation with the baseline (r > 0.94), suggesting that small to moderate weight adjustments have minimal impact on overall suitability distribution. The Random Perturbation Model produced an almost identical output to the baseline (r = 0.999), confirming that minor weight fluctuations do not significantly alter results. Similarly, the High-Impact Variation Models ( $\pm 20\%$  Water Weight) remained strongly correlated (r > 0.99), indicating low sensitivity to moderate adjustments in the most influential criterion.

The Equal Weights Model showed moderate deviations (r = 0.943 with the baseline), reinforcing the role of weighted prioritization in suitability outcomes. In contrast, the Inverted Priority Model had the lowest correlation values (r = 0.777-0.946) across comparisons, indicating that extreme shifts in weighting priorities lead to significant changes in suitability scores.

Overall, the Pearson's correlation analysis suggests that the model is highly stable under minor weight changes but more sensitive to extreme variations in weighting structure

# 3.5.1.2 SPEARMAN'S RANK CORRELATION ANALYSIS

While Pearson's correlation measures numerical similarity between models, it does not account for potential changes in the ranking of suitability values. To address this, Spearman's rank correlation (Equation 4) was applied to evaluate whether the relative suitability order of locations remains consistent across different weighting scenarios.

$$\rho = 1 - \frac{6\sum d_i^2}{n(n^2 - 1)} \tag{4}$$

Where  $d_i$  is the difference between the ranks of each pair of observations and n the total number of ranked observations.

Table 18 — Spearman's Rank Correlation Between Baseline and Sensitivity Models

Comparison	Spearman's $ ho$	Interpretation	
Baseline vs. Baseline	1.000	Reference model	
Baseline vs. Equal Weights	0.920	Moderate ranking shifts, sensitivity to equal weighting	
Baseline vs. High-Impact (+20%)	0.990	Very stable, minimal ranking changes	
Baseline vs. High-Impact (-20%)	0.993	Very stable, minimal ranking changes	
Baseline vs. Random Perturbation	0.999	Almost identical rankings, low sensitivity	
Baseline vs. Inverted Priority	0.303	Highly sensitive, extreme ranking changes	

Following the results presented in Table 18, the Spearman's rank correlation analysis confirms that the model remains highly stable under small to moderate weight variations, as indicated by the strong correlation values ( $\rho > 0.9$ ) for most sensitivity scenarios. The Random Perturbation Model ( $\rho = 0.999$ ) and the High-Impact Variation Models ( $\rho > 0.99$ ) show minimal ranking changes, demonstrating the model's robustness to minor adjustments.

However, the Equal Weights Model ( $\rho$  = 0.920) exhibits moderate deviations, suggesting that removing weighted prioritization introduces some variability in ranking but does not significantly alter the suitability distribution. In contrast, the Inverted Priority Model ( $\rho$  = 0.303) displays the lowest correlation, indicating substantial ranking shifts when weight priorities are reversed. This result highlights the sensitivity of the suitability model to extreme changes in the weighting structure, reinforcing the importance of well-calibrated weights in the multi-criteria decision-making process.

### 3.5.1.3 SUITABILITY SCORE 10 OVERLAP ANALYSIS

To assess the spatial consistency of the highest-suitability areas across different weighting scenarios, a Suitability Score 10 Overlap Analysis was conducted. Rather than selecting a fixed percentage of top-ranking pixels, this approach identifies areas classified as Score 10, based on natural breaks in the Baseline Model, and evaluates their stability across sensitivity models. By maintaining a consistent classification threshold, this ensures that observed variations in high-suitability areas are solely due to weight adjustments rather than differences in classification methods. The overlap percentage provides insight into the model's robustness and the influence of specific criteria on suitability distribution.

Table 19 — Suitability Score 10 Overlap Between Baseline and Sensitivity Models

Comparison	Overlapp % of Score 10	Baseline Pixels Score 10
Baseline vs. Equal Weights	98.90%	Very stable, minimal impact from equalizing weights.
Baseline vs. High-Impact (+20%)	98.20%	Very stable, small weight adjustments have little effect.
Baseline vs. High-Impact (-20%)	48.15%	Major shift, reducing weight significantly alters top locations.
Baseline vs. Random Perturbation	99.67%	Almost identical, random weight variations have negligible impact.
Baseline vs. Inverted Priority	94.73%	Moderate shift, reversing weights affects top 10% locations.

The Suitability Score 10 Overlap Analysis (Table 19) confirms that the model remains highly stable under small and moderate weight variations, as shown by the high overlap percentages (>98%) for the Equal Weights, High-Impact (+20%), and Random Perturbation Models. This suggests that minor weight modifications do not significantly impact the distribution of the highest-suitability locations, reinforcing the model's structural reliability.

In contrast, the High-Impact (-20%) Model shows a sharp decline in overlap (48.15%), demonstrating that reducing the weight of Water substantially alters the highest-suitability areas. Similarly, the Inverted Priority Model (94.73%) causes moderate shifts, indicating that reversing weight priorities affects suitability rankings but does not destabilize the model.

Overall, these findings confirm that the model is resilient to small perturbations, though Water plays a critical role in shaping high-suitability areas. This underscores the importance of carefully calibrating weights to ensure stability while preserving meaningful prioritization in site selection.

The Pearson's correlation, Spearman's rank correlation, and Suitability Score 10 Overlap analyses collectively confirm that the model is highly stable under small to moderate weight variations, with minimal impact on suitability values, rankings, and the highest-suitability areas. However, the High-Impact (-20%) Model in both Spearman's and Overlap analyses demonstrated that reducing the weight of Water significantly alters suitability rankings and spatial distribution. While the Inverted Priority Model caused some variation, the model remained structurally robust. These findings highlight the importance of carefully calibrating weights to maintain stability while ensuring meaningful prioritization in site selection.

# 4. RESULTS AND DISCUSSION

The suitability analysis for human habitability in this study (Figure 71) reveals significant differences compared to Zhu et al. (2025) (Figure 13; Section 2.6.2, Human Habitability in Mars). These differences primarily stem from variations in data selection and methodological adjustments. While both studies employ an AHP-based MCDA approach—using an AHP pairwise comparison model adapted from Zhu et al. (2025), which was originally developed for aboveground building scenarios in Mars habitat site selection—Zhu et al. (2025) predominantly identify mid-latitude zones as the most suitable. In contrast, this study highlights a broader range of suitability, including equatorial regions.

A key distinction lies in the treatment of water availability. Zhu et al. (2025) rely on the SWIM dataset (Morgan et al., 2021; Putzig et al., 2023), which maps water ice consistency based on multiple remote sensing indicators. However, SWIM dataset lacks coverage in areas above +1 km elevation, leading to missing data that was treated as low suitability. In contrast, this study utilizes Water Equivalent Hydrogen (WEH) data from Malakhov et al. (2022), derived from neutron spectroscopy. Unlike SWIM, the WEH dataset provides full spatial coverage from 50°N to 50°S, ensuring a more continuous assessment of potential water resources in equatorial regions. Although WEH measures hydrogen abundance rather than directly confirming water ice, it accounts for various hydrogen-bearing forms, including hydrated minerals, adsorbed water, and potentially subsurface ice deposits. Additionally, scientific literature suggests that subsurface ice could exist at equatorial latitudes, challenging the assumption that ice stability is confined to mid-latitudes.

Dust opacity and storm frequency were not included in this study due to data availability constraints. In Zhu et al. (2025), dust was assigned a weight of 0.099 compared to water's weight of 0.416, indicating that water availability has a more substantial influence on long-term habitability assessments. Consequently, the exclusion of dust is not anticipated to significantly affect the overall suitability patterns.

Ultimately, both studies offer valuable insights into human habitability on Mars. Zhu et al. (2025) present a conservative model that prioritizes mid-latitude locations with confirmed ice consistency, whereas this study takes a more expansive approach by incorporating a dataset that captures both bound hydrogen and potential subsurface ice.

The next part of the section presents the final integrated suitability map for Mars, which combines the Human Suitability Multi-Criteria Decision Analysis with engineering constraints

for safe landing and robotic operability. Figure 72 shows that regions failing engineering criteria are assigned the lowest suitability score (1), while non-restricted areas retain their original suitability scores (1 to 10).

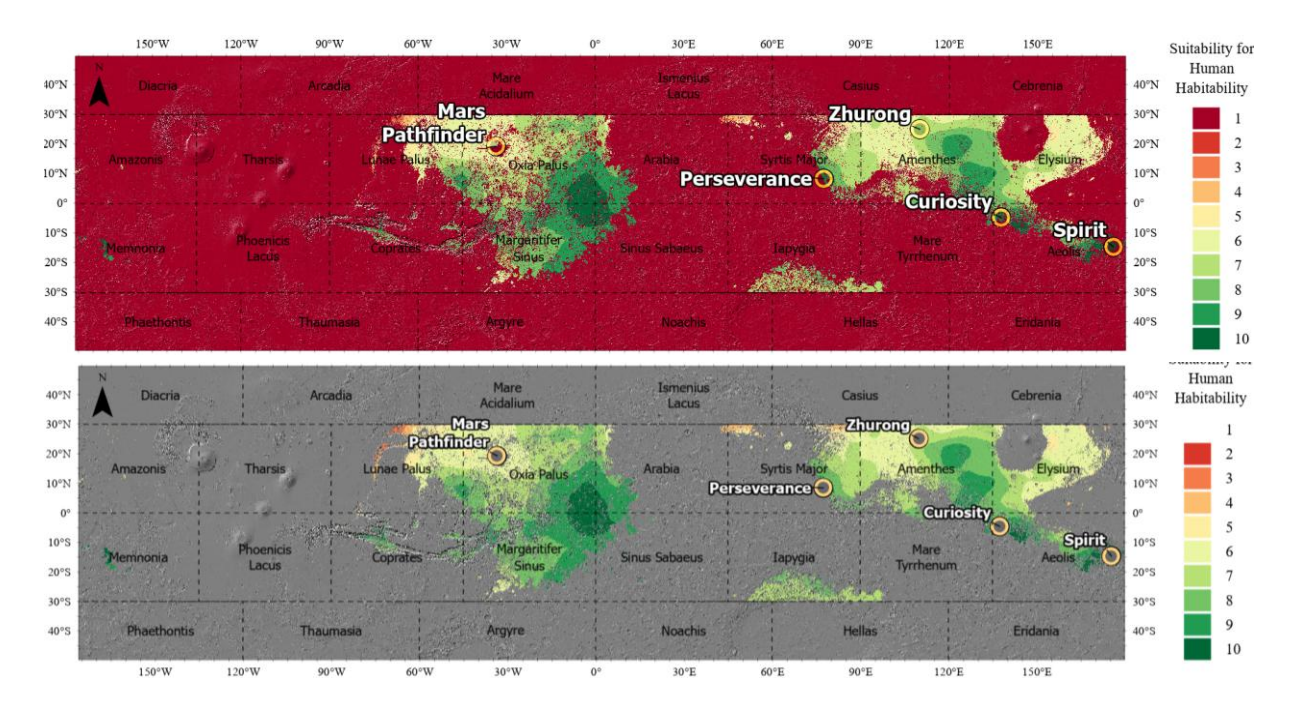


**Figure 72** — Two views of the integrated suitability map for robotic colonies and future human settlement on Mars. Restricted areas receive the lowest score (1), while non-restricted regions retain their scores (2 to 10).

This final integrated suitability map (Figure 72) combines the AHP-based human habitability model (scores 2–10) with engineering constraints for safe landing and robotic operability (where restricted zones are scored as 1).

Notably, the landing sites of Mars rovers—Mars Pathfinder, Perseverance, Curiosity, Spirit, and Zhurong—are all situated within or very close to non-restricted areas. Although these missions relied on criteria that may differ slightly from the latest technological constraints used here (e.g., advances in Entry, Descent, and Landing systems, robotic mobility, and materials), their locations still align well with the map's integrated approach. This outcome suggests that the current criteria capture the essential considerations for landing safety and rover operability, reinforcing the robustness of the methodology. Moreover, by incorporating both habitability and engineering factors, the map provides a comprehensive tool for guiding future site selection for robotic colonies and potential human settlements on Mars.

Furthermore, to offer a clearer perspective on the most favorable regions for robotic colonies and potential human settlements, a focused visualization was generated (Figure 73) by filtering

out lower-scoring areas. This map highlights only those zones with suitability scores of 8, 9, or 10. Two additional map views are displayed from significant suitable regions.

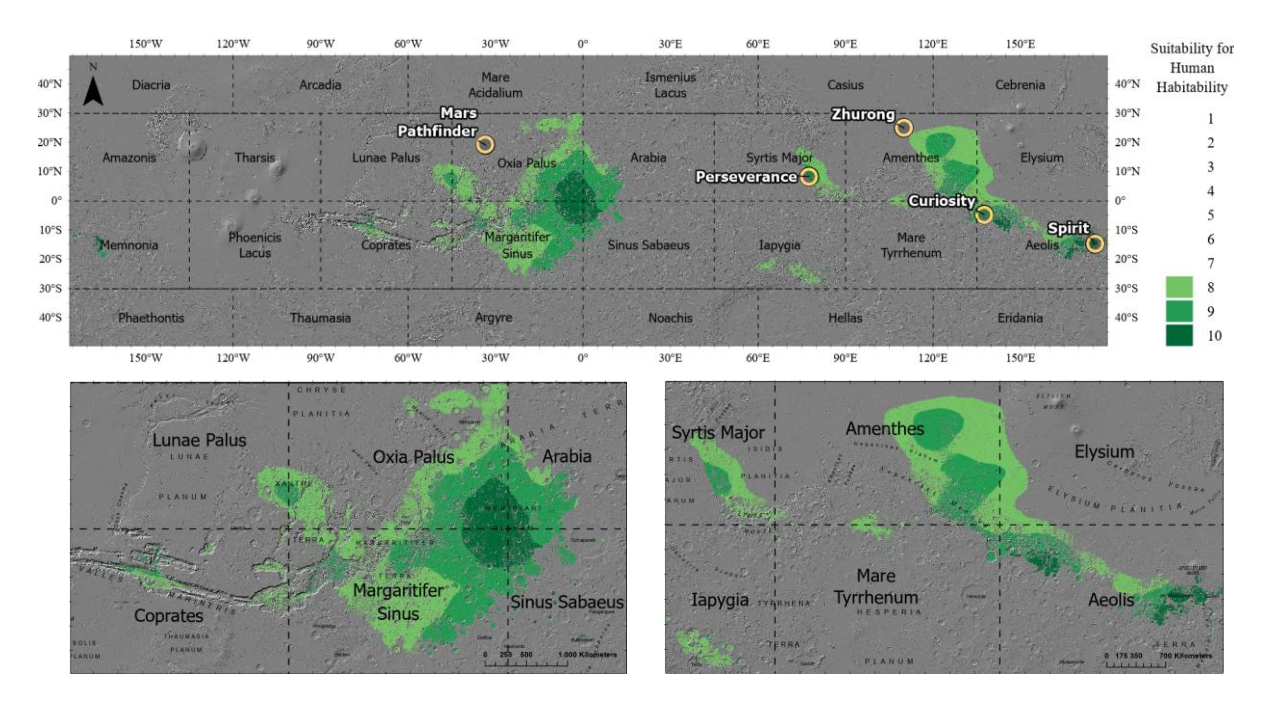


**Figure 73**—Filtered Suitability Map of Mars (50°N to 50°S) displaying the most promising regions for future robotic colonies and potential human settlements (highest-scoring areas 8, 9, and 10), based on integrated habitability criteria and engineering constraints. Mars Rovers displayed in main map for reference.

The filtered suitability map (Figure 73) highlights key regions with high potential for robotic colonies and future human settlement. Notably, Margaritifer Sinus and Oxia Palus exhibit strong suitability, aligning with previous studies indicating extensive past hydrological activity, including valley networks and sedimentary deposits suggestive of sustained liquid water presence (Grant & Parker, 2002; Hynek et al., 2010). These regions are also of particular interest due to their potential for subsurface water ice, which could serve as a vital resource for future missions (Ehlmann et al., 2011).

Similarly, Amenthes emerges as a promising site, consistent with evidence of fluvial erosion and past aqueous processes that may have contributed to near-surface ice stability in the region (Rodriguez et al., 2016). Meanwhile, Elysium stands out due to its association with geologically recent water-related activity, such as outflow channels and potential subsurface ice deposits detected in mid-latitude regions (Dundas et al., 2018). These characteristics make Elysium a compelling candidate for long-term exploration and resource utilization.

Overall, the high-suitability zones identified in this analysis coincide with scientifically significant regions that not only offer potential access to water resources but also provide

relatively stable terrain, reinforcing the robustness of the applied methodology in selecting optimal sites for robotic and eventual human settlement.

To further refine the visualization and analysis, a more focused visualization was generated (Figure 74), highlighting only areas with the highest suitability score of 10. This representation, complemented by four localized views, emphasizes the most promising regions for robotic colonies and potential future human settlements. By isolating the most optimal locations, these visualizations provide deeper insight into their spatial distribution, topographic context, and potential for long-term sustainability.

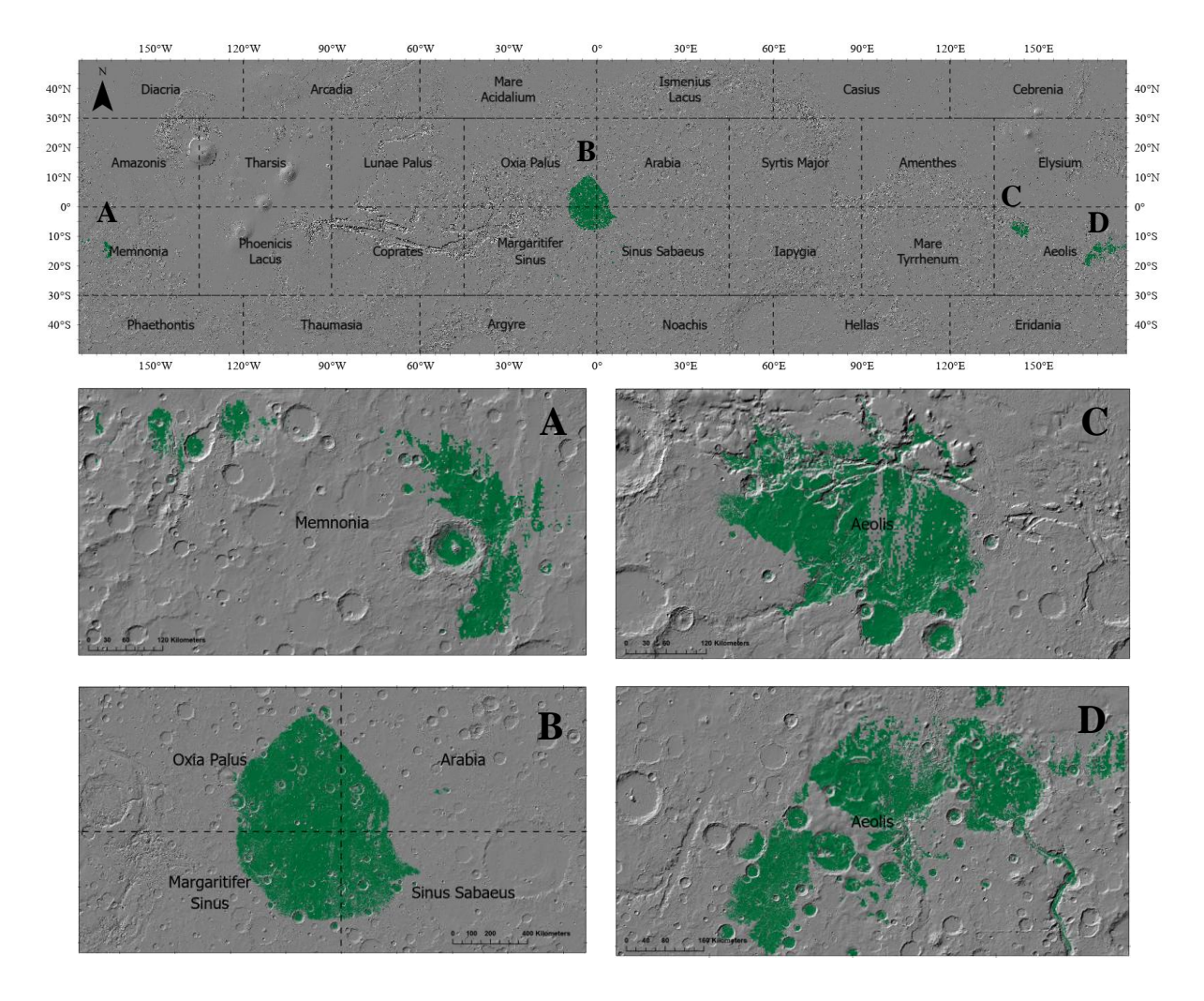


**Figure 74** — Focused Suitability Map for Mars (50°N to 50°S) highlighting only regions with a suitability score of 10. Four supplementary local-scale map views (A-D) further detail these key areas, offering an in-depth perspective on the most favorable zones for robotic colonies and potential human settlements.

Figure 74 presents the most suitable regions for robotic colonies and future human settlement, displaying only areas with a suitability score of 10. This refined visualization isolates the most promising sites, with four key regions examined in local-scale maps. These regions are located

within the Memnonia (A), the four-region intersection, between Oxia Palus–Margaritifer–Arabia–Sinus Sabaeus (B); and the Aeolis quadrangle (C and D), both of which meet the highest criteria for suitability.

A key distinction emerges when comparing these four areas. Region B appears more spatially extensive and contiguous, making it a preferable candidate for site selection. Its broad, uninterrupted distribution of highly suitable terrain provides greater flexibility in choosing an exact landing location. This factor is particularly advantageous when accounting for the uncertainty of a landing ellipse, as a larger continuous area of high suitability increases the probability of a safe and optimal landing.

In contrast, while the Memnonia and Aeolis regions (A, C and D) also meet the highest suitability criteria, their suitable areas are more fragmented. The presence of craters and uneven terrain suggests that a landing ellipse in this area may intersect both highly suitable and less favorable zones, introducing potential challenges for mission planning. Although the suitability score validates its potential, the topographical constraints make it comparatively less favorable than the more uniform and expansive terrain found in the region B.

These findings highlight the importance of spatial continuity and topographical context when selecting sites for robotic and future human missions. While suitability scores provide valuable insights, the physical landscape plays a crucial role in determining the feasibility of landing and long-term settlement on Mars.

### 5. CONCLUSIONS

This study combined the Analytic Hierarchy Process within a Multi-Criteria Decision Analysis framework with engineering constraints to identify optimal regions for robotic colonies as precursors to human settlement on Mars. The critical engineering constraints—slope, elevation, latitude, surface reflectivity and load-bearing surface properties—were derived from the latest successfully landed Mars mission, Perseverance (Mars 2020), to delineate non-viable areas for safe landing and robotic operability. The suitability analysis then evaluated key habitability factors, including surface temperature, water-equivalent hydrogen, elevation and terrain stability, to identify the most suitable locations from non-restricted areas.

The final integrated suitability map highlights as the most promising sites the regions located at the four-quadrangle intersection between Oxia Palus–Margaritifer Sinus–Arabia–Sinus Sabaeus, with and area of ≈600'000 km²; two regions located at Memnonia quadrangle, with

an area of  $\approx 30'000 \text{ km}^2$ ; and two regions located at quadrangle Aeolis, area  $\approx 160'000 \text{ km}^2$ . The region at the four-quadrangle intersection is the region emerging as the preferred option due to its larger, more contiguous terrain, which reduces landing uncertainties and enhances mission flexibility. These optimal regions for robotic colonies, serving as precursors to future human habitation, are shaped by current technological limitations, including Entry, Descent, and Landing (EDL) capabilities, robotic mobility, operability, material resistance, and energy generation. As technology advances, previously restricted areas may become viable, emphasizing the need for adaptable site selection methodologies that can integrate future developments.

Finally, this study demonstrates how integrating human habitability factors with engineering constraints can guide the selection of optimal robotic colony sites. By ensuring both safe and sustainable robotic operations, these findings contribute to the broader objective of establishing a long-term human presence on Mars. Beyond advancing planetary exploration, this research aligns with humanity's ultimate pursuit of interplanetary expansion—securing our survival, extending scientific frontiers and establishing Mars as a gateway for future deep-space exploration.

### 6. FUTURE WORK

Future research should explore the spaciotemporal behavior of the suitable regions for robotic and/or human colonization in Mars. This could be conducted to evaluate how seasonal and orbital variations affect the habitability of potential robotic and human colony sites, particularly in mid-latitude regions where temperature and atmospheric conditions fluctuate the most. Understanding these variations will also be crucial for assessing long-term mission feasibility.

Expanding the scope of potential human settlement sites, future studies should integrate subsurface habitat data, such as caves and volcanic structures, into habitability assessments. These features could be classified based on environmental conditions, terrain stability, safety and overall suitability for human habitation, providing valuable insights into natural shelter options on Mars.

Lastly, incorporating Mars' geological map into site selection studies could enhance the understanding of lithological suitability for both robotic and human colonies. Evaluating terrain composition and its impact on construction feasibility, agriculture, resource extraction, and overall habitability could refine multi-criteria decision models, further optimizing future site selection methodologies.

# **BIBLIOGRAPHICAL REFERENCES**

- Amini, K., Moradi, M., Teymoori, P. E. B., Vossoughi, B., Janabadi, E. D., & Fayaz, R. (2022).

  Design of a set of habitat units and the corresponding surrounding cluster for long-term scientific missions in the pre-terraforming era on mars. Icarus, 385, 115119.
- Boynton, W. V., Feldman, W. C., Squyres, S. W., Prettyman, T. H., Bruckner, J., Evans, L. G., ... & Shinohara, C. (2002). Distribution of hydrogen in the near surface of Mars: Evidence for subsurface ice deposits. *science*, 297(5578), 81-85.
- Byrne, S., Dundas, C. M., Kennedy, M. R., Mellon, M. T., McEwen, A. S., Cull, S. C., ... & Seelos, F. P. (2009). Distribution of mid-latitude ground ice on Mars from new impact craters. *Science*, *325*(5948), 1674-1676.
- Campa, R., Szocik, K., & Braddock, M. (2019). Why space colonization will be fully automated. *Technological Forecasting and Social Change*, 143, 162–171. https://doi.org/10.1016/j.techfore.2019.03.021
- Carr, M. H., & Head, J. W. (2015). Martian surface/near-surface water inventory: Sources, sinks, and changes with time. *Geophysical Research Letters*, 42(3), 726-732.
- Chen, G., Han, Y., Li, Y. et al. Autonomous gait switching method and experiments of a hexapod walking robot for Mars environment with multiple terrains. Intel Serv Robotics 17, 533–553 (2024). https://doi.org/10.1007/s11370-023-00508-z
- Dundas, C. M., Bramson, A. M., Ojha, L., Wray, J. J., Mellon, M. T., Byrne, S., ... & Holt, J. W. (2018). Exposed subsurface ice sheets in the Martian mid-latitudes. Science, 359(6372), 199-201.
- Ehlmann, B. L., Mustard, J. F., Murchie, S. L., Bibring, J. P., Meunier, A., Fraeman, A. A., & Langevin, Y. (2011). Subsurface water and clay mineral formation during the early history of Mars. *Nature*, 479(7371), 53-60.

- Fergason, R. L., Hare, T. M., & Laura, J. (2018). HRSC and MOLA blended digital elevation model at 200m v2. *Astrogeology PDS Annex, US Geological Survey*, 5.
- Forget, F., Hourdin, F., Fournier, R., Hourdin, C., Talagrand, O., Collins, M., ... & Huot, J. P. (1999). Improved general circulation models of the Martian atmosphere from the surface to above 80 km. *Journal of Geophysical Research: Planets*, 104(E10), 24155-24175.
- Georgiou, C. D., Zisimopoulos, D., Kalaitzopoulou, E., & Quinn, R. C. (2017). Radiation-driven formation of reactive oxygen species in oxychlorine-containing Mars surface analogues. *Astrobiology*, 17(4), 319-336.
- Golombek, M. P., Cook, R. A., Moore, H. J., & Parker, T. J. (1997). Selection of the Mars Pathfinder landing site. *Journal of Geophysical Research: Planets*, 102(E2), 3967-3988.
- Golombek, M., Grant, J., Kipp, D. *et al.* Selection of the Mars Science Laboratory Landing Site. *Space Sci Rev* **170**, 641–737 (2012). https://doi.org/10.1007/s11214-012-9916-y
- Golombek, M. P., Grant, J. A., Parker, T. J., Kass, D. M., Crisp, J. A., Squyres, S. W., Haldemann, A. F. C., Adler, M., Lee, W. J., Bridges, N. T., Arvidson, R. E., Carr, M. H., Kirk, R. L., Knocke, P. C., Roncoli, R. B., Weitz, C. M., Schofield, J. T., Zurek, R. W., Christensen, P. R., ... Rice, J. W., Jr. (2003). Selection of the Mars Exploration Rover landing sites. *Journal of Geophysical Research: Planets*, 108(12), Article 12.
  Scopus. https://doi.org/10.1029/2003je002074
- González-Galindo, F., Chaufray, J. Y., López-Valverde, M. A., Gilli, G., Forget, F., Leblanc,
   F., ... & Yagi, M. (2013). Three-dimensional Martian ionosphere model: I. The photochemical ionosphere below 180 km. *Journal of Geophysical Research:* Planets, 118(10), 2105-2123.

- Grant, J. A., Golombek, M. P., Wilson, S. A., Farley, K. A., Williford, K. H., & Chen, A. (2018). The science process for selecting the landing site for the 2020 Mars rover. *Planetary and Space Science*, 164, 106–126. https://doi.org/10.1016/j.pss.2018.07.001
- Grant, J. A., & Parker, T. J. (2002). Drainage evolution in the Margaritifer Sinus region, Mars. *Journal of Geophysical Research: Planets*, 107(E9), 4-1.
- Hecht, M. H., Kounaves, S. P., Quinn, R. C., West, S. J., Young, S. M., Ming, D. W., ... & Smith, P. H. (2009). Detection of perchlorate and the soluble chemistry of martian soil at the Phoenix lander site. *Science*, *325*(5936), 64-67.
- Heldmann, J. L., Marinova, M. M., Lim, D. S., Wilson, D., Carrato, P., Kennedy, K., ... & Coyan, J. (2022). Mission architecture using the SpaceX starship vehicle to enable a sustained human presence on Mars. *New Space*, *10*(3), 259-273.
- Huang, Y., Wu, S., Mu, Z., Long, X., Chu, S., & Zhao, G. (2020). A Multi-agent Reinforcement Learning Method for Swarm Robots in Space Collaborative Exploration. 2020 6th International Conference on Control, Automation and Robotics (ICCAR), 139–144. https://doi.org/10.1109/ICCAR49639.2020.9107997
- Huntsberger, T., Rodriguez, G., & Schenker, P. S. (2000, March). Robotics challenges for robotic and human mars exploration. In *Robotics 2000* (pp. 340-346).
- Hynek, B. M., Beach, M., & Hoke, M. R. (2010). Updated global map of Martian valley networks and implications for climate and hydrologic processes. *Journal of Geophysical Research: Planets*, 115(E9).
- Jet Propulsion Laboratory. (2020). *Missions*. NASA. Retrieved January 30, 2025, from https://www.jpl.nasa.gov/missions/
- Lele, A. S., Fang, Y., Ting, J., & Raychowdhury, A. (2020, August). Learning to walk: Spike based reinforcement learning for hexapod robot central pattern generation. In 2020 2nd

- IEEE International Conference on Artificial Intelligence Circuits and Systems (AICAS) (pp. 208-212). IEEE.
- Leslie, J. (2002). The End of the World: the science and ethics of human extinction. Routledge.
- Maity, T., & Saxena, A. (2024). Challenges and innovations in food and water availability for a sustainable Mars colonization. *Life Sciences in Space Research*, 42, 27–36. https://doi.org/10.1016/j.lssr.2024.03.008
- Malakhov, A. V., Mitrofanov, I. G., Golovin, D. V., Litvak, M. L., Sanin, A. B., Djachkova, M. V., & Lukyanov, N. V. (2022). High Resolution Map of Water in the Martian Regolith Observed by FREND Neutron Telescope Onboard ExoMars TGO. *Journal of Geophysical Research: Planets*, 127(5), Article 5. https://doi.org/10.1029/2022JE007258
- Martinez Rocamora, B., Jr., Kilic, C., Tatsch, C., Pereira, G. A. S., & Gross, J. N. (2023). Multirobot cooperation for lunar In-Situ resource utilization. *Frontiers in Robotics and AI*, 10. Scopus. https://doi.org/10.3389/frobt.2023.1149080
- Mellerowicz, B., Zacny, K., Palmowski, J., Bradley, B., Stolov, L., Vogel, B., ... & Hecht, M. (2022). RedWater: Water Mining System for Mars. *New Space*, *10*(2), 166-186.
- Mellon, M.T., Jakosky, B.M., Kieffer, H.H., Christensen, P.R., 2000. Highresolution thermal inertia mapping from the Mars Global Surveyor Thermal Emission Spectrometer. Icarus 148, 437–455.
- Millour, E., Forget, F., Spiga, A., Pierron, T., Bierjon, A., Montabone, L., ... & Cipriani, F. (2024). The Mars Climate Database, MCD version 6. In *Europlanet Science Congress* 2024 (Vol. 17, pp. EPSC2024-516).
- Millour, E., Forget, F., Spiga, A., Pierron, T., Bierjon, A., Montabone, L., ... & Cipriani, F. (2022). The mars climate database (version 6.1). In *Europlanet Science Congress* 2022 (Vol. 16, pp. EPSC2022-786).

- Millour, E., Forget, F., & Lewis, S. R. (2014). Mars climate database v. 5.1. User manual. *ESTEC Contract*, 11369, 95.
- NASA Hubble Mission Team. (2008). NASA's Hubble Space Telescope close-up of the red planet Mars. NASA Science. Retrieved January 30, 2025, from https://science.nasa.gov/missions/hubble/nasas-hubble-space-telescope-close-up-of-the-red-planet-mars/
- NASA. (2024). *Mars exploration: Science goals*. Retrieved January 30, 2025, from https://science.nasa.gov/planetary-science/programs/mars-exploration/science-goals/
- Ord, T. (2020). The precipice: Existential risk and the future of humanity. Hachette Books.
- Orosei, R., Lauro, S. E., Pettinelli, E., Cicchetti, A. N. D. R. E. A., Coradini, M., Cosciotti, B., ... & Seu, R. (2018). Radar evidence of subglacial liquid water on Mars. *Science*, *361*(6401), 490-493.
- Pajola, M., Rossato, S., Baratti, E., & Kling, A. (2019a). Planetary mapping for landing sites selection: The mars case study. *Lecture Notes in Geoinformation and Cartography*, 175–190. Scopus. https://doi.org/10.1007/978-3-319-62849-3 7
- Petrovsky, A., Kalinov, I., Karpyshev, P., Tsetserukou, D., Ivanov, A., & Golkar, A. (2022).

  The two-wheeled robotic swarm concept for Mars exploration. *Acta Astronautica*, 194,

  1–8. https://doi.org/10.1016/j.actaastro.2022.01.025
- Piqueux, et al., Widespread shallow water ice on mars at high latitudes and midlatitudes, Geophys. Res. Lett. 46 (2019) 14290e14298, https://doi.org/10.1029/2019GL083947.
- Putzig, N., Mellon, M., Kretke, K., & Arvidson, R. (2005). Global thermal inertia and surface properties of Mars from the MGS mapping mission. *Icarus*, *173*(2), 325–341. https://doi.org/10.1016/j.icarus.2004.08.017

- Puumala, M. M., Sivula, O., & Lehto, K. (2023). Moving to Mars: The Feasibility and Desirability of Mars Settlements. *Space Policy*, 66, 101590. https://doi.org/10.1016/j.spacepol.2023.101590
- Rapp, D. (2023). 60+ Years of Humans to Mars Mission Planning. In *Human Missions to Mars:*Enabling Technologies for Exploring the Red Planet (pp. 27-127). Cham: Springer International Publishing.
- Rees, M. J. (2003). Our final hour: A scientist's warning: how terror, error, and environmental disaster threaten humankind's future in this century--on earth and beyond. Basic Books (AZ).
- Rodriguez, J. A. P., Kargel, J. S., Baker, V. R., Gulick, V. C., Berman, D. C., Fairén, A. G., ... & Glines, N. (2015). Martian outflow channels: How did their source aquifers form and why did they drain so rapidly?. *Scientific Reports*, *5*(1), 13404.
- Romioa, A. F. A. P. (2022). Mars Underground: a Landscape Strategy for Long Term Human Colonies on the Red Planet. In *IAC 2022 Congress Proceedings, 73rd International Astronautical Congress (IAC), Paris, France* (pp. 1-15). International Astronautical Federation.
- Röstel, L., Guo, J., Banjac, S., Wimmer-Schweingruber, R. F., & Heber, B. (2020). Subsurface radiation environment of Mars and its implication for shielding protection of future habitats. *Journal of Geophysical Research: Planets*, *125*(3), e2019JE006246.
- Saaty, T. L. (1990). How to make a decision: the analytic hierarchy process. European journal of operational research, 48(1), 9-26.
- Schulze-Makuch, D., Irwin, L.N. (2008). Optimizing Space Exploration. In Schulze-Makuch, D., Irwin, L.N. (Eds). Life in the Universe. Advances in Astrobiology and Biogeophysics. Springer. https://doi.org/10.1007/978-3-540-76817-3\_13

- Starr, S. O., & Muscatello, A. C. (2020). Mars in situ resource utilization: a review. *Planetary and Space Science*, 182, 104824.
- Verseux, C., Baqué, M., Lehto, K., de Vera, J. P. P., Rothschild, L. J., & Billi, D. (2016).

  Sustainable life support on Mars—the potential roles of cyanobacteria. *International Journal of Astrobiology*, 15(1), 65-92.
- Vincendon, M., Mustard, J., Forget, F., Kreslavsky, M., Spiga, A., Murchie, S., & Bibring, J. P. (2010). Near-tropical subsurface ice on Mars. *Geophysical Research Letters*, *37*(1).
- Vithanage, M., Kumarathilaka, P., Oze, C., Karunatilake, S., Seneviratne, M., Hseu, Z. Y., ...
  & Rinklebe, J. (2019). Occurrence and cycling of trace elements in ultramafic soils and their impacts on human health: A critical review. *Environment International*, 131, 104974.
- Watters, T. R., Campbell, B. A., Leuschen, C. J., Morgan, G. A., Cicchetti, A., Orosei, R., & Plaut, J. J. (2024). Evidence of Ice-Rich Layered Deposits in the Medusae Fossae Formation of Mars. *Geophysical Research Letters*, 51(2), e2023GL105490. https://doi.org/10.1029/2023GL105490
- Zhang, J., Liu, Q., Zhou, J., & Song, A. (2022). Crab-inspired compliant leg design method for adaptive locomotion of a multi-legged robot. *Bioinspiration & Biomimetics*, 17(2), 025001.
- Zhu, S., Zhao, B., Yan, Y., & Shi, X. (2025). Habitat site selection on Mars: Suitability analysis and mapping. *Acta Astronautica*, 226, 1–22. https://doi.org/10.1016/j.actaastro.2024.11.019



# Masters Program in Geospatial Technologies



